Proton Therapy Planning using the S_N Method with the Fokker-Planck Approximation

Master's Thesis

Author:
Sander Bastiaan Uilkema
Studentnumber: 1232428
Thesis Registration Number: PNR-131-2012-013

Supervisor:
dr. ir. Danny Lathouwers

Committee Members:
dr. ir. D. Lathouwers
dr. ir. J.L. Kloosterman
dr. ir. D.R. Schaart
dr. N.V. Budko

Section Physics of Nuclear Reactors
Department of Radiation, Radionuclides and Reactors
Faculty of Applied Sciences
Delft University of Technology

October, 2012

TU Delft Delft University of Technology

Abstract

Proton therapy is a type of therapy where the disease area, most often a cancerous tumor, is irradiated by an external beam of protons. Tissue surrounding the tumor is exposed in this process as well. The resulting dose in normal tissue can lead to undesirable long term side effects. To minimize the dose in normal tissue, there is a need for accurate treatment planning methods. These methods are used in the planning stage to calculate the optimal treatment plan. Planning methods now consist out of fast approximations such as pencil beam algorithms and uniform-intensity algorithms, and a very accurate but very slow approach: the Monte Carlo method. In this thesis, an alternative method is investigated: the S_N method.

The S_N method is a deterministic method in which the solution of the transport equation is approximated by discretization of all its independent variables. In principle, this method can be as accurate as the Monte Carlo method, and has some additional advantages: it can be considerably faster, it offers a dose distribution over the entire region of simulation, and it is suitable for perturbation techniques (which allows us to capture to effects of the uncertainty in the chemical composition of the tissue in the patient, and the movement of the patient).

The S_N method was first developed by reactor physicists who used it to calculate the neutron distribution in a reactor core. In this thesis, the method is used to calculate the proton distribution in a patient. The nature of interaction of the proton, however, is different from that of the neutron: due to the Coulomb interactions, the proton has a large number of small angle scatter interactions. This type of interaction is expressed in nearly singular differential scatter cross sections. It is very unpractical to treat these differential cross sections with conventional means in deterministic methods. To deal with this issue, the Fokker-Planck approximation is used. In this approximation, the small angle scatters and the small energy transfers are described by the Fokker-Planck operators.

In this thesis it is investigated whether the S_N method is accurate enough to replace the Monte Carlo method in proton therapy planning, and what underlying methods need to be improved to reach its potential computational speed. For this purpose, the available models and methods for charged particles transport are investigated on accuracy and applicability for protons in the energy range considered in proton therapy.

To investigate the accuracy of the S_N method, two Monte Carlo calculations are used as a benchmark. The results are very promising: the dose profiles of the two methods are almost exactly overlapping. The angular part of the solution, however, cannot be benchmarked with our 1D S_N calculations, 3D calculations should validate this part of the problem in future work.

The underlying methods we used in our work need at least three improvements to reach the potential computation speed of the S_N method: (i) a more advanced discretization method in the spatial and angular domain is necessary, for example, a linear discontinuous finite element method, (ii) adaptive mesh refinement in the spatial and angular range is needed to obtain the most optimal discretization structure, and (iii) acceleration of the convergence of the continuous scatter operator is necessary with, for example, a multi-grid method.

Acknowledgements

I would like to express my gratitude towards my supervisor Danny Lathouwers for giving me the opportunity for doing this MSc project and for the guidance he gave me during the thesis. The weekly meetings with him were of great value. During the thesis, he showed great patience in guiding me through the numerous of issues encountered, for which I am very thankful. Without his help, this project would not have been possible.

I would also like to thank my parents for their support and encouragement during my MSc program and especially for their help during this thesis.

List of Symbols

Latin Symbols

Symbol	Description	Units
A_t	Mass count of target particle	[-]
b	Impact parameter	[cm]
c	Speed of light	[cm/s]
D	Deposited dose	[J/kg]
$\frac{df_n}{dE_n}$	Generalized oscillator strength	[-]
e	Elementary charge	[C]
E	Energy	[MeV]
E_{dep}	Deposited energy	[MeV]
E_g	Energy at center of energy group g	[MeV]
$E_{g-\frac{1}{2}}$	Energy on upper boundary of energy group g	[MeV]
$E_{g+\frac{1}{2}}$	Energy on lower boundary of energy group g	[MeV]
ΔE_g	Width of energy group g	[MeV]
E_{in}	Energy of mono-energetic boundary condition	[MeV]
E_k	Kinetic energy of incident proton	[MeV]
E_{max}	Maximum energy of energy plateau boundary condition	[MeV]
ΔE_p	Width of energy plateau boundary condition	[MeV]
E_s	Energy of secondary particle	[MeV]
f	Factor used in relationships $w_n^a = f \cdot w_{n+1}^a$ and $\Delta E_g = f \cdot \Delta E_{g+1}$	[-]
f_{iso}	Arbitrary isotropic function	[-]
g	Energy group index	[-]
H	Maximum energy transfer in a single collsion for which the collision can be considered soft	[MeV]
i	Spatial element index	[-]
I_{in}	Incident intensity	[# s^{-1} cm^{-2}]
I	Geometric mean of all ionization and excitation potentials of target atom	[eV]
L	Order of Legendre expansion	[-]
L_a	Arbitrary operator which does not depend on variable which is being discretized	[-]
L_B	Boltzmann scatter operator	[-]
$L_{B,e}$	Boltzmann scatter operator of elastic scatter process	[-]
$L_{B,in}$	Boltzmann scatter operator of inelastic scatter process	[-]
L_{CS}	Continuous scatter operator	[-]
L_{CSD}	Continuous slowing down operator	[-]
L_{ES}	Energy straggling operator	[-]
L_{str}	Streaming operator	[-]
m_0	Reduced mass of incident particle	[kg]
m_e	Mass of electron	[kg]

Symbol	Description	Units
m_i	Mass of incident particle	[kg]
m_p	Mass of proton	[kg]
m_t	Mass of target particle	[kg]
n	Discrete ordinate index	[-]
N	Total number of discrete ordinates in quadrature set	[-]
NE	Total number of spatial elements	[-]
NG	Total number of energy groups	[-]
p	Momentum of incident proton	[kg cm s^{-1}]
p^A	Basis function: 1	[-]
p^E	Basis function: $\frac{2}{\Delta E_g}(E - E_g)$	[-]
P_l	Legendre polynomial of order l	[-]
$\vec{r}$	Position vector (x, y, z)	[cm]
$r^l_{i,n,g}$	Residual after iteration l of spatial cell i, ordinate n and energy group g	[-]
ref	Subscript indicating the value used in reference calculation	[-]
S	Stopping power	[MeV cm^{-1}]
$S_{g\pm\frac{1}{2}}$	Stopping power evaluated at boundaries of energy group g	[MeV cm^{-1}]
S_{soft}	Stopping power due to soft collision Coulomb interactions	[MeV cm^{-1}]
S_{hard}	Stopping power due to hard collision Coulomb interactions	[MeV cm^{-1}]
T	Energy straggling coefficient	[MeV^2 cm^{-1}]
Q	Energy lost in a single collision by incident proton	[MeV]
Q_{max}	Maximum energy lost by incident proton in a single collision	[MeV]
Q_{min}	Minimum energy lost by incident proton in a single collision	[MeV]
v_0	Velocity of incident proton	[cm s^{-1}]
v_e	Velocity of electron after hard collision Coulomb interaction	[cm s^{-1}]
w_n	Weight of discrete ordinate n, sum of the weights equals 4π	[-]
w^a_n	Weight of discrete ordinate n, sum of the weights equals 2	[-]
x, y, z	Spatial components	[cm]
Y^m_l	Spherical harmonic function of degree l and order m	[-]
Z_i	Charge count of incident particle	[-]
Z_t	Charge count of target particle	[-]

Greek Symbols

Symbol	Description	Units
α	Fine structure constant	[-]
β_n	$1 - \mu_n^2$ (normal scheme), $\beta_{n+\frac{1}{2}} = \beta_{n-\frac{1}{2}} - 2\mu_n w^a_n$ where $\beta_{\frac{1}{2}} = 0$ (advanced scheme)	[-]
ϵ_0	Vacuum permittivity	[F cm^{-1}]
η	Θ^2_{min}	[-]
μ	Cosine of polar angle	[-]
μ_0	Cosine of scattering angle	[-]
μ^*	Boundary between smooth and singular part of elastic differential scatter cross section	[-]
$\hat{\Omega}$	Direction of motion	[-]
$\hat{\Omega}_n$	Discrete ordinate n	[-]
ϕ	Azimuthal angle	[-]
$\phi_{i,g,l}$	Flux moment l of spatial cell i and energy group g	[-]

Symbol	Description	Units
ϕ_{lm}	Flux moment of degree l and order m	[-]
σ_C	Catastrophic scatter cross section	[cm^{-1}]
$\sigma_{C,g}$	Multi-group total catastrophic scatter cross section of energy group g	[cm^{-1}]
$\sigma_{C,g\to g'}$	Multi-group catastrophic scatter cross section from energy group g to g'	[cm^{-1}]
$\sigma_{C,g\to g',l}$	Multi-group catastrophic scatter cross section moment l from energy group g to g'	[cm^{-1}]
$\sigma_{C,s}$	Total catastrophic scatter cross section	[cm^{-1}]
σ_e	Elastic differential scatter cross section	[cm^{-1}]
$\sigma_{e,n}$	n-th moment of elastic scatter cross section	[cm^{-1}]
$\sigma_{e,s}$	Total elastic scatter cross section	[cm^{-1}]
$\sigma_{e,si}$	Singular part of elastic differential scatter cross section	[cm^{-1}]
$\sigma_{e,si,n}$	n-th moment of singular part of elastic scatter cross section	[cm^{-1}]
$\sigma_{e,sm}$	Smooth part of elastic differential scatter cross section	[cm^{-1}]
$\sigma_{e,sm,s}$	Total cross section of smooth part of elastic differential scatter cross section	[cm^{-1}]
σ_{in}	Inelastic differential scatter cross section	[MeV^{-1} cm^{-1}]
$\sigma_{in,s}$	Total inelastic scatter cross section	[cm^{-1}]
$\sigma_{in,m}$	m-th moment of inelastic scatter cross section	[MeV^m cm^{-1}]
$\sigma_{in,soft}$	Soft collision inelastic differential scatter cross section	[MeV^{-1} cm^{-1}]
$\sigma_{in,hard}$	Hard collision inelastic differential scatter cross section	[MeV^{-1} cm^{-1}]
σ_t	Total scatter cross section ($= \sigma_{C,s} + \sigma_{e,s} + \sigma_{in,s}$)	[cm^{-1}]
σ_{tr}	Transport cross section	[cm^{-1}]
$\sigma_{tr,g}$	Multi-group transport cross section of energy group g	[cm^{-1}]
θ	Polar angle	[-]
Θ	Scatter angle	[-]
Θ_{min}	Minimum scatter angle	[-]
$\varphi(\vec{r}, E, \hat{\Omega})$	Angular flux at position $\vec{r}$, with energy E moving in direction $\hat{\Omega}$	[# cm^{-2} MeV^{-1} s^{-1}]
$\varphi(\vec{r}, \hat{\Omega})$	Angular depending differential flux at position $\vec{r}$	[# cm^{-2} s^{-1}]
$\varphi(\vec{r}, E)$	Energy depending differential flux at position $\vec{r}$	[# cm^{-2} MeV^{-1} s^{-1}]
$\varphi(\vec{r})$	Scalar flux at position $\vec{r}$	[# cm^{-2} s^{-1}]
φ_n	Flux in discrete ordinate n	[# cm^{-2} s^{-1}]
$\varphi_{i,n}$	Flux in spatial cell i and discrete ordinate n	[# cm^{-2} s^{-1}]
$\varphi_{a,i,n,g}$	Average flux in spatial cell i, discrete ordinate n and energy group g	[# cm^{-2} MeV^{-1} s^{-1}]
$\varphi_{e,i,n,g}$	Normalized slope of flux in spatial cell i, ordinate n and energy group g	[-]
φ_g^+	Flux value at upper boundary of energy group g: $\varphi(E_{g+\frac{1}{2}})$	[# cm^{-2} MeV^{-1} s^{-1}]
φ_g^-	Flux value at lower boundary of energy group g: $\varphi(E_{g-\frac{1}{2}})$	[# cm^{-2} MeV^{-1} s^{-1}]
ϑ	Cosine scattering angle measured in center-of-mass frame	[-]

Contents

1 Introduction **2**
- 1.1 Radiotherapy in Treating Cancer Patients . . . 2
  - 1.1.1 Biological Effects of Radiation . . . 2
  - 1.1.2 Types of Radiation Therapies . . . 2
- 1.2 Proton Therapy . . . 3
  - 1.2.1 History of Proton Therapy . . . 3
  - 1.2.2 Proton Beam Dose Deposition Properties . . . 3
  - 1.2.3 Proton Therapy Compared to IMRT . . . 4
- 1.3 Treatment Planning . . . 5
  - 1.3.1 Conventional Methods of Treatment Planning . . . 5
  - 1.3.2 The S_N Method . . . 6
- 1.4 Goals of this Thesis . . . 6

2 Proton Interactions with Matter **8**
- 2.1 Elastic Interactions with the Nucleus . . . 8
  - 2.1.1 Transformation of Reference Frame . . . 10
- 2.2 Inelastic Interactions with Atomic Electrons . . . 12
  - 2.2.1 Hard Collisions . . . 13
  - 2.2.2 Soft Collisions . . . 14
- 2.3 Inelastic Interactions with the Nucleus . . . 15
  - 2.3.1 The SADCO Code . . . 15
- 2.4 Conclusions . . . 18

3 Mathematical Description of Proton Transport **19**
- 3.1 The Linear Boltzmann Transport Equation . . . 19
  - 3.1.1 Justification of the Underlying Assumptions . . . 19
  - 3.1.2 Physical Interpretation of the Operators . . . 20
  - 3.1.3 Separation of the Scatter Interactions . . . 20
  - 3.1.4 Introduction of Flux Definitions . . . 21
- 3.2 The Fokker-Planck Approximation . . . 21
  - 3.2.1 Continuous Scatter Operator . . . 23
  - 3.2.2 Continuous Slowing Down and Energy Straggling Operators . . . 25
  - 3.2.3 Validation of the Coefficients . . . 29
- 3.3 Validation of the Fokker-Planck Approximation . . . 30
  - 3.3.1 The Boltzmann-Fokker-Planck Approximation . . . 31
- 3.4 Conclusions . . . 32

4 The S_N Method **34**
- 4.1 The Quadrature Set . . . 34
- 4.2 Angular Discretization . . . 35
  - 4.2.1 Advanced Scheme . . . 36
- 4.3 Spatial Discretization . . . 37
- 4.4 Energy Discretization . . . 38

4.4.1 The Boltzmann Scatter Operator . . . 40
4.4.2 Continuous Slowing Down Operator . . . 41
4.4.3 Energy Straggling Operator . . . 42
4.5 Conclusions . . . 43

5 Numerical Solution of the Discretized System 44
5.1 The Iterative Method . . . 44
5.2 Energy Deposition . . . 46
5.2.1 Identification of Streaming, Deposition and Source Terms . . . 47
5.2.2 Dose . . . 49
5.3 Conclusions . . . 49

6 Investigation of Discretization Requirements 50
6.1 General Computational Set-up . . . 51
6.1.1 Geometry and Material . . . 51
6.1.2 Boundary Condition . . . 51
6.1.3 Structure of the Discretization . . . 52
6.2 Spatial Discretization . . . 53
6.2.1 Test Case A . . . 53
6.2.2 Test Case B . . . 53
6.3 Energy Discretization . . . 55
6.3.1 Test Case A . . . 55
6.3.2 Test Case C . . . 58
6.4 Angular Discretization . . . 58
6.4.1 Test Case B . . . 58
6.4.2 Test Case C . . . 59
6.5 Conclusions . . . 59

7 Results 61
7.1 Benchmark Cases . . . 61
7.1.1 Computational Set-up . . . 61
7.1.2 Results . . . 62
7.2 Medulloblastoma Case . . . 64
7.2.1 Computational Set-up . . . 64
7.2.2 Results . . . 65
7.3 Conclusions . . . 67

8 Discussion and Conclusions 68
8.1 Models for Describing Protons Transport . . . 68
8.2 Methods to Solve the Transport Equation . . . 69
8.3 Main Question of the Thesis . . . 70
8.4 Conclusion . . . 71
8.5 Future Work . . . 71

A Rutherford Scatter 74

B Derivation of Continuous Slowing Down and Energy Straggling Operators 78

C Effect of Energy Straggling Operator on Solution of Transport Equation 79

D Results Discretization Requirements 81

List of Figures

1.1 Left: a T1 weighted MRI scan[34] of a 4-year-old medulloblastoma patient. Right: the spread-out Bragg peak (SOBP). Since the size of the tumor is usually large compared to the width of a single Bragg peak, a particle beam with multiple energies is used to obtain energy deposition over the entire range of the tumor. 4

1.2 Left: dose distribution of photons compared to the dose distribution of protons[6]. Right: proton therapy treatment plan compared to a photon therapy treatment plan[35]. The critical organs in the human head are much more spared using proton therapy. 5

2.1 The trajectory of an incident proton with impact parameter b, interacting with a particle through the Coulomb force. The proton is scattered in angle Θ. 9

2.2 Relation between the cosine scattering angle $\cos(\Theta)$ of the incident proton measured in the center-of-mass frame, and in the laboratory frame $\cos(\vartheta)$ for different target nuclei. 11

2.3 Correction factor for transformation of differential cross section expressed in coordinates in the center-of-mass frame to the differential cross section expressed in coordinates in the laboratory frame for protons incident of a nucleus, see equation 2.14. 12

2.4 Screened Rutherford cross section for incident protons on water for various energies. The cross sections are nearly singular at $\mu_0 = 1$. 13

2.5 Screened Rutherford cross section for hard collisions between incident protons and electrons for various energies. The cross sections are nearly singular at $Q = 0$. 14

2.6 Multi-group coupled differential cross sections expanded in a P_{11} Legendre series, evaluated with the SADCO code. Left: proton to neutron cross sections from energy group g to g'. Right: proton to proton cross sections from energy group g to g'. 16

2.7 Multi-group coupled differential cross sections expanded in a P_{11} Legendre series, evaluated with the SADCO code. Left: proton to proton cross sections on hydrogen from energy group g to g'. Right: multi-group total cross sections for protons incident on water. 17

3.1 The nearly singular differential cross sections of charged particles expanded in Legendre functions. 22

3.2 Momentum transfer cross section $\sigma_{tr}(E)$ for protons incident on water. . . . 26

3.3 Stopping power $S(E)$ of protons incident on water. 27

3.4 The energy straggling coefficient $T(E)$ for protons incident on water. 28

3.5 Stopping power evaluated with equation 3.28 compared to literature values of PSTAR[2]. 29

3.6 Left: moments of the inelastic Rutherford cross section for protons incident on water. Right: moments for the elastic Rutherford cross section for protons incident on water. 30

3.7 Left: the 1D pencil beam problem can be visualized in the 3D geometry as the uniform radiation of an infinite large slab. Large angle scatter can be ignored in this case. Right: 3D pencil beam problem. Large angle scatter can not be ignored in this case, since in this process energy is pushed to the surrounding tissue, where critical organs may be present. 31

3.8 Left: decomposition of the differential cross section into a smooth and a singular part. Right: moments of the singular part of the elastic cross section for protons incident on water for different energies. $\mu^* = 0.98$ was set here, but different choices for μ^* near $\mu^* = 0.98$ gave similar results. . . 32

4.1 A pencil beam on a slab. The direction of movement of the protons are characterized by the directional cosine $\mu_n = \cos(\theta_n)$. The directional cosine of the particles in the pencil beam is $\mu = 1$. 35

4.2 Representation of the variables which characterize the quadrature set. μ_n is the directional cosine, w_n^a the weight and φ_n the flux value of the discrete ordinate $\hat{\Omega}_n$. 36

4.3 Upper: representation of the step scheme. The 1D slab is divided into NE cells, the flux inside these cells is assumed to be constant, and allowed to be discontinuous an the cell faces. Bottom: representation of the upwind scheme in the spatial domain. If $\mu_n > 0$, the direction of the particle flow (from left to right) is simulated by assuming $\varphi_{i-\frac{1}{2}} = \varphi_{i-1}$ and $\varphi_{i+\frac{1}{2}} = \varphi_i$. Vice versa for $\mu_n < 0$. 38

4.4 Representation of the multi-group method. NG is the total number of energy groups used to divide the energy range. E_g is the center energy value of enegy group g. Protons move from $g = 1$ to $g =$ NG through the problem domain. 39

4.5 Representation of the linear discontinuous Galerkin method. The flux is assumed linear inside the energy groups, and discontinuous on the group faces. Each energy group contains two unknowns, the average of the flux in the energy group $\varphi_{a,g}$ and the slope of the flux inside the energy group $\varphi_{e,g}$. φ_g^- and φ_g^+ are the flux values on the boundaries of the energy group. 40

4.6 Representation of the finite volume method used to evaluate the derivative in the expression of the discretized energy straggling operator. 43

5.1 Representation of the particle flow through the spatial and the energy range along ordinate $\hat{\Omega}_N$. In this ordinate the particles stream from left to right through the spatial domain ($\mu_N > 0$), described by the streaming operator L_{str}, and from top to bottem through the energy domain, described by the continuous slowing down operator L_{CSD}. In the iterative method, the flux-values are solved in the direction of these flows. Note that the flows in the spatial domain are reversed if $\mu_n < 0$. The particles streaming out of the final energy group are assumed to deposit their energy locally. In this thesis $E_{NG+\frac{1}{2}} = 1$ MeV. No particles stream through the final spatial element if the spatial range is sufficiently large. 45

5.2 Schematic representation of the energy transport in spatial cell i and ordinate $\hat{\Omega}_n$ with $\mu_n > 0$. The energy streams in and out of the spatial cells carried by the protons through the spatial domain. Due to the scatter interactions, energy is transferred to atomic nuclei and atomic electrons. The secondary protons created in the catastrhopic scatter process can carry their energy to other cells. The terms in red are energy deposition terms, the green one is an energy source term. 49

6.1 The energy plateau boundary conditions used in test case A in the investigation of the discretization requirement for the energy variable. Here, $E_{max} = 100$ MeV. 52
6.2 Left: test case A, error versus width of spatial cell Δx_i for plateau and mono-energetic boundary conditions. Right: test case B, error versus width of spatial cell Δx_i with an S_{40} quadrature set. 54
6.3 Left: energy depending differential flux of an energy plateau boundary condition problem. Right: energy depending differential flux of a mono-energetic boundary condition problem. The 50 group energy structure is more suited to approximate the energy depending differential flux on the left compared to the right. 57
6.4 Left: test case A, error versus energy width ΔE_g. Right: test case C, error versus energy width ΔE_g. 58
6.5 Left: test case B, the angular depending differential flux at the end of the range, $E_{in} = 100$ MeV. Right: test case B, the error versus the number of ordinates N in the quadrature set. 60

7.1 Left: test case A (see table 6.1), dose profile of a mono-energetic pencil beam boundary condition problem. Right: the error we allow in the calculation is the error in the 500 energy group case which corresponds to $\epsilon \leq 10^{-4}$. . . 62
7.2 Left: 100 MeV benchmark calculation, dose distribution. Right: 200 MeV benchmark calculation, dose distribution. 63
7.3 Left: 100 MeV benchmark calculation, angular depending differential flux. Right: 200 MeV benchmark calculation, angular depending differential flux. 63
7.4 Left: T1-weighted MRI scan, sagittal view of a medulloblastoma patient [34]. Right: the 1D geometry used in the treatment plan. 65
7.5 The energy depending differential flux of the protons in the pencil beam at the boundary used in the medulloblastoma calculation. 66
7.6 Left: medulloblastoma case, dose distribution. Right: medulloblastoma case, scalar flux. 67
7.7 Left: medulloblastoma case, angular depending differential flux at various positions in the patient. Right: medulloblastoma case, energy depending differential flux of the protons in bone (x = 1 cm), in the brain (x = 3 cm) and in the tumor (x = 6 cm). 67

A.1 The hyperbolic path of the incident proton around the target nucleus. r is the distance between the proton and the nucleus, θ the angle between proton and nucleus, and Θ is the scattering angle. 75

C.1 Test case A, energy spectrum of plateau boundary condition problem, with and without straggling operator. 80

D.1 Left: test case A, error versus width of spatial cell Δx_i, $E_{in} = 150$ MeV. Right: test case A, error versus width of spatial cell Δx_i, $E_{in} = 200$ MeV. . 81

D.2 Left: test case A, error versus energy width ΔE_g, $E_{in} = 150$ MeV. Right: test case A, error versus energy group width ΔE_g, $E_{in} = 200$ MeV. 81
D.3 Left: test case A, error versus energy width ΔE_g. The slope of the plateau does not influence the discretization requirement. Right: test case A, error versus energy width ΔE_g. f in $\Delta E_g = f \cdot \Delta E_{g+1}$. The uniform energy structure is optimal in most problems. In this case, however, solution can be obtained more efficiently by applying a different energy structure than the uniform one, but the gain is not significant. 82
D.4 Left: test case A, error versus energy width ΔE_g. The error using boundary condition (i) and (ii) is similar, see section 6.3.1. Right: test case C, illustration of the error in the differential flux for several group widths ΔE_g, $E_{in} = 100$ MeV. 82
D.5 Left: test case B, differential flux at the end of the range, $E_{in} = 10$ MeV. The error in the low quadrature is large near $\mu = 1$ and decreases rapidly further away from $\mu = 1$. Right: test case A, Bragg peak position in PMMA. The position of the Bragg peak is used to impose a range in test case C over which the error in a calculation is evaluated. 83

List of Tables

6.1 The three test cases in which we investigate the discretization requirements. The discretization requirement in a variable in the total transport equation is determined by the most strict discretization requirement of the test cases. 50

6.2 General computational set-up of the test cases, where NE_{ref}, NG_{ref}, and N_{ref} are the number of cells in the reference calculation. 51

6.3 Momentum transfer cross section $\sigma_{tr}(E)$ of protons in PMMA with energy E_{in} for test cases B and C and the corresponding range of the protons with through PMMA for test case B. 54

6.4 The quadrature sets used in test case B and the approximate computation time to obtain a solution. f in $w_n = f \cdot w_{n+1}$. $\mu_N = 0.999995$ and $w_N^a = 10^{-5}$. 59

7.1 Computational set-up of the benchmark cases. 62

7.2 Computational set-up of the medulloblastoma case with an S_{40} quadrature set (see table 6.4), with 100 energy groups, a P_{10} order Legendre expansion catastrophic differential scatter cross sections, and a plateau energy boundary condition $\Delta E_p = 30$ MeV, with energy depending differential flux as in figure 7.5. The multi-group stopping powers $S(E_{g\pm\frac{1}{2}})$ are evaluated with equation 3.28, the multi-group momentum transfer cross sections $\sigma_{tr,g} = \sigma_{tr}(E_g)$ are evaluated with equation 3.19, the multi-group catastrophic scatter cross sections $\sigma_{C,g}$ and $\sigma_{C,g'\to g,l}$ are evaluated with the SADCO code. 65

1. Introduction

1.1 Radiotherapy in Treating Cancer Patients

Cancer is a group of various diseases in which cells divide uncontrollably. In economically developed countries, cancer is the number one cause of death. Globally, around 12.7 million cancer cases in 2008 and 7.6 million cancer deaths are estimated by GLOBOCON [12]. The main treatment options are surgery (the physically removing of the cancer), chemotherapy (the use of drugs which are designed to attack the cancer cells), immunotherapy (the use of the immune system to reject the cancer) and radiotherapy (where radiation is used to kill the cancerous cells). Usually, a combination of these treatments is used to achieve optimal results.

1.1.1 Biological Effects of Radiation

Radiotherapy uses ionizing radiation to treat disease tissue in the body. Excitations of the electrons energy structure and ionizations of the molecules occur due to the interaction of the radiation with the tissue of the patient. The effects on the patient of radiation is assumed to be due to the damage of DNA. The damage to DNA can be created either directly or indirectly: direct if an altered electron structure is created (like the fraction of a chemical bond) due to the interaction of the radiation with the DNA, and indirect if the DNA is damaged by free radicals which are created due to the interaction of the radiation with substances in the neighborhood of the DNA. The most important effects of DNA damage are [4]: damage to nitrogenous bases, cross links between DNA-DNA or DNA-protein, single-strand breaks, and double-strand breaks. The cells in the tissue of a patient are able to repair most of the damage due to the radiation; most single-strand breaks are repaired even within the first few minutes. Double strand-breaks, however, are more difficult to repair since the broken of piece of the DNA may not be close to the damaged DNA. The possible consequences of damaged DNA to a cell are roughly [4]: the repair of the damage with full recovery of the cell, the creation of a modified cell, and cell death. Cancerous cells appear to be more sensitive to radiation and are less able to repair the damage compared to normal cells: after radiation, normal cells appear to recover more fully than cancerous cells do. However, normal tissue is affected by the radiation as well, creating modified cells in normal tissue, which may result in undesirable long term side effects for the patient. Especially sensitive to these long term side effects are children as their organs are in a developing state. Also, children are more likely to live longer if cured, increasing the chance of encountering long term side effects. Examples of such long term side effects are: IQ loss, growth hormone deficiency, hypothyroidism, hearing loss, and secondary cancer [39].

1.1.2 Types of Radiation Therapies

Three main types of radiation therapies can be distinguished according to the position of the radiation source [17]: brachytherapy, unsealed source therapy and external beam therapy. Brachytherapy uses sealed sources placed directly in the disease area. In unsealed source therapy, the radiation source is injected into the body or given by (oral) ingestion. External beam therapy makes use of an external beam of particles aimed at the disease side. The four main types of external beam therapies are: fast neutron therapy, electron

therapy, photon therapy, and heavy charged particle therapy.

Fast neutron therapy uses high energy neutrons with an energy typically greater than 20 MeV[42]. Due to the nature of interaction of neutrons with matter (they primarily interact via (n,p) spallation reactions, in contrast to other forms of radiation which primarily interact through excitations and ionizations), this type of treatment is used to treat tumors which are radio-resistant (tumors which do not respond to other forms of radiation). The downside is that neutrons are difficult to aim at the disease side; they cannot be targeted at the tumor side using magnetic fields since they carry no charge. This, and the fact that neutrons contribute to a relatively large dose in front of the tumor, makes neutron therapy only suitable for relatively large, shallow tumors.

Electrons have a finite range through tissue, sparing tissue behind the tumor side[17]. This is a big advantage of electron therapy, since normal tissue as well as possible critical organs behind the tumor can be spared using this type of therapy. However, due to the strong scatter interactions with matter, the electrons deviate strongly from their incident trajectory, making electron therapy only suitable for treating shallow tumors ($<$ 5cm deep). A second disadvantage, due to the strong scatter interactions of the electrons, is that hot and cold spots (spots were the dose is locally very different from the dose in the surrounding tissue) are created in areas were highly heterogeneities are present in the tissue (for example near a bone structure). As a consequence, electron therapy is not suitable for treating tumors lying in or near strong heterogeneous tissue, like a tumor in the head.

The advantage of photons in the use of external beam radiation is the large penetration depth and the skin sparing property[27]. Due to these properties, photon therapy is the most commonly used type of therapy for deep lying tumors ($>$ 5cm deep). The most advanced form of photon therapy is IMRT (Intensity Modulated Radiation Therapy). IMRT uses modulated intensity beams to deliver precise radiation which conform to the three-dimensional shape of the tumor.

The most common form of heavy charge particle therapy is proton therapy. This type of therapy can offer a superior dose distribution compared to the conventional treatment types, as will be demonstrated in the following section.

1.2 Proton Therapy

1.2.1 History of Proton Therapy

Robert Wilson published a proposal[45] in 1946, saying that accelerated protons can be used in radiation therapy on human patients. Only eight years later, the first patient was treated using a particle accelerator built for physics research[8] at the University of California, Berkely. In 1967, Wilson started as director of the National Accelerator Laboratory, which was to create the largest particle accelerator of his time. It quickly came apparent that it was in that time too early to develop a hospital-based treatment facility, since a highly reliable accelerator with little downtime, greatly improved imaging capabilities and extensive computer modeling were necessary, which were not available in that time. In the 1960s, 1970s and 1980s other physics facilities around the world offered proton treatments, but were all based in research laboratories. The first hospital based proton therapy center was built in 1990 in Loma Linda, California at the Loma Linda University Medical Center. As of June 2011, 42 proton therapy centers are world wide in use, which have treated a total of 74000 patients[36].

1.2.2 Proton Beam Dose Deposition Properties

Protons have a couple of interaction properties which make them especially suited for external beam therapy. The first is that, due to their relatively large mass, protons tend to go into a straight line through tissue. This property makes them easy to aim at the

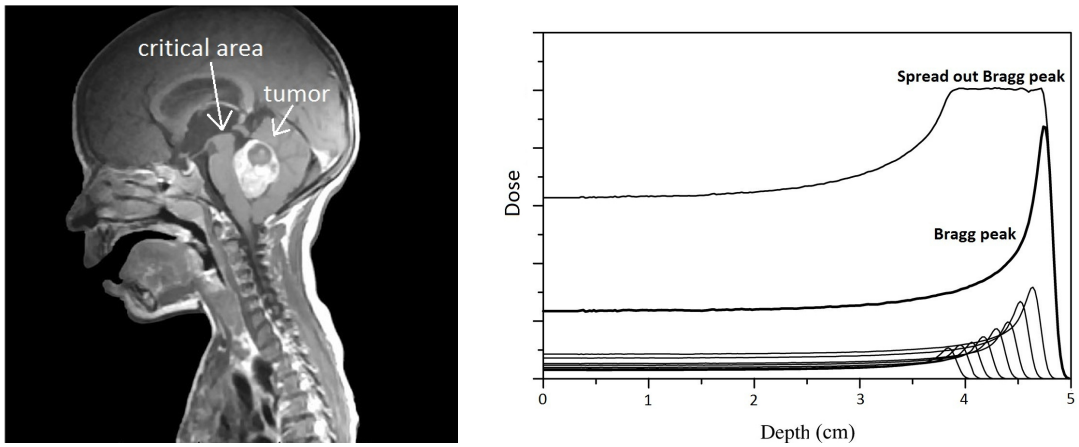

Figure 1.1: *Left: a T1 weighted MRI scan[34] of a 4-year-old medulloblastoma patient. Right: the spread-out Bragg peak (SOBP). Since the size of the tumor is usually large compared to the width of a single Bragg peak, a particle beam with multiple energies is used to obtain energy deposition over the entire range of the tumor.*

tumor side, and suited for use in highly heterogeneous tissue. The second is their relatively low standard deviation in their range through a material: all protons with a certain energy penetrate a material almost over an identical range. This, together with the finite range of protons through tissue results in almost no dose deposition behind the tumor, allowing sparing of critical tissue near the disease area. The third property which makes protons especially suited for therapy is that protons do not interact much with their surrounding until near the end of their range. There, they start to interact very strongly with their surroundings, depositing their remaining energy very locally. This result in the steep rise of deposited dose, known as the Bragg peak, see figure 1.1 (right). In this figure, the Bragg peak is shown as well as the spread-out Bragg peak (SOBP). The Bragg peak is obtained if a mono-energetic proton beam is used. The SOBP is a summation of several Bragg peaks and is obtained by using a proton beam with multiple energies. The SOBP is used to achieve a dose profile over the entire range of the tumor.

An example of a tumor case where proton therapy may give advantages over conventional electron or photon therapy is medulloblastoma. A scan of a medulloblastoma patient is showed in figure 1.1 (left). In this case, the beam needs to go through a highly heterogeneous tissue (which can give problems using electron therapy), and critical area is present lying behind the tumor, which is difficult to spare using photon therapy as we will demonstrate in the following section.

1.2.3 Proton Therapy Compared to IMRT

The most advanced and common type of photon treatment used is IMRT. In principle, proton therapy can offer a superior dose distribution compared to photons. This is illustrated in figure 1.2 (left) where the dose distribution of a photon beam is compared to the dose distribution of a proton beam. The entrance dose of the proton beam is small compared to the entrance dose of the photon beam, the energy deposited in the tumor by the proton beam is large compared to the photon beam, and the exit dose of the proton beam is very small compared to the photon beam. In figure 1.2 (right), a treatment plan of a medulloblastoma patient of proton therapy is compared to IMRT. In this case, a superior dose profile is obtained by the proton treatment plan, much more sparing the critical organs lying behind the tumor (eyes, brain, nerves).

A number of studies show that more tissue is spared in proton therapy compared to IMRT and conventional photon therapy [7] [25] [26]. On the other hand, not enough data is available to provide scientific proof of reduced risk in proton therapy. From the data avail-

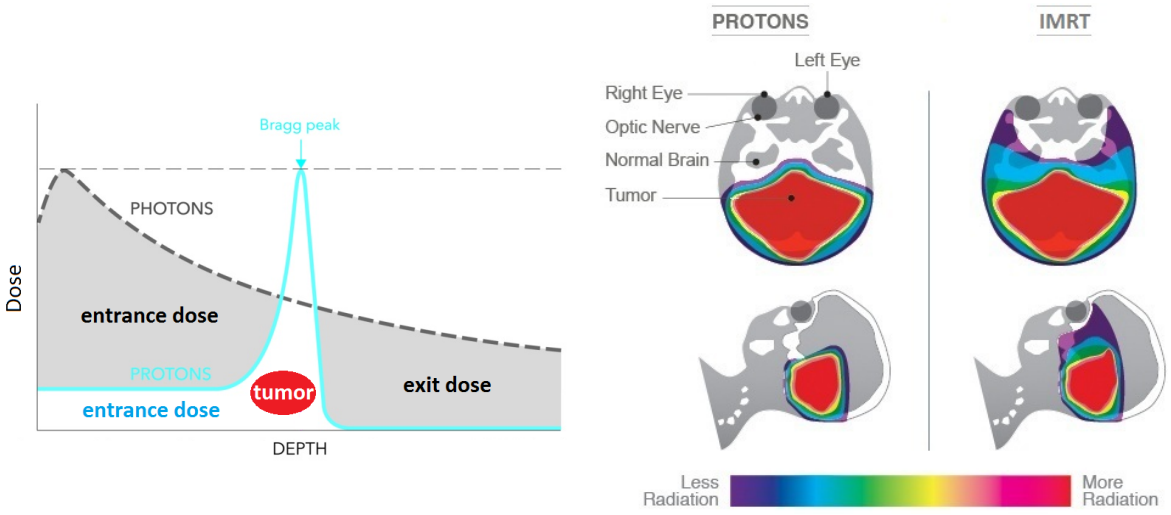

Figure 1.2: *Left: dose distribution of photons compared to the dose distribution of protons*[6]*. Right: proton therapy treatment plan compared to a photon therapy treatment plan*[35]*. The critical organs in the human head are much more spared using proton therapy.*

able, not all cases indicate a lower risk compared to photon therapy. Extensive randomized clinical evidence that protons provide better clinical outcomes compared to photons are available only for ocular, brain and pediatric tumors [48]. Proton therapy is most promising in reducing the long term effects of treatment pediatric tumors [29] [13] [30]. Examples of such treatments by which much is to be gained in sparing normal tissue are: retinoblastoma, medulloblastoma, and rhabdomyosarcoma.

Disadvantages of proton therapy exist as well. First, proton therapy is estimated to be 2.4 times more costly compared to IMRT [39]. However, the costs of the long term side effects of the patient are not incorporated in this estimation. Second, in proton therapy, a relatively large number of secondary neutrons are created. These neutrons may increase the chances of the patient developing secondary cancer, however, no clinical data supports this argument. Third, errors in aiming the proton beam can result in a relatively large dose deposition in normal tissue. To prevent unnecessary dose in normal tissue, there is a need for accurate treatment planning.

1.3 Treatment Planning

1.3.1 Conventional Methods of Treatment Planning

Treatment planning is the process of simulating a delivery strategy for a radiation treatment with as goal to find the optimal treatment plan. There are three primary models for the calculation of the dose profile of a proton beam [20]: uniform-intensity beam algorithms, pencil-beam algorithms and the Monte Carlo method. The uniform-intensity beam algorithms are the simplest and fastest of the three models. They are also the least accurate, especially in estimating the effects of complex heterogeneities on the final dose distribution. This algorithm uses experimentally measured data or numerical fits of dose profiles of a proton beam on a water equivalent phantom. Pencil-beam algorithms are more accurate. In this algorithm, the incident beam is modeled using a set of closely-spaced pencil beams. The broadening of the beam is modeled with the use of experimental data. The resulting dose is computed by adding the dose of the individual contributions from each beam. The uncertainty, however, is very difficult to evaluate using this method. The Monte Carlo method is very accurate. In this approach, individual protons are tracked as they penetrate through the patient. Tens of millions of histories usually must be traced, which can take hours or even days to process. This large computation time hampers the

use of the Monte Carlo methods in the clinics.

1.3.2 The S_N Method

In this thesis, an alternative method for planning proton therapy is investigated: the deterministic method, or discrete-ordinates method, or S_N method. This method refers to the way a solution of the transport equation is obtained. The transport equation, which is, in this case, the linear Boltzmann equation, contains operators which describe the interaction processes of the particles. These operators contain scatter cross sections, which express the likelihood of such interaction process taking place. In the S_N method the direction of travel of the particles is approximated by a finite set of discrete ordinates. Subsequently, the equation is discretized in all of its independent variables. The result of this discretization process is a set of coupled equations describing the particle field in the problem domain. By solving the resulting set of equations, the solution of the transport equation is approximated. In principle, this method offers a similar level of accuracy as the Monte Carlo method does, but has some advantages: it can be considerably faster; it delivers the dose distribution in the entire region of simulation; different optimization techniques are available due to the formulation; and it is suitable for sensitivity analyzes used to quantify uncertainty in a solution due to the movement of the patient and the uncertainties in the chemical composition of the human body on the delivered dose.

The S_N method was first developed by nuclear reactor physicists to calculate the distribution of neutrons in a reactor core. In our work, this method is used to calculate the proton distribution in the patient. Due to the charge of the proton, the nature of interaction with matter is different from the neutron. The Coulomb forces work over a relatively long range, resulting in a large number of small angle scatter interactions. This behavior of the proton is expressed in nearly singular differential cross sections of this scatter process. In the S_N method, it is common practice to expand the differential cross section into Legendre polynomials. However, an unrealistic number of polynomials are necessary to accurately describe the nearly singular shape. The Fokker-Planck approximation of the linear Boltzmann equation is used to overcome this issue. In this approximation, the linear Boltzmann equation is transformed into the Fokker-Planck equation, with the Fokker-Planck operators describing the small angle Coulomb scatter interactions with the atomic nuclei and the small energy transfers to the atomic electrons. Due to the approximation, there exists no need to expand the nearly singular differential scatter cross section into a Legendre series.

1.4 Goals of this Thesis

The goal of this thesis is to investigate the applicability of the S_N method to the use of proton therapy planning, and if it can replace and augment the Monte Carlo method. Therefore, the main question of this thesis is:

Is the S_N method accurate enough to replace the Monte Carlo method in proton therapy planning, and what underlying methods need to be improved to reach its potential computation speed?

To answer this question, the available models for describing charged particles transport and the methods for solving the transport equation are investigated on accuracy for proton transport calculations in the energy range considered in proton therapy (which is 0 - 200 MeV). This investigation can be divided into four parts. In the first part (chapters 2 and 3), the available models for describing the charged particle interaction processes are investigated. The models adopted in our work are used to evaluate scatter cross sections, which are validated by comparing them to literature values. Also, the validity of the Fokker-Planck operators are tested for the energy range considered in proton therapy.

In the second part (chapters 4 and 5), the methods are presented which we used to solve the transport equation. In chapter 4, three discretization methods are presented: the S_N method, the step scheme and the discontinuous Galerkin method, which are used for discretization of the angular, spatial and energy variable in the 1D transport equation respectively. The result of this discretization procedure is a set of coupled equations. In chapter 5, the method to solve the set of coupled equations is presented. From this solution the dose profile can be calculated. In the third part (chapter 6), the discretization requirements are tested for mono-energetic, and plateau boundary condition problems. In the final part of this thesis (chapter 7), the results of the previous investigations are used to set up two benchmark cases. In the final section of the thesis, the S_N method is used to calculate a proton treatment plan for the medulloblastoma patient in the scan of figure 1.1 (left). Based on this investigation, the main question is answered in the final chapter of this thesis. Also recommendations are made for future work regarding investigations which need to be performed in order to improve the S_N method and make it ready to be implemented in the clinics.

This report is part of a master thesis research of Technology University of Delft at the department of Physics of Nuclear Reactors at the Reactor Institute Delft.

2. Proton Interactions with Matter

The basis for the therapeutic suitability of proton therapy is the interaction of protons with matter. Protons have a high ionization rate at the end of their range, they have a tendency to go in a straight line through tissue, and the standard deviation in the range of the protons is very low. These properties of interaction enable us to accurately aim a proton beam at the tumor side while sparing the surrounding normal tissue.

Protons interact with matter through various mechanisms: elastic and inelastic Coulomb scatter with atomic nuclei, with atomic electrons, with the atom as a whole and through catastrophic scatter interactions with the nuclei. In these interactions energy gets lost, the path of direction changes and secondary particles are created. In modeling these interaction processes we require differential scatter cross sections. These cross sections express the likelihood of any type of interaction taking place. With these cross sections we have all the information one needs to model proton therapy. In this chapter we present the interaction processes which are important in the energy range considered in proton therapy, and how to obtain the differential cross sections to describe these interaction processes.

2.1 Elastic Interactions with the Nucleus

The incident proton interacts with the nucleus through Coulomb forces. Due to these forces, the incident proton deviates from its original path of direction, and some energy is transferred during these elastic interactions to satisfy conservation of momentum. As we will encounter later on in the thesis, this energy loss is very small compared to the energy lost in the inelastic interactions with the atomic electrons. For this reason, the focus of this section is on the angular deflection of the incident proton.

Rutherford derived differential cross sections for the elastic scatter process from the classical equations of motion [11]. Here we present its derivation mainly following the work of Goldstein [14], starting with the relation between the scattering angle Θ and the impact parameter b:

$$b = \cot\left(\frac{\Theta}{2}\right)\frac{Z_i Z_t e^2}{4\pi\epsilon_0 m_0 v_0^2}. \tag{2.1}$$

How to derive this relation can be found in appendix A. The impact parameter b is the closest distance between the incident proton and the target nucleus, if the proton does not deflect from its original trajectory. The scattering angle is the angle between the proton's original trajectory, and the proton's trajectory after interacting with the nucleus, see figure 2.1. Z_i and Z_t are the charge counts of the incident and the target particle respectively, ϵ_0 is the vacuum permitivity, v_0 is the initial velocity of the incident particle in the laboratory frame of reference, e is the elementary charge and m_0 is the reduced mass of the incident particle:

$$\frac{1}{m_0} = \frac{1}{m_i} + \frac{1}{m_t} \tag{2.2}$$

where m_i is the mass of the incident particle (which is the proton in this thesis), and m_t is the mass of the target nucleus.

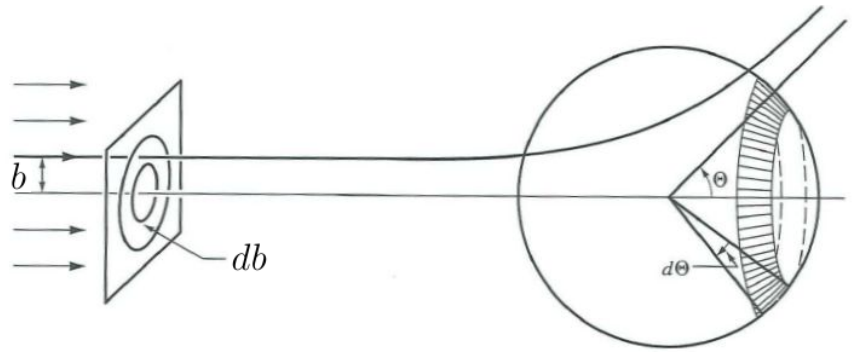

Figure 2.1: *The trajectory of an incident proton with impact parameter b, interacting with a particle through the Coulomb force. The proton is scattered in angle* Θ.

The scattering angle Θ is uniquely determined for an energy E and an impact parameter b. To determine the differential cross section from this result, we consider its definition:

$$\frac{d\sigma}{d\Omega} = \frac{\text{number of particles scattered into solid angle } d\Omega \text{ per unit time}}{\text{incident intensity}}. \tag{2.3}$$

Consider the situation depicted in figure 2.1. The number of particles going through the area $2\pi b db$ on the left hand side of the picture is equal to the number of particles passing the area of the sphere on the right hand side of the picture: $2\pi \sin\Theta d\Theta$. So the number of particles scattered into solid angle $d\Omega$ per unit time is equal to the ratio of the two areas multiplied by the incident intensity of protons: $I\frac{b}{\sin\Theta}\frac{db}{d\Theta}$. Substituting this into the definition of the differential cross section in equation 2.3, we obtain:

$$\frac{d\sigma}{d\Omega} = \frac{b}{\sin\Theta}\frac{db}{d\Theta}. \tag{2.4}$$

We use this result together with equation 2.1 to obtain the Rutherford differential scattering cross section:

$$\sigma'_e(\Theta) = \frac{d\sigma}{d\Omega} = \left(\frac{Z_i Z_t e^2}{8\pi\epsilon_0 m_0 v_0^2}\right)^2 \csc^4\left(\frac{\Theta}{2}\right) = \left(\frac{Z_i Z_t e^2}{4\pi\epsilon_0 m_0 v_0^2}\right)^2 \frac{1}{4\sin^4\left(\frac{\Theta}{2}\right)}. \tag{2.5}$$

Using the trigonometric identity $\sin^4(\Theta) = \frac{(1-\cos(2\Theta))^2}{4}$, the Rutherford differential cross section takes its final form:

$$\sigma'_e(\Theta) = \left(\frac{Z_i Z_t e^2}{4\pi\epsilon_0 m_0 v_0^2}\right)^2 \frac{1}{(1-\cos(\Theta))^2}. \tag{2.6}$$

This result however, cannot be put into direct use. The Rutherford differential cross section is singular at a scattering cosine of unity. As a consequence, the total elastic scattering cross section $\sigma_{e,s}$ is infinite as well:

$$\sigma_{e,s} = \int_{4\pi} \sigma(\Omega) d\Omega = 2\pi \int_0^\pi \sigma'_e(\Theta)\sin(\Theta) d\Theta = \infty. \tag{2.7}$$

Physically, this makes sense: the total scatter cross section is the total number of particles scattered in all directions per unit time for unit incident intensity. The range of the Coulomb force is infinite. Therefore the incident particles show small deflection angles due to interactions with particles which have large distances between them: the scattering field is nonzero at all distances. So, $\sigma_{e,s}$ is finite only when a cutoff in the scattering field occurs. Physically, a cutoff occurs in the Coulomb field, as a result of the bound

atomic electrons surrounding the nucleus. Those electrons screen the nucleus, canceling the charge of the nucleus outside of the atom. A lower bound on Θ can be set if one accounts for the screening of the nucleus [38].

$$\Theta_{min} = \frac{Z_t^{\frac{1}{3}} \alpha m_e c}{p} \tag{2.8}$$

Here, p is the momentum of the incident particle, and α is the fine structure constant. This constant is a measure of the strength of the electromagnetic force that governs the interaction of electrically charged elementary particles. Goudsmit and Saunderson [16] included this minimal scattering angle into the analysis to obtain the cross section which is called the screened Rutherford cross section:

$$\sigma_e'(\Theta) = \left(\frac{Z_t Z_i e^2}{4\pi\epsilon_0 m_0 v_0^2} \right)^2 \frac{1}{(1 - \cos(\Theta) + 2\eta)^2} \tag{2.9}$$

with,

$$\eta = \Theta_{min}^2. \tag{2.10}$$

This result is not singular at a cosine of unity. It contains the information on the angular deflection of the incoming protons due to the Coulomb interaction with the atomic nuclei. Keen [21] demonstrated this cross section to be very accurate for heavy charged particles, like protons, for energies above 1 MeV. For energies under 1 MeV, however, the accuracy deviates significantly. In this work 1 MeV is used as the cutoff energy; the paths of the incident protons are modeled until they reach the energy of 1 MeV, after which the protons are assumed to deposit their remaining energy locally. Since the range of a 1 MeV proton in soft tissue, such as the tissue in the human body, is approximately 10^{-3} cm [4] (p. 53), this approximation is well justified.

2.1.1 Transformation of Reference Frame

Before we proceed any further, it must be noted that this analysis so far is done in the center-of-mass frame. However, it is desirable to have an expression of the cross section in terms of the scattering angle measured in the laboratory frame. In the work of Goldstein [14], a relation is derived which expresses Θ in terms of the scattering angle measured in the laboratory frame ϑ. For protons this relation is:

$$\cos(\vartheta) = \frac{\cos(\Theta) + \frac{m_p}{m_t}}{\sqrt{1 + 2\frac{m_p}{m_t}\cos(\Theta) + \left(\frac{m_p}{m_t}\right)^2}} \tag{2.11}$$

with ϑ the scattering angle measured in the laboratory frame and m_p the mass of the proton. This relationship is shown in figure 2.2 for protons interacting with different target masses with mass m_t. An important conclusion can be drawn from the analysis depicted in this figure: since the mass of an arbitrary nucleus and of the incident proton is very large compared to that of an electron, the angular deflection due to scatter with atomic electrons is negligible compared to the angular deflection by the atomic nuclei. This is demonstrated by substituting the electron mass m_e as the target mass m_t in equation 2.11. For every deflection angle in the center-of-mass frame, the cosine deflection angle in the laboratory frame is approximately equal to unity. This is taken advantage of in modeling proton transport, as we will encounter in the next section.

The differential cross section in equation 2.9 has to be expressed in the scatter angle measured in the laboratory frame of reference. Since the number of particles scattered

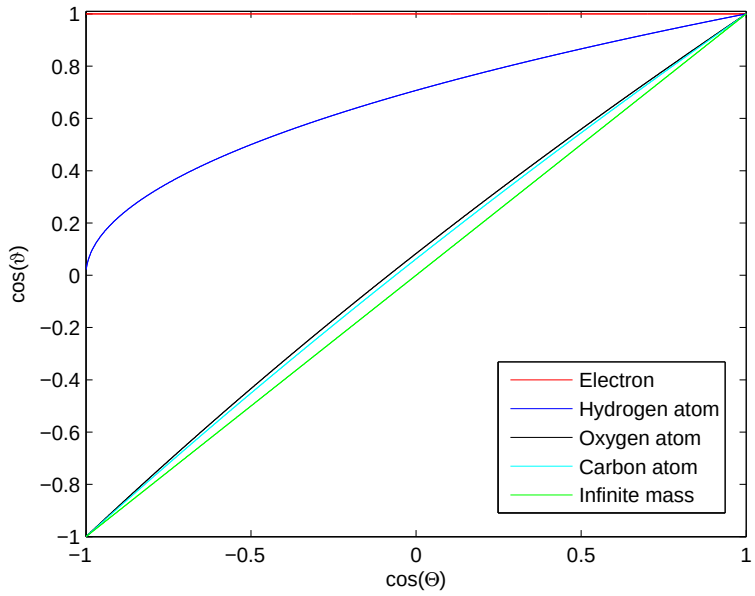

Figure 2.2: *Relation between the cosine scattering angle* $\cos(\Theta)$ *of the incident proton measured in the center-of-mass frame, and in the laboratory frame* $\cos(\vartheta)$ *for different target nuclei.*

into a solid angle must be the same in every coordinate system, we obtain the following relation:

$$2\pi I\sigma_e'(\Theta)\sin\Theta d\Theta = 2\pi I\sigma_e(\vartheta)\sin\vartheta d\vartheta \tag{2.12}$$

or,

$$\sigma_e(\vartheta) = \sigma_e'(\Theta)\frac{\sin\Theta}{\sin\vartheta}\frac{d\Theta}{d\vartheta} = \sigma_e'(\Theta)\frac{d\cos\Theta}{d\cos\vartheta} \tag{2.13}$$

where σ_e is the differential elastic scatter cross section expressed in the scattering angle in the laboratory frame of reference. The derivative in 2.13 can be evaluated with equation 2.11:

$$\sigma_e(\vartheta) = \frac{\left(1 + 2\frac{m_p}{m_t}\cos\Theta + \left(\frac{m_p}{m_t}\right)^2\right)^{\frac{3}{2}}}{1 + \frac{m_p}{m_t}\cos\Theta}\sigma_e'(\Theta). \tag{2.14}$$

The correction term on the right hand side of this equation transforms the scatter cross section measured in the center-of-mass frame to the scatter cross section measured in the laboratory frame. This correction term is plotted in figure 2.3 for incident protons interaction with various nuclei. From this figure, we see that the scatter angle measured in the center-of-mass frame differs only 10% from the laboratory frame for most nuclides considered in proton therapy. However, for a hydrogen nucleus this correction factor is maximum 4.

Now we have derived the final form of the screened Rutherford differential cross section for protons ($Z_i = 1$) expressed in the scattering angle in the laboratory frame,

$$\sigma_e(\mu_0) = \frac{\left(1 + \frac{2\mu_0}{A_t} + \frac{1}{A_t}^2\right)^{\frac{3}{2}}}{1 + \frac{\mu_0}{A_t}}\left(\frac{Z_t e^2}{4\pi\epsilon_0 m_0 v_0^2}\right)^2 \frac{1}{(1 - \mu_0 + 2\eta)^2} \tag{2.15}$$

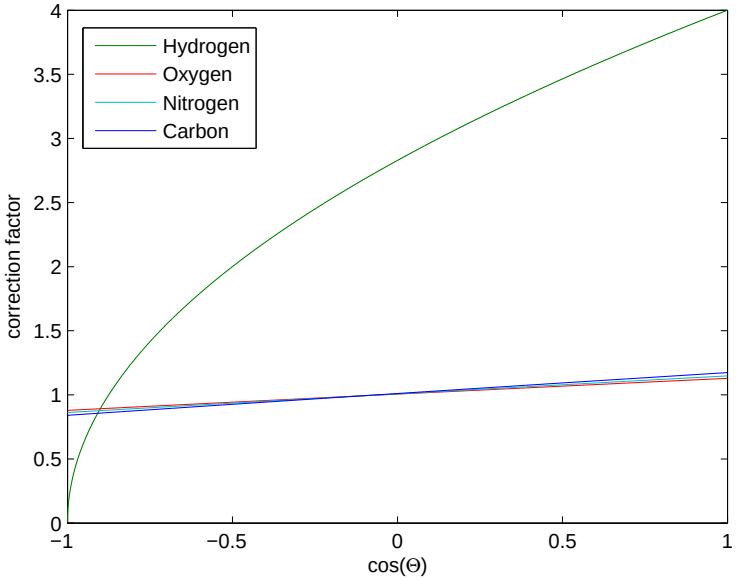

Figure 2.3: *Correction factor for transformation of differential cross section expressed in coordinates in the center-of-mass frame to the differential cross section expressed in coordinates in the laboratory frame for protons incident of a nucleus, see equation 2.14.*

with A_t the mass number of the target nucleus and $\mu_0 \equiv \cos(\Theta)$ the cosine of the deflection angle.

The screened Rutherford scatter cross section is plotted in figure 2.4 for protons incident on water. As can be seen from this figure, the cross sections are extremely forward peaked: the cross sections are nearly singular for angles near $\cos(\Theta) = 1$. Physically, this represents the large number of scatters of the incident proton with a small angular deflection, and a very few number of large angle scatters. This forward peaked nature of the screened Rutherford differential cross section causes difficulties in modeling this interaction process, as we will encounter in the next chapter.

We deliberately did not elaborate on the energy lost by the incident proton in this interaction process, since it turns out to be negligible compared to the energy lost in the elastic scatter interaction process with the atomic electrons. This is demonstrated in the next section.

2.2 Inelastic Interactions with Atomic Electrons

The incident proton interacts with the atomic electrons through the Coulomb forces. This interaction process is inelastic, since energy is used to alter or break the bond between the atomic electrons and its nucleus. As for the elastic scatter of atomic nuclei, we would like to derive differential cross sections for the interaction process of the incident proton with the atomic electrons.

Two types of collisions with atomic electrons can be distinguished: hard collisions and soft collisions. In a hard collision, the binding energy of the electron is negligible compared to the energy transferred to the electron. Therefore, the electron can be seen as free, which greatly simplifies the analysis. Soft collisions, on the other hand, are the collisions in which the binding energy of the electron is not negligible compared to the energy transferred in the collision. In the case of soft collisions, the electron must be treated as bound. This type of interaction is more difficult to model.

In both types of collisions, energy is transferred from the proton to the electrons, and the proton gets deflected from its original direction of movement. However, as we have

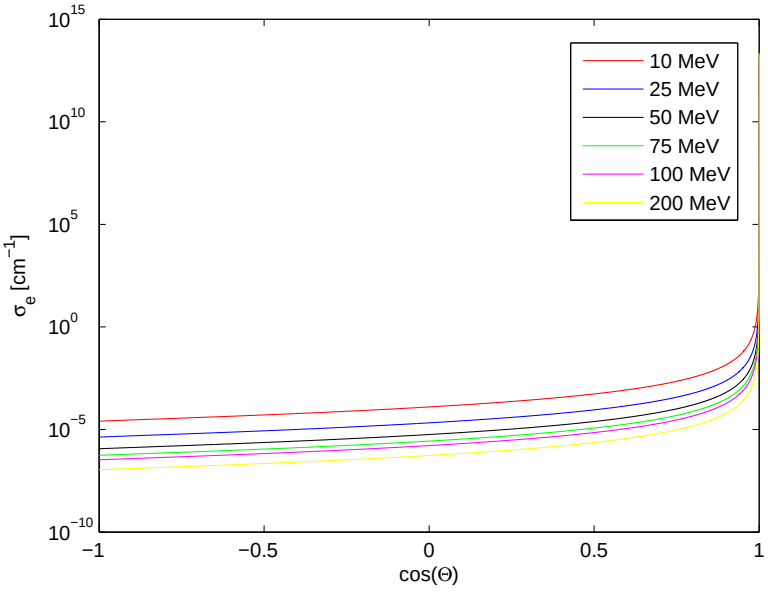

Figure 2.4: *Screened Rutherford cross section for incident protons on water for various energies. The cross sections are nearly singular at* $\mu_0 = 1$.

seen in the previous section, the angular deflection in this process is negligible compared to the angular deflection due to interaction with the atomic nuclei. Therefore, the focus of this section is on the energy transferred from the incident proton to the atomic electrons.

2.2.1 Hard Collisions

In a hard scatter collision, the energy transferred from the incident proton to an atomic electron is much larger than the binding energy of that electron. As a consequence, the electron can be treated as if it were free, and the collision can be considered elastic. Elastic scatter can be modeled with the Rutherford cross section derived in the previous section. This analysis follows the work of Evans [11].

Because the velocity of the incident proton is several orders of magnitude larger than the velocity of the bound electron, the electron may be considered a stationary particle. Therefore, the energy of the electron after the collision is equal to the energy lost Q by the incoming proton:

$$Q = \frac{1}{2} m_e v_e^2. \tag{2.16}$$

From the conservation laws, a relation can be derived between the energy lost Q by the incident proton and its deflection angle Θ [11]:

$$Q = \frac{1}{2} m_e \left(\frac{2 v_0 m_0}{m_e} \right)^2 \sin^2 \frac{\Theta}{2}. \tag{2.17}$$

The differential of this energy loss:

$$dQ = 2 \frac{v_0^2 m_0^2}{m_e} \sin \frac{\Theta}{2} \cos \frac{\Theta}{2} d\Theta \tag{2.18}$$

substituting into equation 2.6 the value of $\cos \frac{\Theta}{2} d\Theta$ of the above equation and the value of $\sin^2 \frac{\Theta}{2}$ from equation 2.17 leads to:

$$\sigma_{in,hard}(Q) = \frac{d\sigma_{in,hard}}{dQ} = \frac{2\pi e^4}{(4\pi\epsilon_0)^2 m_e v_0^2} \frac{1}{Q^2}. \tag{2.19}$$

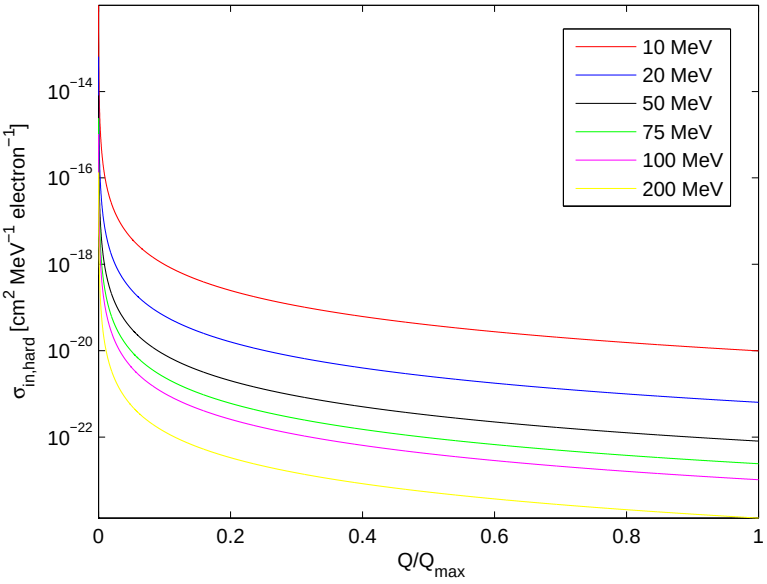

Figure 2.5: *Screened Rutherford cross section for hard collisions between incident protons and electrons for various energies. The cross sections are nearly singular at $Q = 0$.*

Here, we have derived a simple formulation for the energy loss of the hard collision between an incident proton and an atomic electron. In figure 2.5 this differential cross section is plotted for protons incident on water. As can be seen from this figure, this cross section is nearly singular near $Q = 0$. Physically this represents the large number of interactions with a small amount of energy transferred from the proton to the electron. Note that, although this energy transfer near $Q = 0$ is small compared to the maximum energy transferred from proton to electron Q_{max}, it is still very large compared to the binding energy of the electron. Therefore, the collisions can still be seen as hard, relatively close to $Q = 0$ in the figure. In the energy range in the order of magnitude of the electrons binding energy, however, the collisions can no longer be considered hard, and we have to apply a different analysis.

2.2.2 Soft Collisions

A large amount of soft scatter interactions take place between the incident proton and the atomic electrons. In these interactions, the distance between the incident proton and the electrons is relatively large, and the energy transferred to the electron is relatively small. Therefore, unlike in hard collisions, the electron must be regarded as bound. So, instead of considering the energy transferred to just the electron, one should consider the energy transferred to the system formed by all of the electrons and nucleons in the atom. In other words, the protons interact with the atom as a whole.

The two most prominent theories on soft collision scatter are derived by Bohr and Bethe[28]. Bohr treated the atomic electrons as harmonic oscillators. The energy lost by the incident particles is calculated using classical electrodynamics. Bethe performed his analysis through detailed quantum-mechanical calculations using the Born approximation. In the energy range considered in proton therapy, Bethe's theory is in best agreement with experimental results[28]. Therefore, his theory is adopted in this thesis. For a detailed derivation of the soft scatter differential cross section, the reader is referred to the work of McPalrand[28]. Because of the complexity of this derivation, only the final result is

presented here:

$$\sigma_{in,soft}(Q) = \frac{d\sigma_{in,soft}}{dQ} = \frac{2\pi e^4}{(4\pi\epsilon_0)^2 m_e v_0^2}\frac{1}{Q}\frac{df_n}{dE_n} \tag{2.20}$$

where $\frac{df_n}{dE_n}$ represents the generalized oscillator strength (GOS) per unit energy transfer, which is a generalization of the optical oscillator strength. Physically this dimensionless quantity expresses the strength of the transition from one quantum state of the atom to another.

The total differential cross section is obtained by adding the effect of the soft collision scatter with the hard collision scatter:

$$\sigma_{in}(Q) = \sigma_{in,soft}(Q) + \sigma_{in,hard}(Q) = \frac{2\pi e^4}{(4\pi\epsilon_0)^2 m_e v_0^2}\left(\frac{1}{Q}\frac{df_n}{dE_n} + \frac{1}{Q^2}\right). \tag{2.21}$$

In the previous section, we concluded that the process of angular deflection was dominated by elastic scatter of atomic nuclei. A second important conclusion can be drawn from the result in equation 2.21: the process of energy loss is dominated by the inelastic scatter of atomic electrons. This is demonstrated by replacing the mass of the electron by the mass of any arbitrary nucleus. Since the mass of the nucleus is at least 1836 larger than the mass of the electron, this cross section is negligible small compared to the cross section of the scatter of atomic electrons. So, the energy lost by the incident proton is dominated by the process of inelastic scatter with the atomic electrons. In modeling proton transport, advantage is taken from these differences in nature of these processes; the energy loss of the incident proton in the interaction process with the atomic nuclei can be neglected compared to the energy lost to the atomic electrons. In modeling the angular deflection of the proton, on the other hand, the interaction process with the atomic electrons can be neglected compared to the interaction with the atomic nuclei. Separation of these physical processes greatly simplifies the modeling of proton transport, as we will see in the next chapter.

2.3 Inelastic Interactions with the Nucleus

Two types of inelastic interactions with the nucleus can be distinguished: catastrophic scatter reactions, and interactions which result in bremsstrahlung. For the energy range in proton therapy bremsstrahlung is a small and negligible process [11] (p. 632). Catastrophic reactions, on the other hand, are not negligible. In these reactions, the incident proton penetrates the nucleus interacting with the individual nucleons. In this interaction process the proton can get absorbed and various secondary particles can be created such as electrons, neutrons, photons, secondary protons, and also heavy fragments. Some of these secondary particles will deposit their energy locally, other particles deposit their energy over a large range, contributing to a secondary dose. This secondary dose is small compared to the primary dose of the incident protons. However, we should not ignore it as this dose may be deposited in surrounding tissue where critical organs may be present. So, to acquire an accurate dose deposition profile, the paths of these secondary particles with significant range and energy have to be modeled as well. The differential cross section containing the information on catastrophic scatter reactions are, for the purpose of this thesis, generated by the SADCO [15] code.

2.3.1 The SADCO Code

The SADCO [15] system is a code developed to prepare multi-group cross sections for deterministic multi-group calculations. This algorithm is based on an approximation of the available experimental data, accumulated in RD [10] and SADCO nuclear databases, and calculated data using nuclear models.

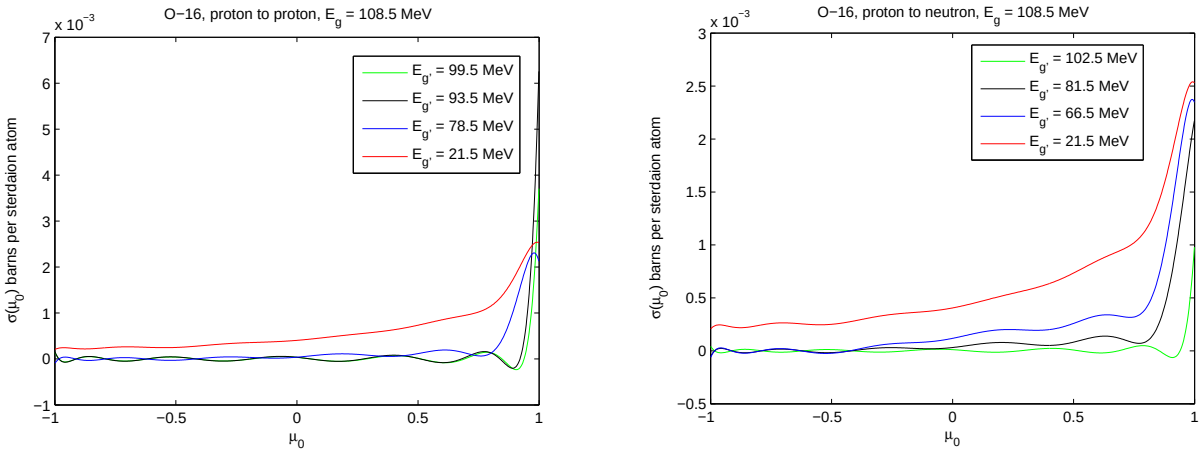

Figure 2.6: *Multi-group coupled differential cross sections expanded in a P_{11} Legendre series, evaluated with the SADCO code. Left: proton to neutron cross sections from energy group g to g'. Right: proton to proton cross sections from energy group g to g'.*

For the purpose of this thesis, the SADCO code is used for generating coupled multi-group cross sections for the catastrophic scatter interaction process, for protons, pions and neutrons in the energy range of 20−200 MeV. To illustrate the data of SADCO, in figures 2.6 and 2.7 multi-group cross sections from a cross section library with 3 MeV wide energy groups are shown, where E_g is the center energy value of energy group g. The cross section are expanded in a P_{11} Legendre series, which is the standard number of Legendre moments generated by the SADCO code.

Figure 2.6 (left) shows differential cross sections from incident proton to secondary proton. The truncation of the Legendre series is clearly visible in the bumpy shape of these cross sections, suggesting that the cross sections are not completely faithfully represented by the P_{11} Legendre expansion. In future work, the validity of these cross sections should be confirmed by literature values, or by cross sections evaluated with a different code, for example MCNPX.

Figure 2.6 (right) shows differential cross sections from incident proton to secondary neutron. Just as in the proton to proton differential cross sections, the truncation of the Legendre series is clearly visible in the bumpy shape of these cross sections.

The differential cross sections for protons incident on hydrogen are shown if figure 2.7 (left). The alternating shape and the negative values suggest these cross sections to be unphysical. This problem is discussed in the following section.

The total cross sections of the catastrophic scatter process $\sigma_{C,s}$ is shown in figure 2.7 (right). This total cross section expresses the likelihood of any catastrophic scatter interaction taking place for particles carrying energy E, including absorption. These cross sections increase with an decreasing energy. Below the 20 MeV these cross sections decrease in magnitude [22]. These values are similar compared to the values for the total cross sections evaluated in the work of Kesley [22].

Problems Encountered Using the SADCO Code

Four problems were encountered in using the SADCO code for the purpose of describing the catastrophic scatter interaction process of protons in the energy range considered in proton therapy:
(i) The coupled differential cross sections generated by the SADCO code suggest no secondary particles other than protons and neutrons are created. However, experiments show that photons are created [33], as well as some other more heavy fragments. These heavy fragments are likely to deposit their energy very locally, and can therefore be ignored in

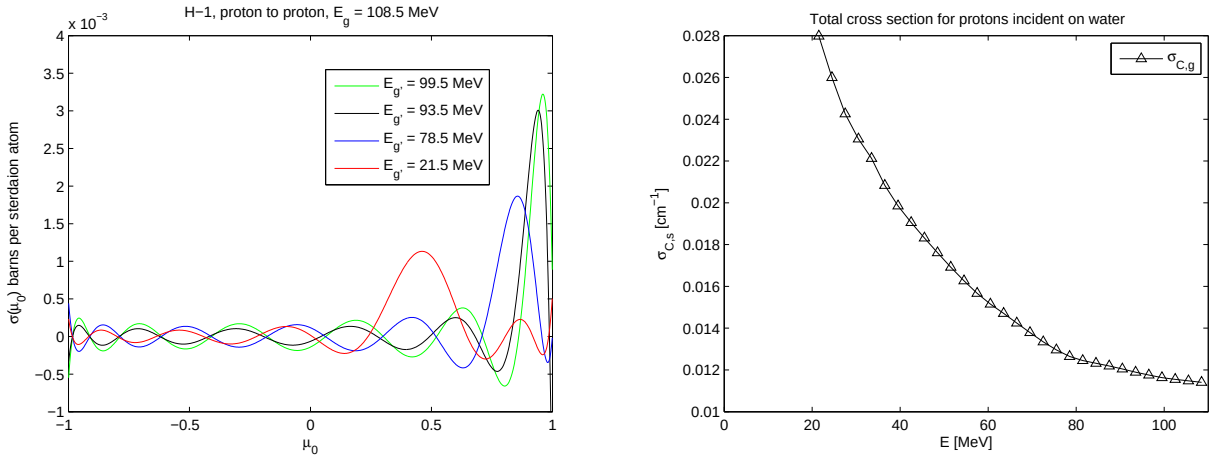

Figure 2.7: *Multi-group coupled differential cross sections expanded in a P_{11} Legendre series, evaluated with the SADCO code. Left: proton to proton cross sections on hydrogen from energy group g to g'. Right: multi-group total cross sections for protons incident on water.*

the modeling process. The photons, on the other hand, do not deposit their energy locally. It is desirable to obtain information about the creation of photons for two reasons: first, the energy of these photons is deposited over a large range, contributing to a secondary dose in parts of the patient where critical organs may be present. Second, the creation of prompt photons can be used to verify the calculated particle field. This is used to verify the treatment plan during treatment. This is important since small errors in the treatment plan can lead to significant dose in normal tissue and, therefore, these small errors need to be detected during treatment. However, although it is desirable to have this information on these secondary photons, it is not strictly necessary for the purpose of our work. Therefore, this problem is accepted in this thesis.

(ii) The differential scatter cross sections for protons incident on a hydrogen nucleus have a strange and unphysical shape, see figure 2.7 (left). Since the hydrogen nuclide is a nuclide frequently encountered in body tissue, it is desirable to have an accurate cross section of this nuclide for the catastrophic scatter process. In future work, other methods to obtain these cross sections should be investigated, for example with the code MCNPX. In this work, however, these cross sections are accepted since the scatter of hydrogen is a small and a relatively unimportant process compared to Coulomb scatter.

(iii) SADCO does not generate catastrophic differential scatter cross sections for energies $E < 20$ MeV. In this thesis, the effects of the catastrophic scatter process is assumed to be small in this energy range and is neglected. This can be justified by noting that low energy protons are less likely to overcome the repelling Coulomb forces of the nucleus [22]. If secondary particles are created by protons with an energy less than 20 MeV, these particles will carry a relatively small amount of energy themselves, and are more likely to deposit their energy locally. So, the missing information in this area is expected to be relatively unimportant. In this work, this incomplete description of the catastrophic scatter process is accepted. However, in future work, differential cross sections for the catastrophic scatter process should be obtained by other means, for example by means of the computer code MCNPX [32], to acquire a more complete description of the particle-field.

(iv) The maximum order of expansion of the differential cross sections generated by the SADCO code is P_{16}. Future studies should verify if this order of expansion is enough to describe the catastrophic scatter process. In this work, however, we only used a P_{10} expansion of the differential scatter cross sections of the catastrophic scatter interaction process. This due to computation and storage space considerations, and we assumed this is an accurate enough description.

So concluding, problems were encountered using the SADCO code and in future work an alternative code should be investigated to obtain differential scatter cross section for the catastrophic scatter process. In this work these problems are accepted, and the SADCO code is used to generate the differential scatter cross sections for the catastrophic scatter process.

2.4 Conclusions

Three main interaction processes of protons with matter are identified: elastic Coulomb interaction with atomic nuclei, inelastic Coulomb interactions with atomic electrons and catastrophic scatter interactions. The energy lost by the protons in the elastic Coulomb scatter of the atomic nuclei is negligible compared to the energy lost in the inelastic Coulomb scatter of the atomic electrons, and vice versa for the angular deflection of the protons. The Coulomb interactions are modeled by Rutherford differential cross sections and by Bethe's theory. This is accurate for energies above 1 MeV. This is an acceptable cut off energy for proton therapy since the typical range of a 1 MeV proton through tissue is short (of the order of 10^{-3} cm).

The catastrophic scatter interactions are modeled by the SADCO code. In this thesis, the problems encountered using the SADCO code are accepted, and the results of the SADCO code are used to describe the catastrophic scatter interaction process. This can be justified since the catastrophic interaction process is relatively unimportant compared to the Coulomb interaction processes. However, in future work, to obtain a more accurate and complete solution of the problem, an alternative code for obtaining these cross sections should be investigated, for example the MCNPX code.

3. Mathematical Description of Proton Transport

The central problem in proton therapy planning is to determine the distribution of the protons in the treatment area. Proton transport is the process in which protons stream from one place to the next and interact with the atomic nuclei and the atomic electrons. The linear Boltzmann equation is the equation which is adopted in this thesis to describe this process. This equation is derived starting from a balance equation of the angular proton distribution. It can be solved analytically for the simplest of problems only. In general, for problems considered in this thesis, the linear Boltzmann equation can only be solved numerically.

In the next section we discuss the underlying assumptions of the linear Boltzmann equation and the physical interpretation of the operators in the linear Boltzmann equation. In the following sections we present an approximation of the linear Boltzmann equation (the Fokker-Planck equation) which enables computer codes to solve the equation using little computation time compared to solving the equation without this approximation. In the final section, we demonstrate the accuracy of the Fokker-Planck equation to be on the verge of validity for the description of angular deflection of the incident protons, after which we discuss a hybrid method to overcome this issue.

3.1 The Linear Boltzmann Transport Equation

3.1.1 Justification of the Underlying Assumptions

Since the linear Boltzmann equation is the basis of all the following work in this thesis, a few words will be spend on the properties of the equation and the assumptions underlying the equation, and on how these assumption can be justified for the purpose of describing proton transport in the energy range considered in proton therapy:

Assumption: the free motion of the particles can be described using classical mechanics. States of the proton, such as spin, do not influence the free movement of the proton in the energy range considered in proton therapy.

Assumption: only binary collisions take place; three body collisions are assumed to be negligible. This can be justified since the proton density is in the order of magnitude of 10^{10} cm^{-3}, while the atom density of a typical tissue is around the 10^{23} cm^{-3}, making the occurrence of a three or more body collision very unlikely.

Assumption: no proton-proton interaction can take place. Protons interact with each other through the Coulomb forces, which can extend over a long range. However, since the large number of atoms present in tissue compared to the number of free protons, the charges of the protons get screened from each other by the atomic electrons, interfering with the protons to have long range Coulomb interactions.

Assumption: the properties of the host medium are not altered. This can be justified since the catastrophic scatter cross sections are small (catastrophic scatter is the process which alter the material properties), and the number of protons are small compared to the number of atoms. As a consequence, the number of atoms which are altered during the treatment is small, and so the properties of the material are not altered significantly.

Property: the linear Boltzmann equation only describes the mean particle density distribution. Fluctuations in the distribution are present, since the interaction of protons with matter is a stochastic process. To capture these fluctuations, other terms in the equation are necessary. But since we are only interested in the total deposited energy, which can be obtained by integrating the average dose deposition over time, we are not interested in capturing the fluctuations in the delivered dose per unit time, but only in the average delivered dose per unit time.
Since these assumptions can be justified for the interest of proton therapy, and the equation is known to be very accurate for neutron transport problem where these assumptions can be justified as well, we assume the transport of protons through matter is accurately described by the linear Boltzmann equation.

3.1.2 Physical Interpretation of the Operators

The linear Boltzmann equation contains seven independent variables: one in time, three in the position $\vec{r}$, one in the kinetic energy E and two in the direction of movement $\hat{\Omega}$. In proton therapy planning, we are only interested in the steady state solution of the problem, leaving us with six independent variables described by the steady state linear Boltzmann equation:

$$\hat{\Omega} \cdot \nabla\varphi(\vec{r}, E, \hat{\Omega}) + \sigma_t\varphi(\vec{r}, E, \hat{\Omega}) = \int_{4\pi}\int_0^\infty dE'\sigma_s(\vec{r}, E' \to E, \hat{\Omega}' \to \hat{\Omega})\varphi(\vec{r}, E', \hat{\Omega}')d\hat{\Omega}' \quad (3.1)$$

Here we introduce the symbols and the physical interpretation of the operators in the equation. For a complete derivation of this equation, the reader is referred to the work of Duderstadt and Hamilton [9].

The quantity considered in this equation is the angular flux $\varphi(\vec{r}, E, \hat{\Omega})$. It may be interpreted as the particle density with kinetic energy E, moving in direction $\hat{\Omega}$ through the surface of the unit sphere at position $\vec{r}$. The first term on the left hand side is the streaming term, which describes the free movement of the particles through the problem domain. The second term is the total removal term, describing all the interactions of the particles, causing the particles to scatter to an energy different from E and a direction of travel different from $\hat{\Omega}$, or get absorbed by the target nucleus. The rate of this interaction is proportional to the total cross section σ_t and to the angular flux $\varphi(\vec{r}, E, \hat{\Omega})$. The term on the right hand side is the Boltzmann scatter operator. This operator describes the particles scattered from all the energies E' and direction of movement $\hat{\Omega}'$ to the energy and direction of movement which is being considered; E and $\hat{\Omega}$. In this operator, no distinction is made between the types of scatter interactions.

3.1.3 Separation of the Scatter Interactions

In the previous chapter, we have distinguished between three types of scatter interactions: catastrophic scatter, inelastic scatter with atomic electrons and elastic scatter with atomic nuclei. It is convenient to separate the Boltzmann scatter operator into three terms, each representing one of these three scatter interactions:

$$\begin{aligned}\hat{\Omega} \cdot \nabla\varphi(\vec{r}, E, \hat{\Omega}) = &\int_{4\pi}\int_E^\infty \sigma_C(\vec{r}, E' \to E, \hat{\Omega}' \to \hat{\Omega})\varphi(\vec{r}, E', \hat{\Omega}')d\hat{\Omega}'dE' - \sigma_{C,s}\varphi(\vec{r}, E, \hat{\Omega}) \\ &+ \int_{4\pi} \sigma_e(\vec{r}, E, \hat{\Omega}' \to \hat{\Omega})\varphi(\vec{r}, E, \hat{\Omega}')d\hat{\Omega}' - \sigma_{e,s}\varphi(\vec{r}, E, \hat{\Omega}) \\ &+ \int_0^\infty \sigma_{in}(\vec{r}, E + Q \to E, \hat{\Omega})\varphi(\vec{r}, E + Q, \hat{\Omega})dQ - \sigma_{in,s}\varphi(\vec{r}, E, \hat{\Omega}),\end{aligned} \quad (3.2)$$

where σ_C is the catastrophic scatter cross section, σ_e is the elastic scatter cross section, and σ_{in} is the inelastic scatter cross section, defined in the previous chapter. In this equation the total scattering cross section is replaced by the total cross section of the

three interaction processes: $\sigma_t = \sigma_{C,s} + \sigma_{e,s} + \sigma_{in,s}$. The first term on the right hand side of the equation represents all the particles having energy E and moving in direction $\hat{\Omega}$ after a catastrophic scatter interaction with a nucleus. Notice that the integral in this term is from $E' = E$ instead of $E' = 0$. This is because we assume that no upscatter interactions take place (the protons only lose energy in this interaction process). The third term on the right hand side represent the particles which have a direction of movement $\hat{\Omega}'$ before a elastic scatter interaction with a nucleus, and a direction of movement $\hat{\Omega}$ after the interaction. Since the energy loss in this interaction process is neglected, the particles have energy E before and after the interaction. The rate of this interaction is proportional to the elastic scatter cross section σ_e. The fourth term on the right hand side of 3.2 represents all the particles which have direction of movement $\hat{\Omega}$ before a elastic scatter interaction, and are scattered to a direction of movement different from $\hat{\Omega}$. The fifth term on the right hand side of equation 3.2 represents the particles with an energy different from E before and energy E after a inelastic scatter interaction with the atomic electrons. The angular deflection of this interaction process is neglected. Hence, the particles have a direction of movement $\hat{\Omega}$ before and after the interaction. The final term of equation 3.2 represents the particles having energy E before a inelastic scatter interaction with the atomic electrons and an energy different from E after the interaction. A solution of 3.2 will give us all the information we need on the proton field, including the creation of secondary particles. Trying to solve this equation directly with a deterministic code, however, gives rise to a practical problem as we will see in the next section.

3.1.4 Introduction of Flux Definitions

The quantity of interest in the Boltzmann equation is the angular flux $\varphi(\vec{r}, E, \hat{\Omega})$. Before we continue, we need to introduce three quantities which will be used in the following sections: the angular depending differential flux $\varphi(\vec{r}, \hat{\Omega})$, the energy spectrum or the energy depending differential flux $\varphi(\vec{r}, E)$ and the scalar flux $\phi(\vec{r})$.

The angular depending differential flux can be interpreted as the particle density at position $\vec{r}$ moving in direction $\hat{\Omega}$ and can be expressed in terms of the angular flux as:

$$\varphi(\vec{r}, \hat{\Omega}) = \int_0^\infty \varphi(\vec{r}, E, \hat{\Omega}) dE. \tag{3.3}$$

The energy depending differential flux can be interpreted as the particle density with at position $\vec{r}$ with energy E and can be expressed in terms of the angular flux as in:

$$\varphi(\vec{r}, E) = \int_{4\pi} \varphi(\vec{r}, E, \hat{\Omega}) d\hat{\Omega}. \tag{3.4}$$

The scalar flux can be interpreted as the total number of particles moving through the surface of the unit sphere at position $\vec{r}$. The scalar flux can be expressed in terms of a differential flux or in terms of the angular flux as in:

$$\phi(\vec{r}) = \int_0^\infty \int_{4\pi} \varphi(\vec{r}, E, \hat{\Omega}) d\hat{\Omega} dE = \int_{4\pi} \varphi(\vec{r}, \hat{\Omega}) d\hat{\Omega} = \int_0^\infty \varphi(\vec{r}, E) dE. \tag{3.5}$$

3.2 The Fokker-Planck Approximation

Significant problems arise when treating charged particle transport with conventional means in deterministic methods, due to the nearly singular shape of the differential cross sections, see figures 2.4 and 2.5. In deterministic methods, it is common practice to expand the differential cross section in Legendre polynomials (up to P_{10} is standard, due to computation time and storage considerations). Smooth functions can be approximated well with a relatively low order expansion, see figure 3.1(a). In this figure, a smooth example scoss section is expanded, and well approximated, by a P_{10} Legendre expansion. However,

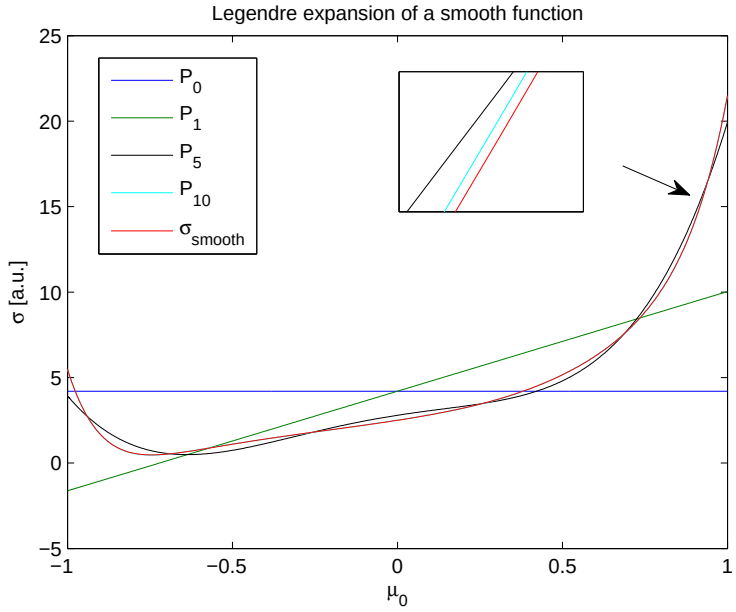

(a) *A smooth arbitrary cross section expanded in Legendre polynomials.*

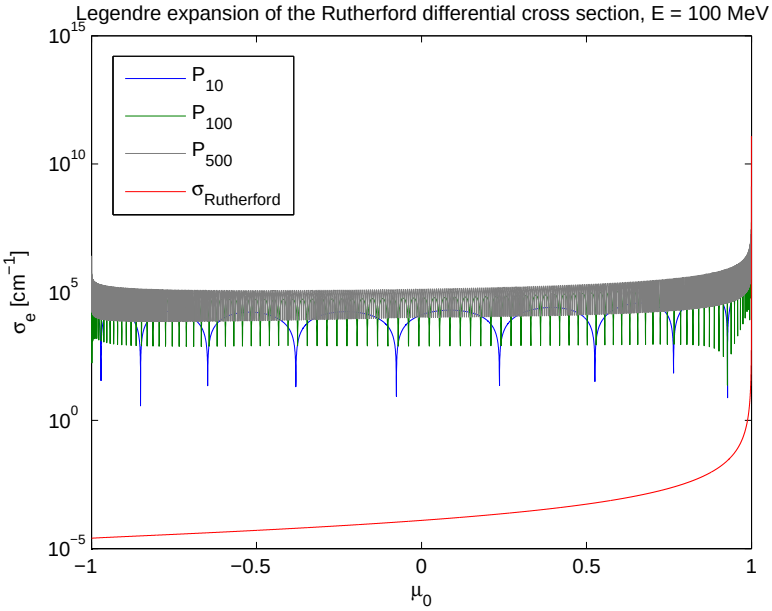

(b) *Nearly singular screened Rutherford differential cross section of 100 MeV protons incident on water expanded in Legendre polynomials. The absolute value of the expanded cross sections are shown, which explains the shape of these expansions.*

Figure 3.1: *The nearly singular differential cross sections of charged particles expanded in Legendre functions.*

the differential cross sections in charged particles interaction are nearly singular, see figure 3.1(b). In this figure, the differential cross section of protons with an energy of 100 MeV incident on water is shown. This cross section increases near $\mu_0 = 1$ with approximately 15 orders of magnitude. A very high order of expansion is needed to accurately represent such a cross section. In figure 3.1 this cross section is expanded up to a P_{500} Legendre series, and even with this high order expansion, the cross section is still not represented well. Also, to describe these large number of small angle scatters and small energy transfers, an unrealistic fine angular and energy grid are necessary. Since it is important in the modeling process that these cross sections are accurately represented, and since the computation expense and storage space increases with the order of the Legendre expansion and grid size, it is inconvenient to treat these cross sections by conventional means.

The Fokker-Planck approximation offers a solution to these problems. In this approach, the small angle scatter in the elastic scatter interaction process with the atomic nuclei is approximated by the continuous scatter operator, and the small energy losses in the inelastic scatter interaction process with the atomic electrons is approximated by the continuous slowing down and energy straggling operators. Due to the formulation of this approximation, there is no further need to describe the near singular differential cross section with Legendre polynomials, resulting in reduced computation time.

In the following section, a short derivation of these Fokker-Planck operators is presented, followed by a brief discussion on the physical interpretation and the accuracy of these operators.

3.2.1 Continuous Scatter Operator

In this section, we demonstrate how to derive the continuous scatter operator by applying the Fokker-Planck approximation to the Boltzmann scatter operator $L_{B,e}$ of the elastic scatter interaction process of charged particles with atomic nuclei. This derivation follows the work of Leakeas and Larsen [24]. The Boltzmann operator of this process for particles with an arbitrary energy at an arbitrary position is given by:

$$L_{B,e}\varphi(\hat{\Omega}) = \int_{4\pi} \sigma_e(\hat{\Omega}' \to \hat{\Omega})\varphi(\hat{\Omega}')d\hat{\Omega}' - \sigma_{e,s}\varphi(\hat{\Omega}). \tag{3.6}$$

The first step is to expand the elastic differential cross section into spherical harmonic functions:

$$\sigma_e(\mu_0) = \sum_{l=0}^{\infty} \sigma_{e,l} \sum_{m=-l}^{l} Y_l^m(\hat{\Omega}) Y_l^{*m}(\hat{\Omega}') \tag{3.7}$$

with the Legendre moments $\sigma_{e,l}$ given by:

$$\sigma_{e,l} = 2\pi \int_{-1}^{1} \sigma_e(\mu_0) P_l(\mu_0) d\mu_0. \tag{3.8}$$

Notice that we have replaced $\hat{\Omega}' \to \hat{\Omega}$ by the cosine scatter angle μ_0. We could do this since we assume that only isotropic materials are considered in proton therapy. In isotropic materials the scattering angle, and also the cosine of the scatter angle $\mu_0 = \hat{\Omega}' \cdot \hat{\Omega}$, is independent of the incoming direction of movement $\hat{\Omega}'$ of the incident proton. The second step is to expand the angular flux in these same spherical harmonic functions:

$$\varphi(\hat{\Omega}) = \sum_{l=0}^{\infty} \sum_{m=-l}^{l} \phi_{lm} Y_l^m(\hat{\Omega}) \tag{3.9}$$

where,

$$\phi_{lm} = \int_{4\pi} \varphi(\hat{\Omega}) Y_l^m(\hat{\Omega}) d\hat{\Omega}. \tag{3.10}$$

With these expressions and using the orthogonality property of the spherical harmonic functions, the Boltzmann scatter operator becomes:

$$L_{B,e}\varphi(\hat{\Omega}) = \sum_{l=0}^{\infty}\sigma_{e,l}\sum_{m=-l}^{l}\phi_{lm}Y_l^m(\hat{\Omega}) - \sigma_{e,s}\sum_{l=0}^{\infty}\sum_{m=-l}^{l}\phi_{lm}Y_l^m(\hat{\Omega}). \tag{3.11}$$

Since the differential cross section is peaked near $\mu_0 = 1$ we can approximate the Legendre polynomials in equation 3.8 by a Taylor series about $\mu_0 = 1$.

$$\begin{aligned}\sigma_{e,l} &\approx 2\pi\int_{-1}^{1}\sigma_e(\mu_0)\left(P_l(1) + P_l'(1)(\mu_0-1) + \mathcal{O}(\mu_0-1)^2\right)d\mu_0 \\ &= \sigma_{e,s} - \sigma_{tr}P_l'(1) + \mathcal{O}\left(\sigma_{e,s}\overline{(\mu_0-1)^2}\right)\end{aligned} \tag{3.12}$$

with,

$$\sigma_{tr} = 2\pi\int_{-1}^{1}(1-\mu_0)\sigma_e(\mu_0)d\mu_0. \tag{3.13}$$

Legendre polynomials have the following basic property:

$$P_l'(1) = \frac{l(l+1)}{2} \tag{3.14}$$

Plugging this back into 3.12 gives:

$$\sigma_{e,l} \approx \sigma_{e,s} - \sigma_{tr}\frac{l(l+1)}{2} + \mathcal{O}\left(\sigma_{e,s}\overline{(\mu_0-1)^2}\right). \tag{3.15}$$

We have used Legendre and Taylor expansions to rewrite the Boltzmann scatter term. In the next step, we assume the differential cross section is forward peaked enough to express it with only a first order Taylor expansion. With this approximation, the expression of the Boltzmann scatter operator becomes:

$$L_{B,e}\varphi(\hat{\Omega}) \approx \frac{\sigma_{tr}}{2}\sum_{l=0}^{\infty}-l(l+1)\sum_{m=-l}^{l}\phi_{lm}Y_l^m(\hat{\Omega}) \tag{3.16}$$

The spherical harmonics functions are the eigenvalues of the angular part of the Laplace operator:

$$\nabla^2_{\hat{\Omega}}Y_l^m = -l(l+1)Y_l^m. \tag{3.17}$$

Now, we use all of the above to obtain the final expression for the first order Taylor approximation of the Boltzmann scatter operator:

$$\begin{aligned}L_{B,e}\varphi(\hat{\Omega}) &\approx \frac{\sigma_{tr}}{2}\sum_{l=0}^{\infty}\sum_{m=-l}^{l}\phi_{lm}\nabla^2_{\hat{\Omega}}Y_l^m(\hat{\Omega}) = \frac{\sigma_{tr}}{2}\nabla^2_{\hat{\Omega}}\left(\sum_{l=0}^{\infty}\sum_{m=-l}^{l}\phi_{lm}Y_l^m(\hat{\Omega})\right) = \frac{\sigma_{tr}}{2}\nabla^2_{\hat{\Omega}}\varphi(\hat{\Omega}) \\ &= \frac{\sigma_{tr}}{2}\left[\frac{\partial}{\partial\mu}(1-\mu^2)\frac{\partial\varphi(\hat{\Omega})}{\partial\mu} + \frac{1}{1-\mu^2}\frac{\partial^2\varphi(\hat{\Omega})}{\partial\phi^2}\right].\end{aligned} \tag{3.18}$$

Here, we have transformed an integro-differential operator into a differential operator which is much easier to solve. This Fokker-Planck operator is the continuous scatter operator. Physically, this operator represents the diffusion of flux over the unit sphere; in a proton pencil beam, the protons are introduced in the problem domain all having the same direction of movement. This is represented by an infinitely small dot on the surface of

the unit sphere. As the protons penetrate through the material, the direction of movement deviates from their original trajectory. This process is represented by the diffusion of this dot over the surface of the unit sphere. The rate in which this dot diffuses over the unit sphere is proportional to the first moment of the elastic scatter cross section $\sigma_{tr}(E)$, which is called the momentum transfer cross section, or the transport cross section. Physically, it represents the average angular deviation of the incident particle per unit distance traveled. So instead of modeling the large number of small angle scatters, with this operator we only model the average angular deflection of the protons per unit distance traveled. The momentum transfer cross section can be evaluated by substituting the screened Rutherford cross section for σ_e from the previous chapter, equation 2.15:

$$\sigma_{tr}(E) = 2\pi \int_{-1}^{1} (1-\mu_0)\sigma_e(\mu_0)d\mu_0$$
$$= 2\pi \int_{-1}^{1} (1-\mu_0) \frac{\left(1+\frac{2\mu_0}{A_t}+\frac{1}{A_t}^2\right)^{\frac{3}{2}}}{1+\frac{\mu_0}{A_t}} \left(\frac{Z_t e^2}{4\pi\epsilon_0 m_0 v_0^2}\right)^2 \frac{1}{(1-\mu_0+2\eta)^2} d\mu_0. \tag{3.19}$$

Unfortunately, this integral is very difficult to solve analytically, and therefore one should use numerical integration. For heavy nuclei, the scattering angle of the proton measured in the center of mass frame is approximately equal to the scattering angle measured in the laboratory frame: $\vartheta \approx \Theta$. Using this approximation, the transport equation can be evaluated analytically:

$$\sigma_{tr}(E) = 2\pi \int_{-1}^{1} (1-\mu_0)\sigma_e(\mu_0)d\mu_0$$
$$\approx 2\pi \int_{-1}^{1} (1-\mu_0) \left(\frac{Z_t e^2}{4\pi\epsilon_0 m_p v_0^2}\right)^2 \frac{1}{(1-\mu_0+2\eta)^2} d\mu_0 = 2\pi \left(\frac{Z_t e^2}{4\pi\epsilon_0 m_p v_0^2}\right)^2 \left(\ln\frac{\eta+1}{\eta} - \frac{1}{\eta+1}\right) \tag{3.20}$$

where we used $m_0 \approx m_p$. In this thesis, this expression is used to evaluate all of the momentum transfer cross sections, including those of the light elements. The error due to this approximation is around 10%, except for hydrogen, for which the error is much larger, see figure 2.3. However, the magnitude of the momentum transfer coefficient for hydrogen turns out to be negligible compared to the momentum transfer cross sections of the other elements. This is demonstrated by comparing the result of equation 3.19 with $Z_t = 1$ and $A_t = 1$ for hydrogen and, for example, $Z_t = 8$ and $A_t = 16$ for oxygen. The total error in using equation 3.20 instead of numerically evaluating the integral in equation 3.19 for evaluating the momentum transfer cross sections of materials considered in proton therapy, is estimated to be approximately 10%. In future work a numerical integration routine should be developed to evaluate the integral in equation 3.19 precisely and efficiently. In this work, the error of 10% is accepted in the value of the moment transfer coefficient, and no distinguishing is made between the scatter angle measured in the laboratory reference frame ϑ and the center-of-mass frame Θ in the rest of this thesis.

In figure 3.2, the value of the momentum transfer cross section is shown for protons incident on water. From this figure we see that this cross section increases significantly in the low energy range. Physically representing the proton starting to deviate strongly from its original trajectory at the end of its range where its energy is relatively small, resulting in a trumpet-like shape of the proton field.

3.2.2 Continuous Slowing Down and Energy Straggling Operators

The Fokker-Planck approximation for the inelastic scatter has an analogous derivation. As little energy is lost in every collision, the differential cross section is peaked near $Q = 0$,

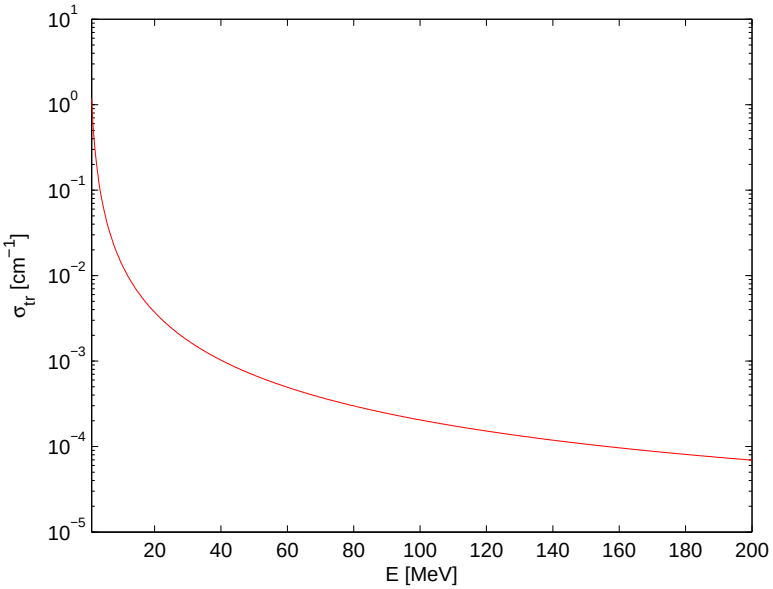

Figure 3.2: *Momentum transfer cross section $\sigma_{tr}(E)$ for protons incident on water.*

allowing it to be approximated with a Taylor series. Including terms up to 2^{nd} order in the Taylor series will lead to:

$$\begin{aligned} L_{B,in}\varphi(E) &= \int_0^\infty \sigma_{in}(E+Q \to E)\varphi(E+Q)dQ - \sigma_{in,s}\varphi(E) \\ &\approx \frac{\partial S(E)\varphi(E)}{\partial E} + \frac{1}{2}\frac{\partial^2 T(E)\varphi(E)}{\partial E^2}. \end{aligned} \tag{3.21}$$

The coefficient $S(E)$ and $T(E)$ are the first and second moment of the inelastic cross section respectively. $S(E)$ is the stopping power and $T(E)$ the energy straggling coefficient. In this section, we elaborate on the physical interpretation of these two Fokker-Planck operators and their corresponding coefficients. A complete derivation of these Fokker-Planck operators can be found in appendix B.

Stopping Power

The first term on the right hand side of equation 3.21 is what we call the continuous slowing down operator. Physically, this operator represents the continuous energy transfer of the incident proton to the atomic electrons. The rate of this energy transfer is given by the first moment of the inelastic cross section

$$S(E) = \int_0^\infty \sigma_{in}(Q)QdQ \tag{3.22}$$

and is called the stopping power. Two types of inelastic scatter interactions with the atomic electrons contribute to the stopping power: the soft scatter interactions and the hard scatter interactions. The contribution to the stopping power of soft scatter is obtained by integrating the soft scatter differential cross section in equation 2.20 from the minimum possible energy transfer to the bound electron Q_{min}, up to some maximum value H, for which the collision can still be considered soft. The minimum possible energy transfer Q_{min} is in the order of the geometric mean of all the ionization and excitation potentials I of the target atom. This value cannot be determined analytically, except for hydrogen. Therefore, this constant is determined empirically for each element. In this thesis, the

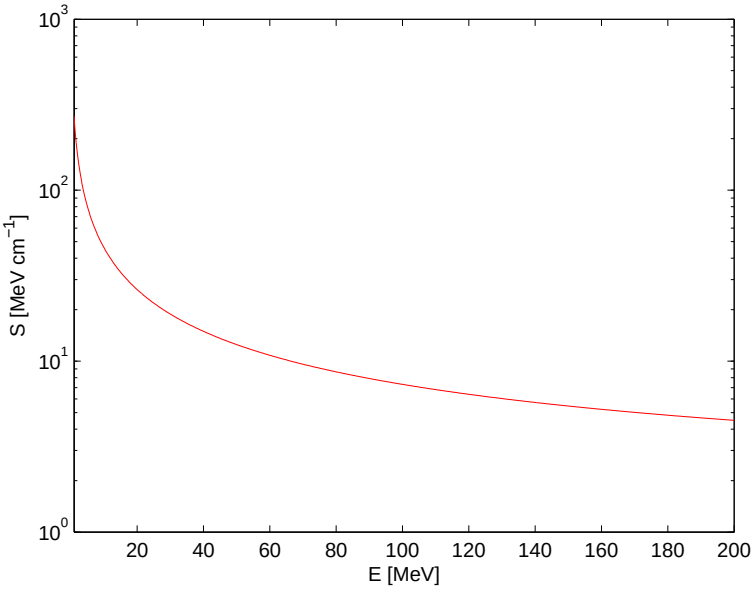

Figure 3.3: *Stopping power $S(E)$ of protons incident on water.*

values of I in eV as proposed by Turner[41] are used.

$$S_{soft}(E) = \int_{Q_{min}}^{H} Q\sigma_{in,soft}(Q)dQ = \int_{Q_{min}}^{H} Q\frac{2\pi Z_i^2 e^4}{(4\pi\epsilon_0)^2 m_e v_0^2}\frac{1}{Q}\frac{df_n}{dE_n}dQ$$
$$= \frac{2\pi e^4}{(4\pi\epsilon_0)^2 m_0 v_0^2}\ln\frac{2m_0 v_0^2 H}{I^2} \tag{3.23}$$

with,

$$I = \begin{cases} 19 & \text{for} \quad Z_t = 1 \\ 11.2 + 11.7Z_t & \text{for} \quad 2 \leq Z_t \leq 13 \\ 52.8 + 8.71Z_t & \text{for} \quad Z_t > 13. \end{cases} \tag{3.24}$$

The contribution of the hard scatter collisions is obtained by integrating the hard scatter differential cross section from equation 2.19 from the value from which the collision can be considered hard H to the maximum energy transferred in one such collision Q_{max}.

$$S_{hard}(E) = \int_{H}^{Q_{max}} Q\sigma_{in,hard}(Q)dQ = \int_{H}^{Q_{max}} Q\frac{2\pi Z_i^2 Z_t^2 e^4}{(4\pi\epsilon_0)^2 m_e v_0^2}\frac{1}{Q^2}dQ$$
$$= \frac{2\pi e^4}{(4\pi\epsilon_0)^2 m_0 v_0^2}\ln\frac{Q_{max}}{H} \tag{3.25}$$

The largest amount of energy transferred in one collision can be derived from the conservation law for energy and momentum[11],

$$Q_{max} = E_k\left[\frac{1 + \left(\frac{2m_p c^2}{E_k}\right)}{1 + (m_p + m_e)^2\left(\frac{c^2}{2m_e E_k}\right)}\right] \tag{3.26}$$

where E_k is the kinetic energy of the incident proton. In the energy range considered in proton therapy, this relationship reduces to the following:

$$Q_{max} = 2m_e v_0^2. \tag{3.27}$$

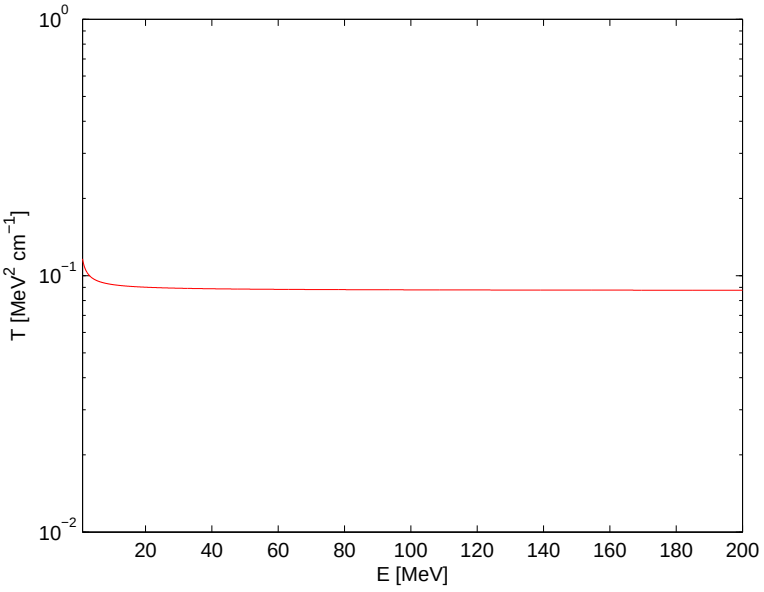

Figure 3.4: *The energy straggling coefficient $T(E)$ for protons incident on water.*

Using this result, and adding the contribution of the soft and the hard scatter, we obtain the total stopping power for protons:

$$S(E) = S_{soft} + S_{hard} = \frac{4\pi e^4}{(4\pi\epsilon_0)^2 m_e v_0^2} \ln \frac{2m_e v_0^2}{I^2}. \tag{3.28}$$

This is the stopping power for incident protons per electron. From this result, we see that the value of H is arbitrary, since it cancels out when the soft- and hard scatter contributions are added.

From figure 3.3 we recognize the nature of energy deposition of the incident protons: the incident protons transfers relatively little energy to their surroundings when their energy is high. When the protons reach the end of their ranges through the material, their energy is relatively low, and the magnitude of the stopping power increases significantly. As a consequence, the protons deposit their remaining energy very locally at the end of their range, which results in the Bragg peak.

Energy Straggling Coefficient

The second term on the right hand side of equation 3.21 is the energy straggling operator. Physically, this operator represents the stochastic nature of the interaction process between the incident proton and its surrounding medium; not every proton has the same amount of energy after passing a fixed amount through a material, and not every proton has the same range through the material. In modeling, this operator acts as a diffusion operator in the energy domain, with the energy straggling coefficient $T(E)$, the second moment of the inelastic differential cross section, as a diffusion coefficient. Williams [43] included quantum mechanical effects of the electron binding in his derivation of $T(E)$. The final result is

$$T(E) = 4\pi e^4 \left(1 + \frac{kI}{m_0 v_0^2} \ln \frac{2m_0 v_0^2}{I}\right) \tag{3.29}$$

where $k = \frac{4}{3}$ is assumed to obtain approximate results for any atom. The energy straggling coefficient is shown in figure 3.4 for protons incident on water. From this figure we see that the energy straggling coefficient does not increase in magnitude as much in the low energy range as the two other Fokker-Planck coefficients.

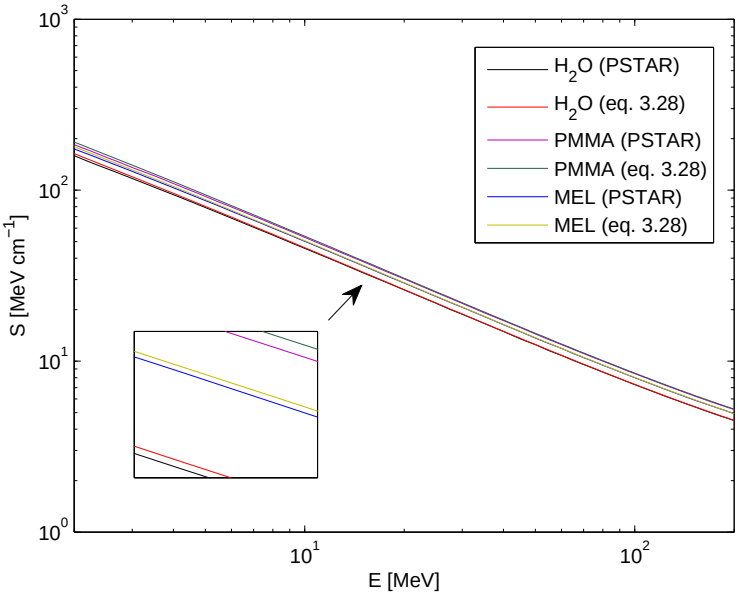

Figure 3.5: *Stopping power evaluated with equation 3.28 compared to literature values of PSTAR*[2].

3.2.3 Validation of the Coefficients

So far, we have introduced three coefficients based on models derived in the previous sections: the stopping power $S(E)$, the momentum transfer coefficient $\sigma_{tr}(E)$, and the energy straggling coefficient $T(E)$. In order to validate these models, the outcomes of these models are compared to literature values.

To compare momentum transfer coefficients and the energy straggling coefficients, we used the work of Kelsey[22]. For energy straggling coefficients, we have obtained similar result to those found in his work. Kelsey used two methods to evaluate the momentum transfer cross sections: the screened Rutherford model and a computer code called MCNPX. Our results are similar to screened Rutherford results found in his work. The results of the MCNPX model, however, differ approximately by a factor of two. This uncertainty in the momentum transfer coefficient is much larger than the 10% error which we allowed for, in our model in the previous chapter.

Values of stopping power for protons on various materials are well documented in literature. Both experimental data and models are available to compare results with. In this work, we compare our data with the data from PSTAR[2]. PSTAR generates stopping powers for protons as tabulated in ICRU report 49[19]. In figure 3.5, the results are shown of stopping power value evaluated by PSTAR for three materials: PMMA, water and MEL (muscle equivalent liquid). Also in this figure are the stopping power values generated by our model in equation 3.28. Although the results are similar, the values of the stopping power generated by our model is a small fraction larger compared to the stopping power evaluated by PSTAR. Two effects are not included in our model which may be responsible for the small difference: the electronic shell correction effect, and the density effect.

The density effect occurs in dense media, where the dielectric polarization of the material alters the particle's field, and thus 'screening' the field from distance atoms, which decreases the interaction between the incident charged particle and the material, resulting in a slightly reduced stopping power. This effect becomes significant for protons with an energy which exceeds their rest mast. For a proton, the rest mass is 938 MeV, which is far beyond the energy range considered in proton therapy.

The second effect, the shell correction effect, is important in the energy range consid-

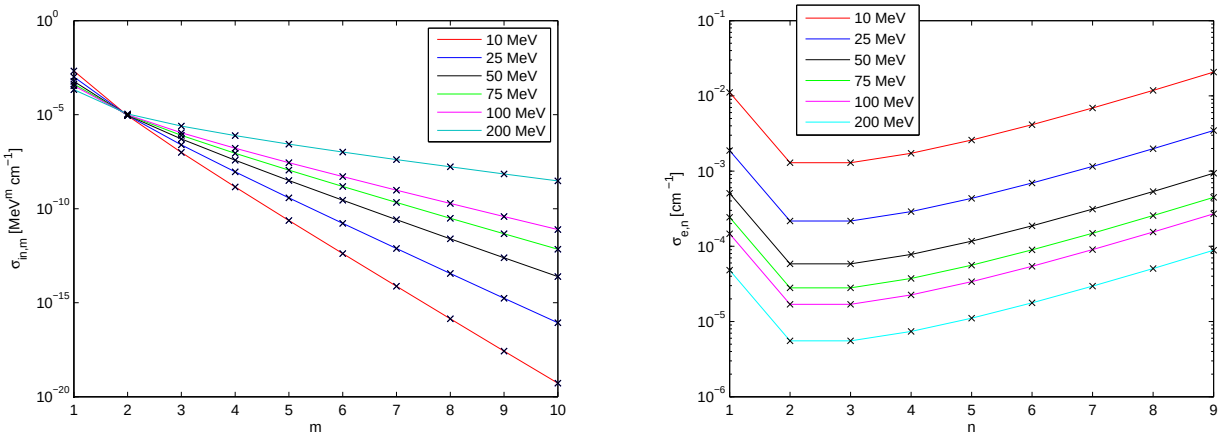

Figure 3.6: *Left: moments of the inelastic Rutherford cross section for protons incident on water. Right: moments for the elastic Rutherford cross section for protons incident on water.*

ered in proton therapy. This effect corrects for the assumption that the incident particles velocity is far greater than the velocity of the atomic bound electron in the energy range of 1 - 100 MeV in the case of protons [47]. In this energy range, the electron's orbital bonding needs to be considered in the collision between the electron and the incident proton. These shell corrections have been calculated and documented in literature using various approximations. The two most common approaches to calculate non-relativistic shell correction are the hydrogenic wave functions and the local density approximation. In future work one of these approaches should be included in the model for the stopping power to improve results. Or, as an alternative, available tabulated data of stopping power values can be used from, for example, PSTAR.

3.3 Validation of the Fokker-Planck Approximation

Due to the forward peaked nature of the interaction process, the scatter cross sections of the inelastic scatter with atomic electrons and the elastic scatter with atomic nuclei can be approximated by a finite Taylor series, giving rise to the Fokker-Planck operators. But since this approximation uses only the first and second order Taylor expansions around $Q = 0$ and $\mu_0 = 1$ respectively, it discards any large angle scattering and large energy transfers. So, the differential scattering cross section has to be sufficiently forward peaked, for this approximation to hold. If this condition is met, we expect the higher moments of the differential cross sections

$$\sigma_{e,n} = \int_{-1}^{1} (1 - \mu_0)^n \sigma_e(\mu_0) d\mu_0 \tag{3.30}$$

and

$$\sigma_{in,m} = \int_{Q_{min}}^{Q_{max}} Q^m \sigma_{in}(Q) dQ \tag{3.31}$$

to be vanishing small for $n > 1$ and $m > 2$.

Figures 3.6 show the magnitude of various moments for different energies for the inelastic (left) and the elastic scatter (right) processes. Similar results were found by Smith [40]. And indeed the higher moments for the inelastic scatter for all energies in the range considered seem to vanish. For elastic scatter, however, this does not seem to be the case. Here, the second moment is an order of magnitude smaller than the first, but the magnitude of the higher moments starts to increase significantly. On the basis of this analysis, the

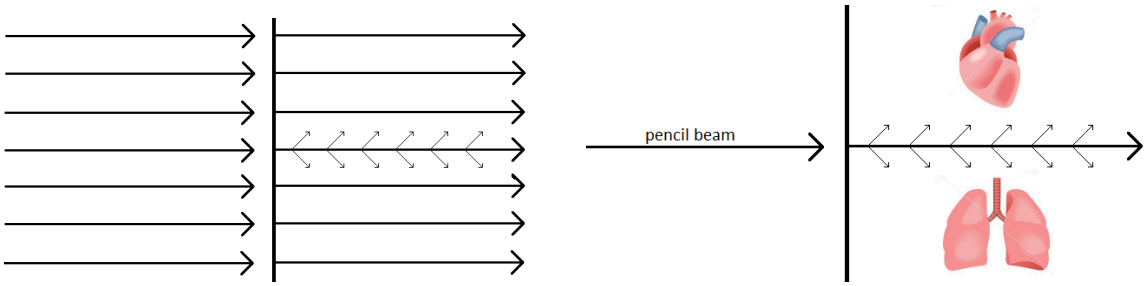

Figure 3.7: *Left: the 1D pencil beam problem can be visualized in the 3D geometry as the uniform radiation of an infinite large slab. Large angle scatter can be ignored in this case. Right: 3D pencil beam problem. Large angle scatter can not be ignored in this case, since in this process energy is pushed to the surrounding tissue, where critical organs may be present.*

validity of the Fokker-Planck approximation for elastic scatter is questionable. An analysis by Larsen and Börgers confirms this suspicion, showing the Fokker-Planck approximation for elastic scatter to lie on the verge of validity [23].

A second argument to doubt the validity of the Fokker Planck approximation for elastic scatter is the fact that large angle scatter can (and will) transfer energy to surrounding tissue where critical organs may be present, see figure 3.7 (right). It is desirable to predict the amount of this energy, and since the Fokker-Planck approximation ignores all large angle scatter, it is not a complete description of the problem, at least not by itself.

3.3.1 The Boltzmann-Fokker-Planck Approximation

The objective of a hybrid method is to isolate the problematic part of the differential cross section and to treat it by other means. The large angle scatter is the problematic part for the Fokker-Planck (continuous scatter) operator, and the small angle scatter is the problematic part for the conventional Boltzmann scatter operator. The optimal hybrid approximation proposed is the Boltzmann-Fokker-Planck approximation [40]. Here, the singular part, which describes the small angle scatter, is separated from the smooth part, which describes the large angle scatter. The singular part is treated with the Fokker-Planck continuous scatter operator; the remaining smooth part is treated by the conventional Boltzmann scatter operator. This hybrid method allows exact treatment of the large angle scatter, with all the benefits of the Fokker-Planck approximation.

$$L_{B,e}\varphi(\hat{\Omega}) \approx \frac{\sigma_{tr}}{2}\left[\frac{\partial}{\partial\mu}(1-\mu^2)\frac{\partial\varphi(\hat{\Omega})}{\partial\mu} + \frac{1}{1-\mu^2}\frac{\partial^2\varphi(\hat{\Omega})}{\partial\phi^2}\right] + \int_{-1}^{1}\sigma_{e,sm}(\hat{\Omega}'\to\hat{\Omega})\varphi(\hat{\Omega}')d\hat{\Omega}' - \sigma_{e,sm,s}\varphi(\hat{\Omega}) \tag{3.32}$$

with

$$\sigma_{tr} = 2\pi\int_{-1}^{1}(1-\mu_0)\sigma_{e,si}(\mu_0)d\mu_0. \tag{3.33}$$

Here, $\sigma_{e,sm}$ and $\sigma_{e,si}$ are the smooth part and the singular part respectively, see figure 3.8 (left).

Again, we want the higher moments in the Fokker-Planck equation to be vanishing small for $n > 1$. In order to investigate these higher moments, we decompose the elastic differential equation in a smooth part from $\mu_0 = -1$ to $\mu_0 = \mu^*$ and a singular part from $\mu_0 = \mu^*$ to $\mu_0 = 1$. In deterministic methods, however, decomposing the differential cross section as described here, is inconvenient since the smooth part has a discontinuity at μ^* which makes this part difficult to expand in a Legendre series. For the analysis done here,

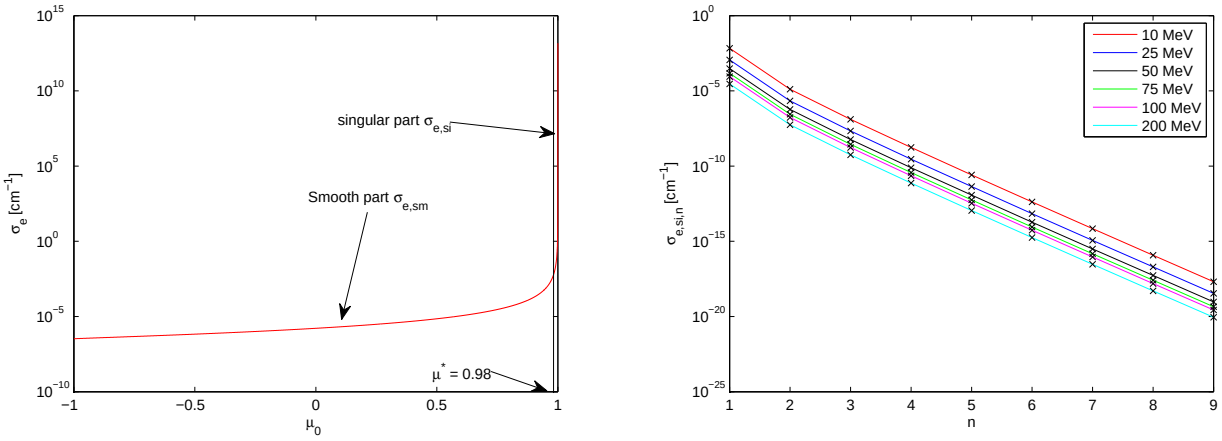

Figure 3.8: *Left: decomposition of the differential cross section into a smooth and a singular part. Right: moments of the singular part of the elastic cross section for protons incident on water for different energies.* $\mu^* = 0.98$ *was set here, but different choices for* μ^* *near* $\mu^* = 0.98$ *gave similar results.*

however, with the object of investigating the higher moments, the method of decomposing is arbitrary. For a discussion on a smooth decomposition of the differential cross section, the reader is referred to the work of Smith [40]. With the decomposition method we have used here, we are able to calculate higher moments of the singular part:

$$\sigma_{e,si,n} = \int_{\mu^*}^{1} (1-\mu_0)^n \sigma_e(\mu_0) d\mu_0. \tag{3.34}$$

These higher moments, as shown in figure 3.8 (right), do vanish for $n > 1$, showing the accuracy of the Boltzmann-Fokker-Planck equation. In the decomposition depicted in figure 3.8 (left), we chose $\mu^* = 0.98$ by inspection of figure 2.4. Other values near $\mu^* = 0.98$ gave similar results.

So, in modeling proton therapy in a 3D simulation, one should decompose the elastic differential equation in a smooth and a singular part in order to obtain optimal results. In this thesis, however, we only consider 1D problems (this for simplicity, in future work the obtained equations can be expanded to solve problems in 2D and 3D geometries). In 1D calculations no energy can be transferred to the surrounding tissue. This is demonstrated by visualizing the 1D geometry in three dimensions. In 3D, the 1D problem is the uniform irradiation of an infinite large slab. Since no energy can be pushed outside the beam in this case, and the number of particles which encounter large angle scatter is very small compared to the number of particles in the beam, the energy deposited by these large angle scattered particles can be neglected, see figure 3.7 (left). Only in a 3D geometry energy can be pushed outside the beam where critical organs may be present, see figure 3.7 (right). Since only 1D calculations are performed in this thesis, this decomposition of the elastic scatter cross section is not taken into account in the rest of this work. However, since we still use the Boltzmann scatter operator in the transport equation to describe the catastrophic scatter process, the transport equation is still referred to as the Boltzmann-Fokker-Planck equation in the remainder of this thesis.

3.4 Conclusions

The underlying assumptions of the linear Boltzmann equation can be justified. This equation is assumed to be able to accurately describe proton transport and is used as the basis of the modeling process.

The nearly singular Coulomb scatter cross sections are unpractical to treat with conventional methods in deterministic methods (to expand them in a finite Legendre series). The Fokker-Planck approximation is used to overcome this issue. In this approximation, the small angle scatter and the small energy transfers are described by the Fokker-Planck operators: the continuous scatter operator describes the small angle scatter, the continuous slowing down operator describes the small energy transfers of the incident protons to the atomic electrons, and the energy straggling operator describes the stochastic nature of the energy transfer to the atomic electrons.

The Fokker-Planck coefficients are evaluated with the Rutherford scatter cross sections. The momentum transfer cross section $\sigma_{tr}(E)$ expresses the rate of the continuous scatter process. The stopping power $S(E)$ expresses the rate of the energy transfer to the atomic electrons, and the energy straggling coefficient $T(E)$ expresses variance in the stochastic nature of the energy transfer process. These coefficients were validated by comparison to literature values. Similar results were found for the energy straggling coefficient $T(E)$ in the work of Kelsey[22]. The transport cross sections $\sigma_{tr}(E)$ have a relatively large uncertainty according to the work of Kelsey, values of our work are within this range of uncertainty. The stopping power $S(E)$ is compared to the values of the stopping power from PSTAR[2]. The stopping power evaluated with the Rutherford scatter cross sections results in a slightly overestimated stopping power, compared to PSTAR. This difference is expected to reduce if shell corrections are included in the models.

The investigation of the validity of the Fokker-Planck approximation shows the approximation to ignore all large angle Coulomb scatter. In 1D geometries this large angle can be ignored. In 3D geometries, however, the large angle scatter cannot be ignored and the differential scatter cross sections has to be decomposed where the small angle scatter is described by the Fokker-Planck operator and the large angle scatter by the conventional Boltzmann operator.

4. The S_N Method

The Boltzmann-Fokker-Planck transport equation can be solved analytically only in the simplest of problems. In practice, however, such simple problems do not occur, and the transport equation has to be solved by numerical means. For this purpose, we transform the transport equation into a set of algebraic equations. This is accomplished by discretizing the transport equation in all its independent variables. One of the methods to discretize the angular variable in the transport equation is the S_N method. In the S_N method, or the discrete ordinate method, the direction of travel of the particles is approximated by a finite set of N discrete ordinates $\hat{\Omega}_n$ each with a corresponding weight w_n. The sum of the weights equals 4π, since this is the surface of the unit sphere. With this method, the scalar flux is approximated with a sum over the discrete ordinates, multiplied by their corresponding weights:

$$\phi(\vec{r}) = \int_{4\pi} \varphi(\vec{r}, \hat{\Omega}) d\hat{\Omega} \approx \sum_{n=1}^{N} w_n \varphi_n(\vec{r}). \tag{4.1}$$

In this thesis, the S_N method is used to discretize the 1D transport equation in angle. The 1D transport equation with the S_N approximation is:

$$\mu_n \frac{\partial \varphi_n(x,E)}{\partial x} + \sigma_{C,s}\varphi_n(x,E) = \frac{\partial S(E)\varphi_n(x,E)}{\partial E} + \frac{\partial^2 T(E)\varphi_n(x,E)}{\partial E^2}$$
$$+ \frac{\sigma_{tr}}{2}\left(\frac{\partial}{\partial \mu}\left[\left(1-\mu_n^2\right)\frac{\partial \varphi_n(x,E)}{\partial \mu}\right]\right) + \sum_{n'=1}^{N}\int_0^{\infty} \sigma_C(E' \to E, \hat{\Omega}_{n'} \to \hat{\Omega}_n)\varphi_{n'}(x,E')dE' \tag{4.2}$$

where $\mu_n \equiv \cos(\theta_n)$, the directional cosine of the particles traveling along ordinate $\hat{\Omega}_n$, see figure 4.1. In a one dimensional problem, an ordinate $\hat{\Omega}_n$ is fully specified by the directional cosine μ_n. This 1D direction can be visualized in three dimensions by all the directions having an angle θ_n with the x-axis. These directions form a ring on the unit sphere, see figure 2.1.

The number of ordinates N in the set, together with their corresponding weights and directions, is referred to as the quadrature set. The optimal choice for a quadrature set depends on the problem to be solved. In the next section, we present the quadrature set which is adopted in this thesis. In the following sections, we demonstrate how to discretize the one dimensional transport equation in order to obtain an algebraic set of equations. The discretization is done in three steps: an angular, a spatial and an energy discretization.

4.1 The Quadrature Set

The most common choice for a quadrature set in a one dimensional calculation in reactor physics is the Gauss quadrature set [5]. This quadrature set integrates polynomial of order 2N - 1 exactly, which is useful as it is common practice to expand the differential cross sections in Legendre polynomials. However, in this quadrature set the discrete ordinates are symmetrically located around $\mu = 0$. In a proton therapy problem, the directional cosine of the majority of the protons are close to $\mu = 1$, since the protons are introduced

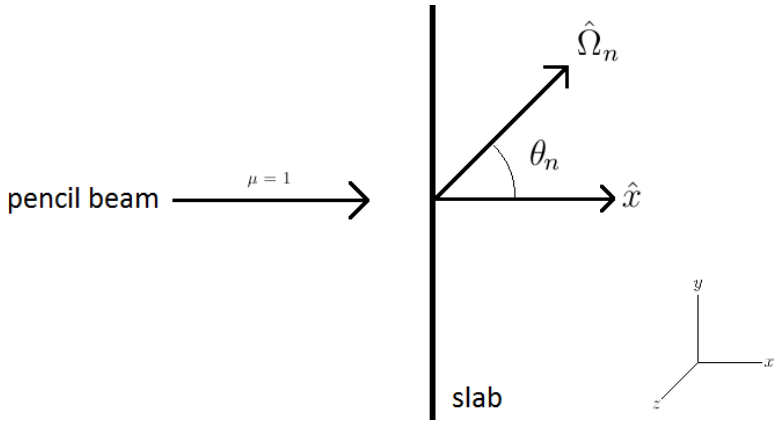

Figure 4.1: *A pencil beam on a slab. The direction of movement of the protons are characterized by the directional cosine* $\mu_n = \cos(\theta_n)$*. The directional cosine of the particles in the pencil beam is* $\mu = 1$*.*

at the boundary with direction cosine $\mu = 1$ and have a strong tendency to go in a straight line and to have small scatter angle interactions. If we would use a Gauss quadrature set in this case, much of the computation expense would go into calculating the angular flux in directions which contribute almost nothing to the solution of the problem. Therefore, we introduce a quadrature set in which the discrete ordinates are densely located near $\mu = 1$ and much less further away from $\mu = 1$. This is accomplished by applying the following recursion relationship on the weights of the ordinates,

$$w_{n-1} = f \cdot w_n \tag{4.3}$$

and placing the discrete ordinates as depicted in figure 4.2, where $w_n^a = \frac{w_n}{2\pi}$.

The values of N and f are chosen such that: (i) the majority of the ordinates are located in the region of interest, $0.98 < \mu < 1$. (ii) the directional cosine μ_N of ordinate $\hat{\Omega}_N$ is close enough to $\mu = 1$ to approximate the pencil beam boundary condition as depicted in figure 4.1. The optimal value for f and N is investigated in chapter 6.

4.2 Angular Discretization

The general procedure in discretizing an independent variable in equation 4.2 is to divide the range of that variable into a number of cells and subsequently integrate the transport equation over the volume of each cell. The result is a set of coupled equations, describing the flux field in the cells in the problem domain. For the angular variable in a 1D problem this means integrating the transport equation over the area surrounding a discrete ordinate. This is done in two steps. First, we evaluate the arbitrary operators L_a in the transport equation which do not explicitly depend on the angular variable μ. Second, we evaluate the integration of the continuous scatter operator L_{CS} over the angular variable. The Boltzmann scatter operator L_B for catastrophic scatter, which depends on both the angular variable μ as the energy variable E, is discretized in section 4.4.1.

Operators that do not depend on the angular variable are left unchanged after integration:

$$\frac{1}{w_n^a} \int_{\mu_{n-\frac{1}{2}}}^{\mu_{n+\frac{1}{2}}} L_a \varphi_n d\mu \approx L_a \varphi_n. \tag{4.4}$$

The continuous scatter operator L_{CS}, on the other hand, does depend on the angular

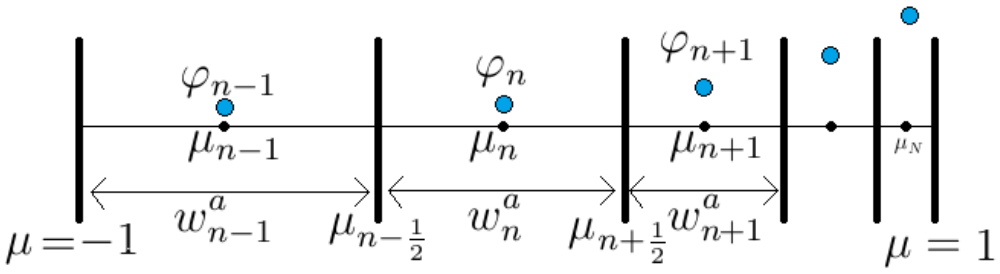

Figure 4.2: *Representation of the variables which characterize the quadrature set. μ_n is the directional cosine, w^a_n the weight and φ_n the flux value of the discrete ordinate $\hat{\Omega}_n$.*

variable μ. Integration of this operator results in:

$$\frac{1}{w^a_n}\int_{\mu_{n-\frac{1}{2}}}^{\mu_{n+\frac{1}{2}}} L_{CS}\varphi_n d\mu = \frac{1}{w^a_n}\int_{\mu_{n-\frac{1}{2}}}^{\mu_{n+\frac{1}{2}}} \frac{\sigma_{tr}}{2}\left(\frac{\partial}{\partial\mu}\left[\left(1-\mu_n^2\right)\frac{\partial\varphi_n}{\partial\mu}\right]\right)d\mu$$

$$= \frac{1}{w^a_n}\left[\frac{\sigma_{tr}}{2}\left(1-\mu_n^2\right)\frac{\partial\varphi_n}{\partial\mu}\bigg|_{\mu_{n-\frac{1}{2}}}^{\mu_{n+\frac{1}{2}}} = \frac{1}{w^a_n}\frac{\sigma_{tr}}{2}\left[\beta_{n+\frac{1}{2}}\left.\frac{\partial\varphi_n}{\partial\mu}\right|_{n+\frac{1}{2}} - \beta_{n-\frac{1}{2}}\left.\frac{\partial\varphi_n}{\partial\mu}\right|_{n-\frac{1}{2}}\right]\right. \tag{4.5}$$

with,

$$\begin{aligned}\beta_{n+\frac{1}{2}} &= \left(1-\mu^2_{n+\frac{1}{2}}\right)\\ \beta_{n-\frac{1}{2}} &= \left(1-\mu^2_{n-\frac{1}{2}}\right).\end{aligned} \tag{4.6}$$

The values of the angular derivatives on the cell faces are approximated by a finite difference scheme. In this scheme, the derivatives are approximated by the finite difference between the flux in the control volume and the flux in the neighbor control volume.

$$\left.\frac{\partial\varphi_n}{\partial\mu}\right|_{n+\frac{1}{2}} \approx \frac{\varphi_{n+1}-\varphi_n}{\mu_{n+1}-\mu_n} \tag{4.7}$$

Note that, due to symmetry, the derivatives of the angular flux on $\mu = 1$ and $\mu = -1$ are equal to zero. This corresponds with the derivatives at $\mu_{N+\frac{1}{2}}$ and $\mu_{\frac{1}{2}}$ respectively.

Discretization of the continuous scatter operator leaves us with an expression for the discrete ordinate flux φ_n, which depends on both the neighboring discrete ordinate fluxes φ_{n-1} and φ_{n+1}. As we will encounter in chapter 5, this dependency on the flux in both neighbor ordinates will introduce the necessity to iterate the equations to obtain a solution which significantly increases computation time.

4.2.1 Advanced Scheme

Since the spherical harmonic functions are eigenfunctions of the continuous scatter operator, it can be demonstrated that [31]

$$L_{CS}f_{iso} = 0 \tag{4.8}$$

$$\int_{4\pi} L_{CS}\varphi d\hat{\Omega} = 0 \tag{4.9}$$

and

$$\int_{4\pi} \vec{\Omega} L_{CS}\varphi d\Omega = -\sigma_{tr}\vec{J} \tag{4.10}$$

where f_{iso} is an arbitrary isotropic function and $\vec{J}$ is the particle current. The first property in equation 4.8 shows that there is no angular diffusion if the flux is already

homogeneously distributed over the unit sphere. The second property, in equation 4.9, tells us that no particles are created or removed by the continuous scatter operator. The third property tells us what current is created in direction $\vec{\Omega}$ due to the Fokker-Planck operator. In transport calculations, it is highly desirable to preserve these properties. Failure to preserve these properties can lead to nonphysical results or to degraded accuracy. The 'standard' scheme presented so far does preserve the properties 4.8 and 4.9 but fails to preserve property 4.10. Morel proposed an improved scheme[31], which uses the following recursion relationship for β.

$$\beta_{n+\frac{1}{2}} = \beta_{n-\frac{1}{2}} - 2\mu_n w_n^a \text{ where } \beta_{\frac{1}{2}} = 0 \tag{4.11}$$

This scheme preserves 4.10 as well as 4.8 and 4.9, and is therefore adopted in this thesis.

In the previous section, we defined the quadrature set adopted in this thesis. In this set, we require the ordinate $\hat{\Omega}_N$ to have a directional cosine close to $\mu = 1$, in order to approximate the directional cosine of the particles in the pencil beam. The reason for not including a discrete ordinate with $\mu_N = 1$ in the quadrature set is that the properties in 4.8 - 4.10 are not preserved in this case. In this thesis, we choose to preserve these properties by placing the discrete ordinates as presented in the previous section, and approximate the pencil beam with an ordinate $\hat{\Omega}_N$ with a directional cosine very close to but not equal to one.

4.3 Spatial Discretization

Since the focus of this thesis is on the Fokker-Planck operators, a simple discretization method is used for the spatial discretization: the step scheme. In the step scheme the 1D spatial domain is divided into NE cells, and the flux is approximated piecewise constant, see figure 4.3 (upper). We have one unknown per cell, let's say the average value. Now, in order to obtain a set of coupled equations, we integrate the 1D transport equation over each spatial cell. Operators L_a in the equation, which do not depend on the spatial variable x,

$$\frac{1}{\Delta x_i} \int_{x_{i-\frac{1}{2}}}^{x_{i+\frac{1}{2}}} L_a \varphi_n(x) dx \approx L_a \varphi_{i,n} \tag{4.12}$$

are left unchanged after integration and act on the flux of ordinate n in spatial cell i; $\varphi_{i,n}$. Here, Δx_i is the width of the i's cell. The only operator in the transport equation which does depend on the spatial variable x is the streaming operator, L_{str}. Straightforward integration of this operator leads to:

$$\frac{1}{\Delta x_i} \int_{x_{i-\frac{1}{2}}}^{x_{i+\frac{1}{2}}} L_{str} \varphi_n(x) dx = \frac{1}{\Delta x_i} \int_{x_{i-\frac{1}{2}}}^{x_{i+\frac{1}{2}}} \mu_n \frac{\partial \varphi_n(x)}{\partial x} dx = \frac{\mu_n}{\Delta x_i} \varphi_n(x) \Big|_{x_{i-\frac{1}{2}}}^{x_{i+\frac{1}{2}}}. \tag{4.13}$$

In order to choose which flux value to use on the discontinuous cell faces to perform above integration, we introduce the upwind scheme. In this scheme, the upwind side and the downwind side of a cell are defined such that the particles propagate from the upwind side to the downwind side of the cell. The value of the flux on the cell faces is chosen such that we simulate the direction of travel of the particles, by choosing the flux-value of the neighbor cell on the upwind side, and choosing the flux-value inside the cell on the downwind side, see figure 4.3 (bottom).

$$\varphi_n(x_{i-\frac{1}{2}}) \approx \varphi_{i,n} \text{ and } \varphi_n(x_{i+\frac{1}{2}}) \approx \varphi_{i+1,n} \text{ if } \mu_n > 0 \tag{4.14}$$

$$\varphi_n(x_{i-\frac{1}{2}}) \approx \varphi_{i-1,n} \text{ and } \varphi_n(x_{i+\frac{1}{2}}) \approx \varphi_{i,n} \text{ if } \mu_n < 0 \tag{4.15}$$

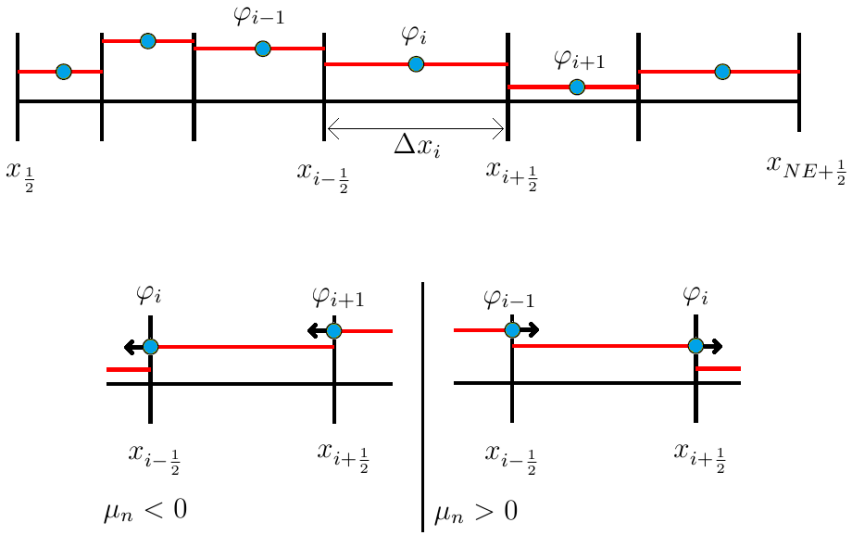

Figure 4.3: *Upper: representation of the step scheme. The 1D slab is divided into NE cells, the flux inside these cells is assumed to be constant, and allowed to be discontinuous an the cell faces. Bottom: representation of the upwind scheme in the spatial domain. If $\mu_n > 0$, the direction of the particle flow (from left to right) is simulated by assuming $\varphi_{i-\frac{1}{2}} = \varphi_{i-1}$ and $\varphi_{i+\frac{1}{2}} = \varphi_i$. Vice versa for $\mu_n < 0$.*

We use this scheme to obtain the final expression of the discretized streaming operator.

$$\frac{1}{\Delta x_i}\int_{x_{i-\frac{1}{2}}}^{x_{i+\frac{1}{2}}} L_{str}\varphi_n(x)dx \approx \frac{\mu_n\left(\varphi_{i-1,n}-\varphi_{i,n}\right)}{\Delta x_i} \text{ if } \mu_n > 0 \tag{4.16}$$

$$\frac{1}{\Delta x_i}\int_{x_{i-\frac{1}{2}}}^{x_{i+\frac{1}{2}}} L_{str}\varphi_n(x)dx \approx \frac{\mu_n\left(\varphi_{i,n}-\varphi_{i+1,n}\right)}{\Delta x_i} \text{ if } \mu_n < 0 \tag{4.17}$$

The discretization scheme presented here, is the simplest and most straightforward scheme available. It must be noted that this scheme suffers from large truncation errors: to obtain an accurate solution it is necessary to use a relatively large number of spatial cells. More advanced discretization schemes would require fewer cells, and thereby reduce computation time. This disadvantage of the step scheme is accepted in this thesis, since the focus is on the Fokker-Planck operators. In future work, however, solutions can be obtained more efficiently by, for example, introducing a linear discontinuous finite element method [18].

4.4 Energy Discretization

The standard method of discretization of the energy variable in the transport equation is the multi-group method. In this method the energy range is divided into a number of cells which are referred to as energy groups, see figure 4.4. Note that the energy group with the highest energy correspond to $g = 1$, and the direction of flow of the particles from $g = 1$ to $g = \text{NG}$, where NG is the total number of energy groups. In the spatial discretization scheme we have assumed a constant flux within the spatial cells. For the energy domain, however, we have used a more advanced discretization scheme: the linear discontinuous Galerkin method [18], see figure 4.5. In this scheme, the flux is assumed to be linear within the energy group, and is allowed to be discontinuous at the group faces.

The flux inside each energy group can be expressed with a set of two basis functions:

$$p^A(E) = p^0(E) = 1 \tag{4.18}$$

$$p^E(E) = p^1(E) = \frac{2}{\Delta E_g}(E - E_g) \tag{4.19}$$

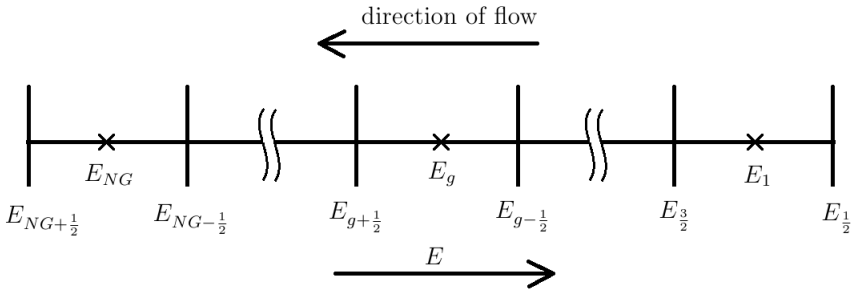

Figure 4.4: *Representation of the multi-group method. NG is the total number of energy groups used to divide the energy range. E_g is the center energy value of enegy group g. Protons move from $g = 1$ to $g = NG$ through the problem domain.*

where ΔE_g is the width of energy group g, and E_g is the center energy value of energy group g. With these basis functions, which are scaled Legendre functions, the flux is expressed as,

$$\varphi_{i,n,g}(E) \approx \varphi_{a,i,n,g} p^A(E) + \varphi_{e,i,n,g} p^E(E) \tag{4.20}$$

where $\varphi_{a,i,n,g}$ is the average of the flux in energy group g and $\varphi_{e,i,n,g}$ is the normalized slope of the flux in energy group g. The basis functions satisfy the following orthogonally property:

$$\int_{E_{g+\frac{1}{2}}}^{E_{g-\frac{1}{2}}} p^i(E) p^j(E) dE = \frac{\Delta E_g}{2j+1} \delta_{ij}. \tag{4.21}$$

Since we have two unknowns per energy group, the average flux and the normalized slope of the flux, we need two equations in each group to solve for these unknowns. The method to obtain this average and slope equation, is: (i) expand the flux in the transport equation into the two basis functions, (ii) multiply this equation by one of the basis functions, (iii) integrate this equation over the volume of an energy group, (iv) use the upwind scheme to evaluate the surface integrals. In this process, the total cross sections, the scatter cross sections, transport cross sections, and the energy straggling coefficient are assumed to be constant within each of the energy groups. The stopping power, on the other hand, is assumed to be linear continuous in the energy group.

The derivation of this average and slope equation is done in two steps; first, we discretize the operators L_a in the transport equation which do not act on the energy variable E. Second, the derivation of the continuous slowing down, Boltzmann scatter and the energy straggling operator for the average and slope equation is presented.

Straightforward integration of the operators which do not depend on the energy variable E,

$$\frac{1}{\Delta E_g} \int_{E_{g+\frac{1}{2}}}^{E_{g-\frac{1}{2}}} L_a \varphi_{i,n,g}(E) p^A(E) dE \approx L_a \varphi_{a,i,n,g} \tag{4.22}$$

results in an expression in which the operator L_a is left unchanged after integration and now acts on the average flux $\varphi_{a,i,n,g}$ of the energy group. The derivation of the slope equation for the operators L_a,

$$\frac{3}{\Delta E_g} \int_{E_{g+\frac{1}{2}}}^{E_{g-\frac{1}{2}}} L_a \varphi_{i,n,g}(E) p^E(E) dE \approx L_a \varphi_{e,i,n,g} \tag{4.23}$$

results in an expression with the operators L_a unchanged after integration, and now acting on the flux slope $\varphi_{e,i,n,g}$.

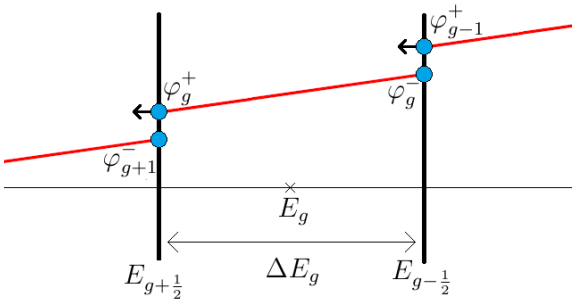

Figure 4.5: *Representation of the linear discontinuous Galerkin method. The flux is assumed linear inside the energy groups, and discontinuous on the group faces. Each energy group contains two unknowns, the average of the flux in the energy group $\varphi_{a,g}$ and the slope of the flux inside the energy group $\varphi_{e,g}$. φ^-_g and φ^+_g are the flux values on the boundaries of the energy group.*

The multi-group constants follow from a more general derivation of the multi-group method. For this derivation, the reader is referred to the work of Duderstadt and Hamilton [9]. Here, we only state the final result:

$$\sigma_{C,g} = \frac{\int_{E_{g+\frac{1}{2}}}^{E_{g-\frac{1}{2}}} \sigma_C(E)\varphi(E)dE}{\int_{E_{g+\frac{1}{2}}}^{E_{g-\frac{1}{2}}} \varphi(E)dE} \text{ and } \sigma_{tr,g} = \frac{\int_{E_{g+\frac{1}{2}}}^{E_{g-\frac{1}{2}}} \sigma_{tr}(E)\varphi(E)dE}{\int_{E_{g+\frac{1}{2}}}^{E_{g-\frac{1}{2}}} \varphi(E)dE}. \tag{4.24}$$

Note that in these expressions, the flux $\varphi(E)$ is unknown and has to be approximated beforehand. The SADCO code assumes a $\frac{1}{E}$ dependency for the flux in the energy range considered for proton therapy [15]. In this thesis, the multi-group constant $\sigma_{tr,g}$ is not evaluated as in 4.24, but at the center of the energy group ($\sigma_{tr,g} = \sigma_{tr}(E_g)$). As we will see in chapter 6, there is no need for a better approximation of this group constant, such as in equation 4.24

So far, we have demonstrated how to obtain expressions for the average and energy slope equations for operators which do not act on the energy variable. The Boltzmann scatter operator, the continuous slowing down operator and the energy straggling operator, on the other hand, do act on the energy variable. In the following sections, we demonstrate how these operators can be discretized using the multi-group linear discontinuous Galerkin method.

4.4.1 The Boltzmann Scatter Operator

We assume the medium in which the protons propagate to be isotropic. In isotropic media, the scatter angle of the proton is independent of the angle in which the proton approaches the material. With this assumption, the differential cross section depends on the scattering angle $\hat{\Omega}' \cdot \hat{\Omega} = \mu_0$ only, instead on both $\hat{\Omega}$ and $\hat{\Omega}'$. The expression of the Boltzmann scatter operator with this assumption, together with the multi-group approximation, results in:

$$L_B\varphi_{i,n,g}(E) = \sum_{g'=1}^{g} \int_{E_{g'+\frac{1}{2}}}^{E_{g'-\frac{1}{2}}} \sum_{n'=1}^{N} \sigma_C(E' \to E, \hat{\Omega}_{n'} \to \hat{\Omega}_n)\varphi_{i,n,g}(E')dE'. \tag{4.25}$$

In this first step, we have used the multi-group method to break up the integral over E'. Note that we sum up to energy group $g' = g$ since we assume no upscatter in the simulation (the protons can only lose energy in the catastrophic scatter interactions). In the second step, we expand the angular flux and the differential cross section in a Legendre series of degree L, and integrate the resulting expression, multiplied by the corresponding basis function, over an energy group to obtain the expression of the Boltzmann scatter

operator in the average and slope equations. For the average equation:

$$\frac{1}{\Delta E_g}\int_{E_{g'+\frac{1}{2}}}^{E_{g'-\frac{1}{2}}} p^A(E)L_B\varphi_{i,n,g}(E) \approx \sum_{g'=1}^{g}\sum_{l=0}^{L}\frac{2l+1}{4\pi}\sigma_{C,g'\to g,l}\phi_{i,g',l}P_l(\mu_n)\frac{\Delta E_{g'}}{\Delta E_g} \tag{4.26}$$

with,

$$\phi_{i,g,l} = \sum_{n=1}^{N} P_l(\mu_n)\varphi_{a,i,n,g}w_n \tag{4.27}$$

where $\sigma_{s,g'\to g,l}$ are the Legendre moments of the regular multi-group cross section $\sigma_{s,g'\to g}(\mu_0)$. For the slope equation:

$$\frac{3}{\Delta E_g}\int_{E_{g'+\frac{1}{2}}}^{E_{g'-\frac{1}{2}}} p^E(E)L_B\varphi_{i,n,g}(E) \approx 0. \tag{4.28}$$

Here we have used the following assumption:

$$\int_{E_{g'+\frac{1}{2}}}^{E_{g'-\frac{1}{2}}} \sigma_C(E'\to E,\mu_0)p^E(E)dE \approx 0. \tag{4.29}$$

If we used the complete linear discontinuous treatment of the scattering source, we would end up with nonzero scattering source energy slopes. In this thesis, however, we ignore this slope scattering source for two reasons. The first reason is simplicity: the solution converges to the same solution if these scatter source energy slopes were included. The second reason is that we would need multi-group scatter moments for these scatter source energy slopes. For the average source, the multi-group Legendre moments $\sigma_{s,g'\to g,l}$ are generated by the SADCO code. For the energy slopes, however, we do not have such a code available.

For a derivation of the expression of the multi-group Legendre scatter cross section, the reader is referred to the work of Duderstadt and Hamilton [9]. The final result of this derivation is:

$$\sigma_{C,g'\to g}(\mu_0) \approx \sigma_{C,g'\to g}(\mu_0,\hat{\Omega}') = \frac{\int_{E_{g-\frac{1}{2}}}^{E_{g+\frac{1}{2}}}\int_{E_{g'-\frac{1}{2}}}^{E_{g'+\frac{1}{2}}}\sigma_C(E'\to E,\mu_0)\varphi(\hat{\Omega}',E')dE'dE}{\int_{E'_{g-\frac{1}{2}}}^{E'_{g+\frac{1}{2}}}\varphi(E',\hat{\Omega}')dE'} \tag{4.30}$$

where the assumption is made that the medium is isotropic, i.e. the scatter cross section does not depend on the incoming direction $\hat{\Omega}'$ of the proton. These group to group differential scatter cross sections are generated by the SADCO code, which uses a $\frac{1}{E}$ dependency of the flux in the energy groups. The SADCO code gives the moments of the Legendre expansion of these group to group differential cross sections. Since these differential cross sections are relatively smooth functions, these cross sections can be represented by a relatively low order Legendre expansion L. In this thesis, we assumed $L = 10$ is sufficient to represent these cross sections, since the cross section are relatively smooth, and the effect on the solution of this scatter process is relatively small.

4.4.2 Continuous Slowing Down Operator

The stopping power $S(E)$ is an important parameter in the transport equation: it determines the range of the protons and is the main contributor to energy deposition. Due to its importance, and because it is strongly varying in energy, it is assumed to be linear within an energy group, and continuous on the group faces (in contrast to the other multi-group

parameters, which were assumed to be constant within the group). The stopping power in an energy group is expressed with the same set of basis function as the flux in the energy groups,

$$S(E) = \frac{S_{g+\frac{1}{2}} + S_{g-\frac{1}{2}}}{2} p^A(E) + \frac{S_{g-\frac{1}{2}} - S_{g+\frac{1}{2}}}{2} p^E(E) \tag{4.31}$$

where $S_{g\pm\frac{1}{2}}$ are the values of the stopping power on the faces of the energy group, and are evaluated using equation 3.28, with $E = E_{g\pm\frac{1}{2}}$.

To obtain an expression of the continuous slowing down operator L_{CSD} in the average equation, the operator is multiplied by the basis function $p^A(E)$, and subsequently integrated over the volume of an energy group.

$$\begin{aligned}\frac{1}{\Delta E_g}\int_{E_{g+\frac{1}{2}}}^{E_{g-\frac{1}{2}}} L_{CSD}\varphi_{i,n,g}(E)p^A(E) &= \frac{1}{\Delta E_g}\int_{E_{g+\frac{1}{2}}}^{E_{g-\frac{1}{2}}} \frac{\partial}{\partial E} S(E)\varphi_{i,n,g}(E)p^A(E) \\ &\approx \frac{S_{g-\frac{1}{2}}}{\Delta E_g}(\varphi_{a,i,n,g-1} - \varphi_{e,i,n,g-1}) - \frac{S_{g+\frac{1}{2}}}{\Delta E_g}(\varphi_{a,i,n,g} - \varphi_{e,i,n,g})\end{aligned} \tag{4.32}$$

Here, we have used the upwind scheme to evaluate the surface integral. Since the protons have a unique direction of travel through the energy domain, from high energy to low, the upwind neighbor is energy group $g-1$, see figure 4.5.

For the slope equation, we multiply the continuous slowing down operator by $p^E(E)$ and integrate over an energy group,

$$\begin{aligned}\frac{3}{\Delta E_g}\int_{E_{g+\frac{1}{2}}}^{E_{g-\frac{1}{2}}} L_{CSD}\varphi_{i,n,g}(E)p^E(E)dE &= -\frac{3}{\Delta E_g}\int_{E_{g+\frac{1}{2}}}^{E_{g-\frac{1}{2}}} S(E)\varphi_{i,n,g}(E)\frac{\partial p^E(E)}{\partial E}dE \\ &+\frac{3}{\Delta E_g}\left[p^E(E)S(E)\varphi_{i,n,g}(E)\right|_{E_{g+\frac{1}{2}}}^{E_{g-\frac{1}{2}}} \approx -3\frac{S_{g+\frac{1}{2}} + S_{g-\frac{1}{2}}}{\Delta E_g}\varphi_{a,i,n,g} \\ -\frac{S_{g-\frac{1}{2}} - S_{g+\frac{1}{2}}}{\Delta E_g}\varphi_{e,i,n,g} &+ 3\frac{S_{g-\frac{1}{2}}}{\Delta E_g}(\varphi_{a,i,n,g-1} - \varphi_{e,i,n,g-1}) - 3\frac{S_{g+\frac{1}{2}}}{\Delta E_g}(\varphi_{a,i,n,g} - \varphi_{e,i,n,g})\end{aligned} \tag{4.33}$$

where the upwind scheme is used to evaluate the surface integral.

The result of the discretization of the continuous slowing down operator is a coupled set of terms in the average and slope equation: both the average and the slope equation of group g depends on both the average and the slope of the flux in group g.

4.4.3 Energy Straggling Operator

In this thesis, we use a simple finite volume method to discretize the energy straggling operator L_{ES} for the average equation, and its contribution to the slope equation is ignored. This simplified discretization is used because the discontinuous Galerkin method is difficult to apply on diffusion operators. The solution converges to the same solution we would have obtained if we had used the fully discretized energy straggling operator in the slope equation.

Straightforward integrating of the energy straggling operator with the finite volume approach leads to:

$$\begin{aligned}\frac{1}{\Delta E_g}\int_{E_{g+\frac{1}{2}}}^{E_{g-\frac{1}{2}}} p^A(E)L_{ES}\varphi_{i,n,g}(E) &= \frac{1}{\Delta E_g}\int_{E_{g+\frac{1}{2}}}^{E_{g-\frac{1}{2}}} p^A(E)\frac{1}{2}\frac{\partial^2}{\partial E^2}T(E)\varphi_{i,n,g}(E) \\ &= \frac{1}{\Delta E_g}\left[\frac{1}{2}\frac{\partial}{\partial E}T(E)\varphi_{i,n,g}(E)\right|_{E_{g+\frac{1}{2}}}^{E_{g-\frac{1}{2}}} \\ \approx \frac{1}{\Delta E_g}\frac{(T\varphi_{a,i,n})_{g-1} - (T\varphi_{a,i,n})_g}{\Delta E_g + \Delta E_{g-1}} &- \frac{1}{\Delta E_g}\frac{(T\varphi_{a,i,n})_g - (T\varphi_{a,i,n})_{g+1}}{\Delta E_{g+1} + \Delta E_g}.\end{aligned} \tag{4.34}$$

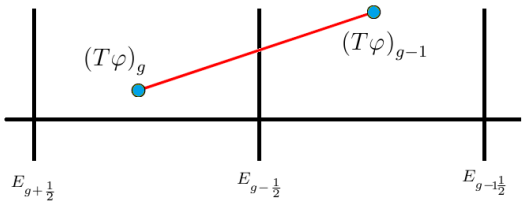

Figure 4.6: *Representation of the finite volume method used to evaluate the derivative in the expression of the discretized energy straggling operator.*

In figure 4.6 is depicted how the finite volume method is used to evaluate the derivatives on the energy group faces.

4.5 Conclusions

In this thesis, three methods are used to discretize the three independent variables μ, x and E in the 1D transport equation: the S_N method, the step scheme and the discontinuous Galerkin method respectively.

In the S_N method, the direction of travel of the particles is approximated with a set of N discrete ordinates, together forming the quadrature set. By integrating the 1D transport equation over the volume surrounding these discrete ordinates, a set of N coupled equations is obtained, describing the flux in these ordinates.

The step scheme is the most simple and straightforward discretization method available: it suffers from large truncation errors. In this method, the spatial range is divide into NE spatial cells, and the flux is assumed constant inside the cells and discontinuous on the cell faces. A coupled set of NE equations describing the flux in these spatial cells is obtained by integrating the 1D transport equation over the volume of these cells. The upwind scheme is used to simulate the direction of flow of the particles through the problem domain.

The energy variable is discretized using a combination of the multi-group method and the Galerkin method. In the multi-group method, the energy range is divided into NG energy groups. In the Galerkin method, the flux is assumed to be linear within these energy groups and discontinuous on the group faces. The direction of travel of the particles through the energy domain is simulated using the upwind method. By integrating the transport equation, multiplied by the corresponding basis function, over the volume of the groups, a coupled set of NG average equations and NG slope equations is obtained. The contributions of the Boltzmann scatter operator and the energy straggling operator to the slope equations are neglected.

The result of the three discretization methods is a coupled set of 2×N×NE×NG equations. In the following chapter, the method is presented which is used to solve this, generally large, set of coupled equations.

5. Numerical Solution of the Discretized System

The result of discretization of the transport equation in all of its independent variables is a set of coupled linear equations describing the particle field. The size of this set depends on the number of cells in which we divide the problem domain. For a typical 1D problem considered in this thesis, the number of equations in the set is large: in the order of $10^7 - 10^9$, depending on the type of boundary condition problem. These equations are solved with the help of a computer. In the following sections, we demonstrate the methods used in the computer code to efficiently solve the set of equations.

With this computer code, the particle field can be evaluated from the set of equations. However, the quantity of interest in proton therapy planning is not the particle field itself, but the distribution of deposited energy over the problem domain. In the final section of this chapter we demonstrate how to obtain this energy deposition profile from the particle field.

5.1 The Iterative Method

The linear Boltzmann-Fokker-Planck equation consists of streaming, diffusion, source and removal operators. Streaming is the main process in proton transport. The flows in this process have a unique direction through the problem domain. This is illustrated with help of figure 5.1, where the flows in ordinate $\hat{\Omega}_N$ are shown. On the top left, particles stream into the system through the spatial domain (here only a boundary condition is imposed on the energy group $g = 1$, depending on the type of boundary condition multiple energy groups can have boundary conditions). The flows from the left to the right of the picture represent the free movement of the particles through the spatial domain. As the protons stream through the slab they slow down due to interaction with the atomic electrons. This process is described by the continuous slowing down operator and represented in this figure by the stream of particles down the energy domain. At the bottom ($E = E_{NG+\frac{1}{2}}$) the particles stream out of the system through the final energy boundary. The remaining energy of the protons, which is $E_{NG+\frac{1}{2}} = 1$ MeV in our work, is assumed to be deposited locally.

The two equations which describe the angular flux in one such cell in figure 5.1 can be expressed in the following matrix system:

$$\begin{pmatrix} a_{11} & a_{12} \\ a_{21} & a_{22} \end{pmatrix} \begin{pmatrix} \varphi_{a,i,n,g} \\ \varphi_{e,i,n,g} \end{pmatrix} = \begin{pmatrix} c_1 \\ c_2 \end{pmatrix}. \tag{5.1}$$

The average and slope equation are solved together as they are strongly coupled. This matrix system is used as the basic building block to solve the large set of equations. The general idea here is to use 5.1 to solve the flux-value in cell i, n, g, using the most up to date flux-values for the matrix coefficients. These cells are than solved in the direction of the flows, starting at the top left of figure 5.1 if $\mu_n > 0$, and starting at the top right if $\mu_n < 0$. One successive solution through the angular and spatial range of a single energy group is referred to as a sweep.

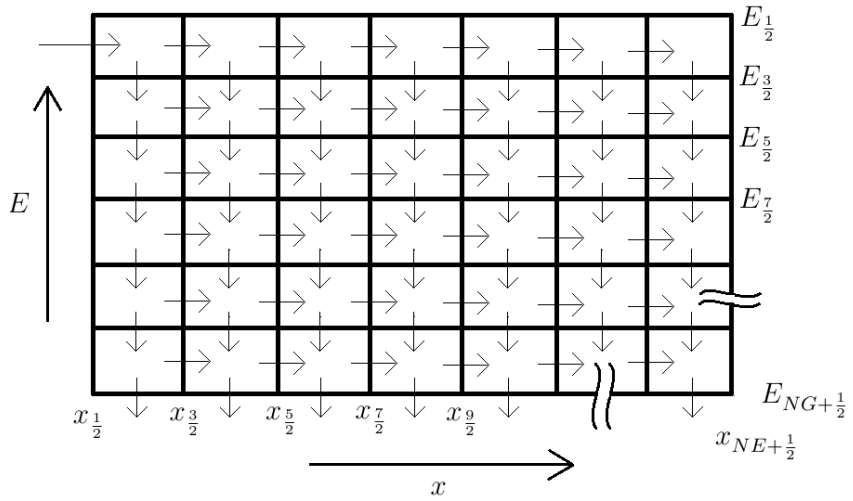

Figure 5.1: *Representation of the particle flow through the spatial and the energy range along ordinate $\hat{\Omega}_N$. In this ordinate the particles stream from left to right through the spatial domain ($\mu_N > 0$), described by the streaming operator L_{str}, and from top to bottem through the energy domain, described by the continuous slowing down operator L_{CSD}. In the iterative method, the flux-values are solved in the direction of these flows. Note that the flows in the spatial domain are reversed if $\mu_n < 0$. The particles streaming out of the final energy group are assumed to deposit their energy locally. In this thesis $E_{NG+\frac{1}{2}} = 1$ MeV. No particles stream through the final spatial element if the spatial range is sufficiently large.*

Sweep:
for $n = N$ to $n = 1$ **do**
  if $\mu_n > 0$ **then**
    for $i = 1$ to $i = NE$ **do**
      Solve matrix system 5.1 for $\varphi_{a,i,n,g}$ and $\varphi_{e,i,n,g}$
    end for
  else
    for $i = NE$ to $i = 1$ **do**
      Solve matrix system 5.1 for $\varphi_{a,i,n,g}$ and $\varphi_{e,i,n,g}$
    end for
  end if
end for

The flux-values in the discrete ordinates are coupled through the scatter operators. The continuous scatter operator contains a second order derivative in angle, see equation 3.18. Discretization of second order derivatives results in an expression containing the flux-values of both neighbors, in this case the flux-values in both neighbor ordinates of ordinate n: (φ_{n-1} and φ_{n+1}), see equation 4.5. As a consequence, unknowns appear in the expression for the matrix system 5.1. Therefore an iterative procedure is necessary to obtain a solution of this part of the system. In this iterative procedure, the sweep is repeated using the most up-to-date flux-values (the Gauss-Seidel method [1]) until some convergence criterion is met.

The expression of the energy straggling operator contains a second order derivative in energy, see equation 3.21. Discretization of this operator results in an expression containing the flux-values of both neighbor energy groups of energy group g: φ_{g-1} and φ_{g+1}, see equation 4.34. A similar iterative procedure as with the continuous scatter operator is used to obtain a solution for this part of the system. This iterative procedure is also repeated until some convergence criterion is met. The solution of the system is obtained

when both convergence criteria are met.

Iterative procedure:
repeat
  for $g = 1$ to $g = NG$ **do**
    repeat
      for $n = N$ to $n = 1$ **do**
        Sweep
      end for
      Update scatter source
    until convergence
  end for
until convergence

The inner iterations are for convergence of the continuous scatter and Boltzmann scatter operator. The outer iterations are for convergence of the energy straggling operator.

The iterations are repeated until the convergence criterion is met. In order to quantify the convergence in a solution, we introduce the residual $r^l_{i,n,g}$, which is a measure for the change of the flux-value in spatial cell i, discrete ordinate n and energy group g after iteration l.

$$r^l_{i,n,g} = |c|^l - A\varphi^{l-1} \tag{5.2}$$

where

$$|c| = \sqrt{c_1^2 + c_2^2} \tag{5.3}$$

and A is the matrix on the left hand side, and c the vector on the right hand side of matrix system 5.1. The residual is a measure for change in the solution after iteration l. Only if the residual is small enough, the solution is assumed to be converged. The criterion used in our work,

$$\max\left(\frac{r^l_{i,n,g}}{|c|^l}\right) \leq 10^{-8} \tag{5.4}$$

was semi-arbitrarily chosen, based on inspection of solutions with smaller and larger convergence criteria.

The diffusion operators in the transport equation, make the calculation computationally very demanding. In a typical calculation performed in this thesis, using a S_{40} quadrature set approximately 500 inner iteration are necessary to converge the solution. In future work, computation time can be gained in accelerating the iterative processes to obtain the solution of these diffusive operators.

5.2 Energy Deposition

After obtaining the solution of the transport equation, we have the particle distribution in the problem range. To determine the distribution of the deposited energy, we make use of a quantity called the energy flux $\Phi^E(\vec{r})$.

$$\Phi^E(\vec{r}) = \int_0^\infty \int_{4\pi} E\varphi(\vec{r}, E, \hat{\Omega}) d\hat{\Omega} dE. \tag{5.5}$$

This quantity can be seen as the amount of energy going through the surface of the unit sphere per unit time at a certain point $\vec{r}$ in the problem domain and is used to obtain a

balance equation of energy in a spatial cell. Multiplication of the transport equation by the energy E, and integrating the resulting equation over the angular and energy domain and over a single spatial cell, results in this balance equation of energy in that spatial cell.

$$\begin{aligned}
&\int_{E_{NG+\frac{1}{2}}}^{E_{\frac{1}{2}}} \int_{x_{i-\frac{1}{2}}}^{x_{i+\frac{1}{2}}} \int_{4\pi} E \cdot (\text{Transport Equation})\, dx dE d\hat{\Omega} \\
&= \int_{E_{NG+\frac{1}{2}}}^{E_{\frac{1}{2}}} \int_{x_{i-\frac{1}{2}}}^{x_{i+\frac{1}{2}}} \int_{4\pi} E\mu \frac{\partial \varphi}{\partial x} dx dE d\hat{\Omega} + \int_{E_{NG+\frac{1}{2}}}^{E_{\frac{1}{2}}} \int_{x_{i-\frac{1}{2}}}^{x_{i+\frac{1}{2}}} \int_{4\pi} E\sigma_{C,s}\varphi dE \qquad (5.6) \\
&= \int_{E_{NG+\frac{1}{2}}}^{E_{\frac{1}{2}}} \int_{4\pi} E \frac{\partial S(E)\varphi}{\partial E} dx dE + \int_{E_{NG+\frac{1}{2}}}^{E_{\frac{1}{2}}} \int_{x_{i-\frac{1}{2}}}^{x_{i+\frac{1}{2}}} \int_{4\pi} \sum_{g'=1}^{g} E\sigma_{C,g'\to g}\varphi_{g'} \Delta E' dx dE
\end{aligned}$$

here we used

$$E \int_{4\pi} \frac{\sigma_{tr}}{2} \left(\frac{\partial}{\partial \mu} \left[\left(1-\mu^2\right) \frac{\partial \varphi}{\partial \mu} \right] \right) d\hat{\Omega} = 0 \qquad (5.7)$$

and

$$\int_{E_{NG+\frac{1}{2}}}^{E_{\frac{1}{2}}} E \frac{\partial^2 T(E)\varphi(E)}{\partial E^2} \approx 0. \qquad (5.8)$$

Equation 5.7 represents the redistribution of the energy flux over the unit sphere. Since no energy flux is created in this process, this term does not contribute to the balance equation. In equation 5.8, we assumed the contribution of the energy straggling term to be negligible, due to the small effect of this term to the solution. The result in equation 5.6 contains energy streaming, energy deposition, and energy source terms. In the following section, these terms are identified.

5.2.1 Identification of Streaming, Deposition and Source Terms

In this section, we evaluate the integrals in equation 5.6 term by term. In the resulting expressions the streaming, deposition and source terms are identified.

After performing the integration on the streaming operator,

$$\int_{E_{NG+\frac{1}{2}}}^{E_{\frac{1}{2}}} \int_{x_{i-\frac{1}{2}}}^{x_{i+\frac{1}{2}}} \int_{4\pi} E\mu \frac{\partial \varphi}{\partial x} d\hat{\Omega} dx dE \approx \sum_{n=1}^{N} w_n \mu_n \sum_{g=1}^{NG} \int_{E_{g+\frac{1}{2}}}^{E_{g-\frac{1}{2}}} E \left(\varphi_{i+\frac{1}{2},n,g}(E) - \varphi_{i-\frac{1}{2},n,g}(E) \right) \qquad (5.9)$$

two streaming terms are recognized. They represent the nett energy flow through the spatial faces of the cell. No deposition or source terms result from the integration.

The continuous slowing down operator represents the Coulomb interaction process of the incident protons with the atomic electrons. In this process, energy is transferred from the incident proton to the atomic electrons. After using partial integration,

$$\begin{aligned}
&\int_{E_{NG+\frac{1}{2}}}^{E_{\frac{1}{2}}} \int_{x_{i-\frac{1}{2}}}^{x_{i+\frac{1}{2}}} \int_{4\pi} \frac{\partial S(E)\varphi(r,E)}{\partial E} E d\hat{\Omega} dx dE \\
&\approx \Delta x_i \sum_{n=1}^{N} w_n \sum_{g=1}^{NG} \left(- \int_{E_{g+\frac{1}{2}}}^{E_{g-\frac{1}{2}}} S(E)\varphi_{i,n,g}(E) dE + S(E)\varphi_{i,n,g}(E) E \Big|_{E_{g-\frac{1}{2}}}^{E_{g+\frac{1}{2}}} \right) \qquad (5.10)
\end{aligned}$$

we recognize a streaming term, and therefore the remaining term is must be a deposition term. The deposition term is further evaluated to a relation which expresses the deposited

energy to the atomic electrons in the spatial cell:

$$\int_{E_{g+\frac{1}{2}}}^{E_{g-\frac{1}{2}}} S(E)\varphi_{i,n,g}(E)dE \approx \varphi_{a,i,n,g}\frac{S_{g+\frac{1}{2}}+S_{g-\frac{1}{2}}}{2}\Delta E_g + \varphi_{e,i,n,g}\frac{S_{g-\frac{1}{2}}-S_{g+\frac{1}{2}}}{2}\frac{\Delta E_g}{3}. \quad (5.11)$$

The intern energy flows in the spatial cell through the energy domain do not contribute to energy deposition. However, the energy carried by the particles which stream out of the system through the final energy boundary $E = E_{NG+\frac{1}{2}}$, is assumed to be deposited locally. This flow is expressed as,

$$S(E)\varphi_{i,n,g}(E)E|_{E_{NG+\frac{1}{2}}} = S_{NG+\frac{1}{2}}\varphi_{i,n,NG+\frac{1}{2}}E_{NG+\frac{1}{2}} = S_{NG+\frac{1}{2}}\left(\varphi_{a,i,n,NG}-\varphi_{e,i,n,NG}\right)E_{NG+\frac{1}{2}} \quad (5.12)$$

and is added to the deposited energy.

The total removal operator in equation 5.6 represents the total amount of energy which is removed due to the catastrophic scatter interactions. In this process, protons with energy E are removed from the equation, and secondary particles with energy $E_s < E$ are introduced into the system. The expression for the total amount of energy lost in this process,

$$\begin{aligned}&\int_{E_{NG+\frac{1}{2}}}^{E_{\frac{1}{2}}}\int_{x_{i-\frac{1}{2}}}^{x_{i+\frac{1}{2}}}\int_{4\pi} E\sigma_{C,s}\varphi d\hat{\Omega}dxdE\\ &\approx \Delta x_i\sum_{n=1}^{N}w_n\sum_{g=1}^{NG}\sigma_{C,g}\left(\frac{1}{6}\Delta E_g^2\varphi_{e,i,n,g}+E_{g-\frac{1}{2}}\varphi_{a,i,n,g}\Delta E_g-\frac{1}{2}\Delta E_g^2\varphi_{a,i,n,g}\right)\end{aligned} \quad (5.13)$$

is an energy deposition term. The secondary protons can carry their energy over a significant range. The expression of this energy is obtained by performing the integral in equation 5.6:

$$\begin{aligned}&\int_{E_{NG+\frac{1}{2}}}^{E_{\frac{1}{2}}}\int_{x_{i-\frac{1}{2}}}^{x_{i+\frac{1}{2}}}\int_{4\pi}\left(\sum_{g'=1}^{g}E\sigma_{C,g'\to g}\varphi_{a,i,n,g'}\Delta E_{g'}\right)d\hat{\Omega}dxdE\\ &\approx \Delta x_i\sum_{n=1}^{N}w_n\sum_{g=1}^{NG}\sum_{g'=1}^{g-1}\sigma_{C,g'\to g}\varphi_{a,i,n,g'}\Delta E_{g'}\left(\frac{1}{2}E_{g-\frac{1}{2}}^2-\frac{1}{2}E_{g+\frac{1}{2}}^2\right)\\ &+\sum_{g=1}^{NG}\sum_{n=1}^{N}w_n\Delta x_i\sigma_{C,g\to g}\left(\frac{1}{6}\Delta E_g^2\varphi_{e,i,n,g}+E_{g-\frac{1}{2}}\varphi_{a,i,n,g}\Delta E_g-\frac{1}{2}\Delta E_g^2\varphi_{a,i,n,g}\right).\end{aligned} \quad (5.14)$$

Since this is a source of energy, this expression is subtracted from the total energy deposition obtained so far. In our work, we have ignored the energy carried by the secondary neutrons, and other secondary particles. If they would have been included, more source terms would show up here, and some of the energy, which now is assumed to be deposited, would have been carried to other parts of the problem domain. This results in somewhat higher energy deposition in the areas where the creation of these secondary particles is significant.

Figure 5.2 shows a schematic overview of the energy flow, source, and deposition terms in spatial cell x_i of the particles streaming along ordinate $\hat{\Omega}_n$ which are identified in this section.

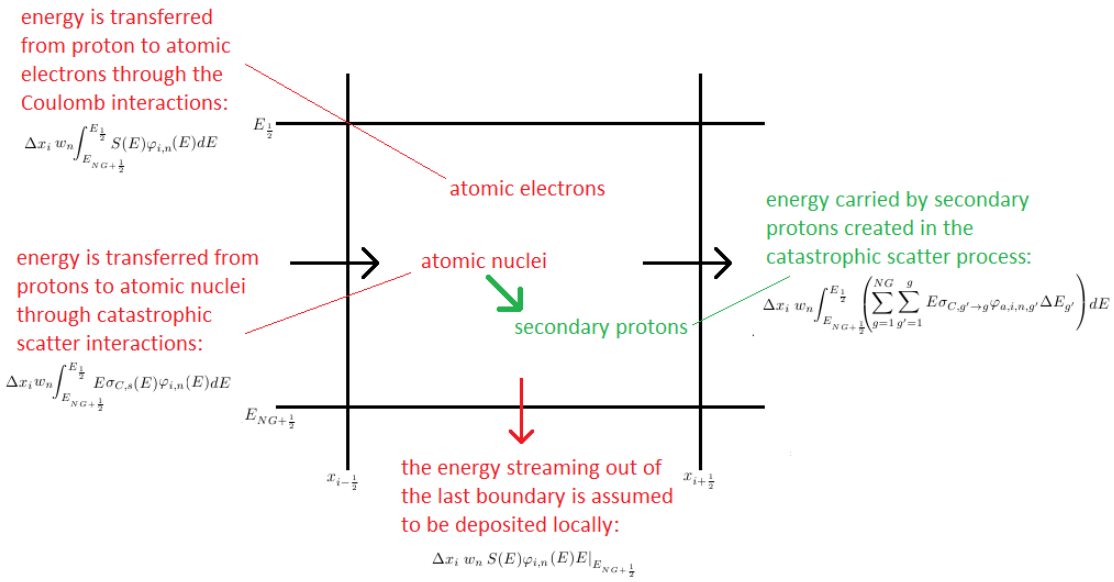

Figure 5.2: *Schematic representation of the energy transport in spatial cell i and ordinate $\hat{\Omega}_n$ with $\mu_n > 0$. The energy streams in and out of the spatial cells carried by the protons through the spatial domain. Due to the scatter interactions, energy is transferred to atomic nuclei and atomic electrons. The secondary protons created in the catastrhopic scatter process can carry their energy to other cells. The terms in red are energy deposition terms, the green one is an energy source term.*

5.2.2 Dose

The energy deposited E_{dep} in tissue is distributed over the mass in that tissue. This energy causes molecular bonds to break, and energy structures to be altered. These effects are the basis of the interference with the cancerous cells. A better measure for the damage in these cells is the deposited dose. Dose expresses the energy absorption by the medium per unit of mass:

$$D(\vec{r}) \equiv \frac{E_{dep}(\vec{r})}{\rho(\vec{r})}. \tag{5.15}$$

In treatment planning, this is the quantity which is considered.

5.3 Conclusions

The set of coupled equations, obtained in the discretization process described in the previous chapter, is solved by the use of an iterative method. In this method, the slope equation and the average equation are solved together and is used as the basic building block in solving the system. The cells are solved in the direction of the flows (along the ordinate directions and down the energy domain), starting at ($i = 1$, $g = 1$, $n = N$). This is repeated until both convergence criteria are met. To quantify the convergence, the residual is defined which is a measure for change in the flux values after an iteration. The convergence criterion is set based on inspection of solutions with more and less strict criteria.

An energy flux balance equation is obtained by the multiplication of the transport equation by the energy variable E, and integrating the result over energy, angle and a single spatial cell. In this balance equation the in and out flows terms are identified. The remaining terms signify energy deposition or source terms.

6. Investigation of Discretization Requirements

In chapter 4, we have obtained a set of coupled equations by discretization of the 1D transport equation in all of its independent variables. The number of equations in the set depends on the level of discretization we use. If we use a high level of discretization, we can obtain a very accurate solution, which is referred to as the converged solution. However, the computation time and the storage space required to obtain this solution will be large. If we, on the other hand, use a low level of discretization, the solution looses accuracy. Therefore, we want to obtain an accurate solution with a minimum level of discretization. In this chapter, we investigate what level of discretization is necessary to obtain an accurate enough solution. In other words; what is the minimum amount of cells in which we need to divide the energy, angular and spatial range, and how should we distribute these cells over the ranges, in order to produce accurate results as efficiently as possible.

By focusing on simplified versions of the Boltzmann-Fokker-Planck equation, we are able to efficiently investigate the level of discretization necessary in an independent variable. We assume the number of cells needed to obtain a converged solution in a test case from table 6.1 to be the same as in the total transport equation.

Table 6.1: *The three test cases in which we investigate the discretization requirements. The discretization requirement in a variable in the total transport equation is determined by the most strict discretization requirement of the test cases.*

test case	transport equation	error equation
A	$\mu\frac{\partial\varphi}{\partial x}+\sigma_{C,s}\varphi=\frac{\partial S\varphi}{\partial E}$	$\epsilon=\frac{\int_0^\infty\left(D_{ref}-D\right)^2dx}{\int_0^\infty D_{ref}^2dx}$
B	$\mu\frac{\partial\varphi}{\partial x}=\frac{\sigma_{tr}}{2}\left[\frac{\partial}{\partial\mu}\left(1-\mu^2\right)\frac{\partial\varphi}{\partial\mu}\right]$	$\epsilon=\frac{\int_0^\infty\int_{-1}^1\left(\varphi_{ref}-\varphi\right)^2d\mu dx}{\int_0^\infty\int_{-1}^1\varphi_{ref}^2d\mu dx}$
C	$\frac{\partial S\varphi}{\partial E}=-\frac{\sigma_{tr}}{2}\left[\frac{\partial}{\partial\mu}\left(1-\mu^2\right)\frac{\partial\varphi}{\partial\mu}\right]$	$\epsilon=\frac{\int_0^\infty\int_{-1}^1\left(\varphi_{ref}-\varphi\right)^2d\mu dE}{\int_0^\infty\int_{-1}^1\varphi_{ref}^2d\mu dE}$

Note that we did not include the Boltzmann scatter operator and the energy straggling term in the test cases. The effects of these operators on the solution are assumed to be small, and therefore not to have a large effect on the choice of angular, spatial and energy discretization required.

Each of the transport equations in the test cases in table 6.1 contain two independent variables: x and E in test case A, x and μ in test case B, and E and μ in test case C. The discretization requirement of one such variable is investigated by performing multiple calculations with a varying levels of discretization in this variable, while using a fixed level of discretization in the other variable. The error in one such calculation is evaluated by comparing it to a reference solution. In this reference solution, the discretization level is as high as possibly allowed by computation time and storage space limitations, and we assume this solution to be fully converged. The error equation in test case A compares the

Table 6.2: *General computational set-up of the test cases, where NE_{ref}, NG_{ref}, and N_{ref} are the number of cells in the reference calculation.*

	fraction % by weight								
Material	H	C	O	$\rho\ [\frac{g}{cm^3}]$	$S(E_{g\pm\frac{1}{2}})$	$\sigma_{tr}(E_g)$	NE_{ref}	NG_{ref}	N_{ref}
PMMA	8	60	32	1.18	Eq. 3.28	Eq. 3.19	100000	10000	500

dose distribution D over the spatial domain to the dose distribution D_{ref} of the reference solution. The error functions in test cases B and C compare the angular flux φ over the problem domain to the angular flux φ_{ref} of the reference reference solution.

The discretization requirement of a single variable is set by the most strict requirement for the discretization of that variable in any of the test cases. The error ϵ which is allowed in the system depends on the problem at hand. In this thesis, we assumed the following error criterion to be acceptable in proton therapy planning:

$$\epsilon \leq 10^{-4}. \tag{6.1}$$

See section 7.1.1 for more details on how this semi-arbitrary criterion was chosen.

6.1 General Computational Set-up

Here, the general set-up of the test cases is presented regarding the geometry, the material, the boundary conditions which are used, and the structure of the discretization. These settings are used in all of the test cases, unless stated otherwise in the computational set-up section of the corresponding test case. In these sections, the more specific computational set-up is presented of the corresponding test case.

6.1.1 Geometry and Material

The 1D geometry can be visualized in 3D as an infinite large slab, see figure 3.7 (left). This slab is uniformly irradiated from the left side.

The Monte Carlo benchmark cases are calculations performed on PMMA. PMMA, or polymethylmethacrylate, is a transparent plastic which closely resembles the properties of human tissue. Phantoms are often made out of PMMA, which are used as model for the human body with the purpose of measuring the dose deposition in a certain environment. Since this material closely resemble the tissue of a patient, this material is assumed to be a good representation of the materials encountered in proton therapy. Therefore this material is, just as in the benchmark cases, used in the test cases as well. The physical properties of PMMA can be found in table 6.2.

6.1.2 Boundary Condition

The boundary condition is set to mimic a pencil beam on the left side of the 1D slab. In this boundary condition, the particles stream into the problem domain in the first spatial element ($i = 1$). Therefore, the boundary condition φ_{BC} is imposed on the first spatial element in the streaming operator ($L_{str} = \mu\frac{\partial}{\partial x}$). To approximate the pencil beam direction ($\mu = 1$) of the particles, the boundary condition is imposed on the discrete ordinate with the directional cosine closest to one: $\varphi_{BC}(\hat{\Omega}_N) \neq 0$ and $\varphi_{BC}(\hat{\Omega}_{n\neq N}) = 0$.

Two types of boundary conditions are investigated: the mono-energetic boundary condition (which gives rise to a Bragg peak), and the energy plateau boundary condition, see figure 6.1 (which gives rise to a SOBP). In this figure, the two energy plateau boundary conditions with $\Delta E_p = 25$ MeV and $\Delta E_p = 50$ MeV are shown which are investigated in this chapter. The size of the plateaus ΔE_p is around the size of the plateau in the medulloblastoma case. We also investigate the influence of the slope in the plateau on the discretization requirement. For that purpose slope 0 (a flat plateau), 1 (a plateau which

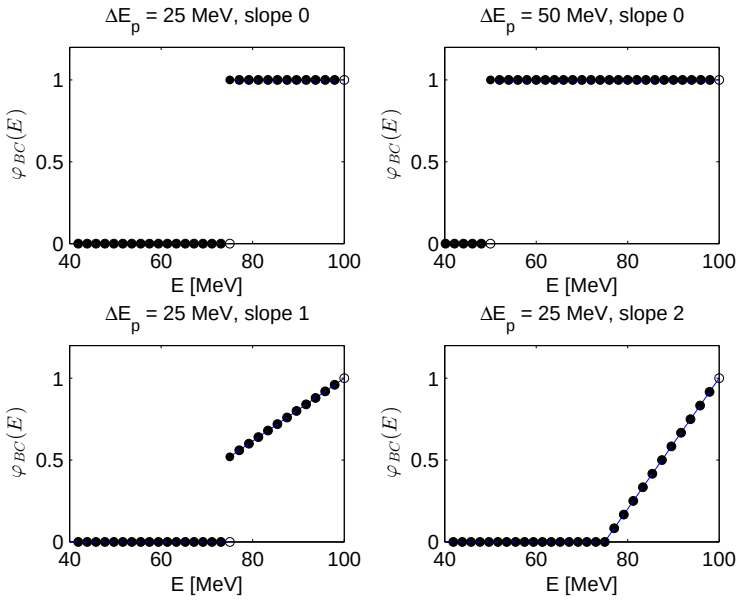

Figure 6.1: *The energy plateau boundary conditions used in test case A in the investigation of the discretization requirement for the energy variable. Here, $E_{max} = 100$ MeV.*

goes half way to zero) and 2 (a plateau which goes to zero) are defined. The calculations are performed with varying inlet energies. E_{in} refers to the energy of the mono-energetic boundary condition. E_{max} refers to the maximum energy of the energy plateau boundary condition.

6.1.3 Structure of the Discretization

Unless stated otherwise, the cells in the spatial and the energy domain in the test calculations are all uniformly distributed over the problem range. The size of the spatial range is taken just over the range of the proton through the material, see figure D.5 (right). In section 6.3.1 is investigated if adopting a different structure in the energy domain enables us to obtain results more efficiently. In this thesis the optimal structure for the spatial cells is not investigated.

The discrete ordinates are not uniformly distributed over the problem range, but are distributed as described in section 4.1. Several quadrature sets (see table 6.4) are used to investigate the discretization requirement of the angular variable. In order to be able to compare the results of calculations with different quadrature sets, we only want the discretization to be different in these calculations, not the boundary conditions. Therefore, we want the direction of the particles streaming into the problem domain to be equal in every calculation. To accomplish this, the directional cosine μ_N of the ordinate in which the particles stream into the problem domain must be fixed for every set: $\mu_N = 0.999995$ ($w_N^a = 10^{-5}$). This value is semi-arbitrarily chosen such that it is very close to $\mu = 1$ to approximate the pencil beam direction and that the majority of the remaining ordinates are in the region of interest: $0.98 < \mu < 1$. In order to validate this pencil beam direction approximation, we want to quantify the error due to this approximation. This is done by performing calculations using the setting of test case A with the quadrature sets: (i) N = 1, $\mu_N = 1$, $w_N = 4\pi$, and (ii) N =1, $\mu_N = 0.999995$, $w_N = 4\pi$. The results of calculations with quadrature set (i) are used as a reference solution (in the error equation of test case A) to evaluate the error due to the pencil beam approximation in quadrature set (ii). The result is that the error is approximately $\epsilon \approx 10^{-11}$. This is much smaller than the error which we allow into the system due to discretization, and from this result can

be concluded that the directional cosine $\mu_N = 0.999995$ close enough to 1 to accurately approximate the pencil beam direction.

6.2 Spatial Discretization

6.2.1 Test Case A

Computational Set-up

The requirement for the spatial discretization is determined by the most strict discretization requirement of test cases A and B. We start with case A. In this test case, we consider the spatial variable x and the energy variable E, and we ignore the operators which depend on the angular variable μ. Therefore, it is sufficient to consider just a single ordinate in the quadrature set: N = 1, $\mu_N = 1$ with $w_N = 4\pi$. In the energy range, we use a fixed number of 1000 energy groups. As we will see in the following section, this meets the error criterion in equation 6.1 for the energy variable. In the reference case, we use 100000 spatial cells. In these calculations, we distinguish two different types of boundary conditions: the mono-energetic boundary condition and the energy plateau boundary condition.

Results of the Mono-Energetic Boundary Condition Problem

The result for $E_{in} = 100$ MeV is shown in 6.2 (left), the results of $E_{in} = 150$ MeV and $E_{in} = 200$ MeV can be found in appendix D. As we can see from these figures, the error decreases with an increasing number of cells with approximately 2^{nd} order. If a more advanced discretization scheme would have been used here, we would expect this order to be higher, and the number of cells needed to produce accurate results to be lower. To meet the error criterion in equation 6.1, approximately 2000 spatial cells cm^{-1} are necessary. A total of 10000 cells uniformly distributed over the spatial range is sufficient to meet the error criterion for all values of E_{in}, if the spatial range is set not much larger than the range of the protons through the material (else, part of the spatial cells do not contribute to the solution, reducing the number of effective spatial cells).

Results of the Plateau Boundary Condition Problem

The same analysis is applied with a plateau boundary condition. The result for $E_{max} = 100$ MeV is shown in 6.2 (left), the results of $E_{max} = 150$ MeV and $E_{max} = 200$ MeV can be found in appendix D. We see that the number of spatial cells needed to meet the error criterion is approximately a factor of 5 - 10 smaller as compared to the mono-energetic boundary condition problem. With an increasing size of the energy plateau ΔE_p, a decreasing number of spatial cells are necessary to produce accurate results. The error decreases approximately 2^{nd} order, which is small compared to more advanced discretization schemes. The number of spatial cells to produce accurate results is expected to be lower if a more advanced discretization scheme would have been used here.

So concluding, the size of the energy depending differential flux influences the number of cells in the spatial domain necessary to meet the error criterion; with an increasing sharpness of the energy depending differential flux at the boundary, an increasing number of spatial cells are necessary in the spatial domain to produce accurate results.

6.2.2 Test Case B

Computational Set-up

In the transport equation in test case B, the angular variable μ and the spatial variable x are considered, and we ignore operators which depend on the energy variable E. Therefore, it is sufficient to include just a single energy group in the calculation. In the angular domain, just as in the benchmark cases and in the medulloblastoma case in the next chapter, we use an S_{40} quadrature set. In the reference solution, we use 100000 spatial cells.

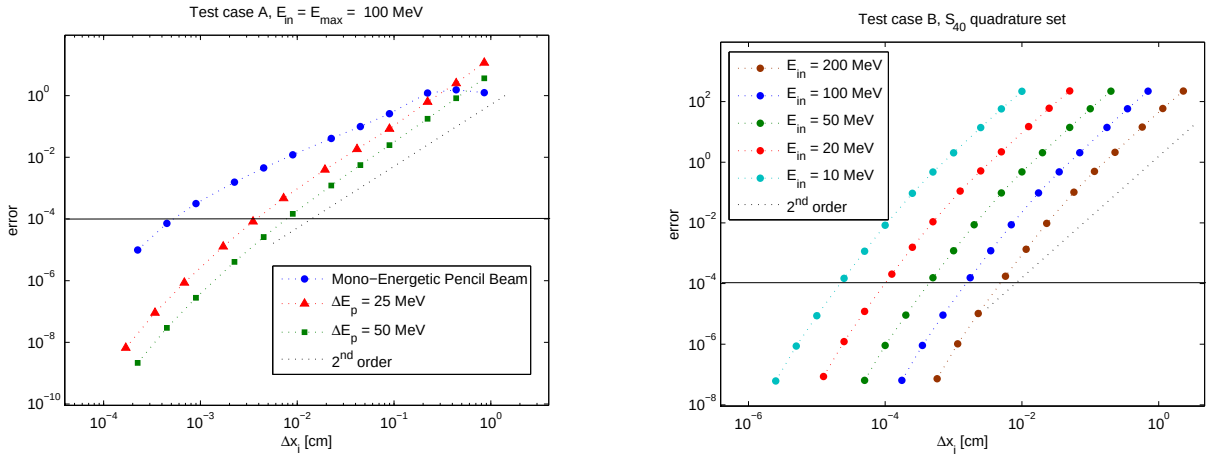

Figure 6.2: *Left: test case A, error versus width of spatial cell Δx_i for plateau and mono-energetic boundary conditions. Right: test case B, error versus width of spatial cell Δx_i with an S_{40} quadrature set.*

Table 6.3: *Momentum transfer cross section $\sigma_{tr}(E)$ of protons in PMMA with energy E_{in} for test cases B and C and the corresponding range of the protons with through PMMA for test case B.*

Material	E_{in} [MeV]	$\sigma_{tr}(E_{in})$ [cm^{-1}]	range [cm]
PMMA	200	$7 \cdot 10^{-5}$	23
PMMA	100	$2 \cdot 10^{-4}$	7
PMMA	50	$7 \cdot 10^{-4}$	2
PMMA	20	$4 \cdot 10^{-3}$	0.3
PMMA	10	$1.5 \cdot 10^{-2}$	0.1

The transport equation in test case B does not contain operators which remove particles from the equation, such as the total removal operator or the continuous slowing down operator. As a consequence, in this problem no particles are removed from the equation and the range over which the particles penetrate the spatial domain is infinite. Therefore, in test case B, we have to impose a range over which we investigate the error in a solution. This range is set equal to the range which the protons would have had if the continuous slowing down term and the total removal operator would have been included. This range is investigated with the help of test case A. The results are shown in figure D.5 in the appendix of this thesis. The error in the solution of test case B is evaluated over the range which corresponds with E_{in} in this figure.

In this test case, the protons do not lose energy as they penetrate the material. As a consequence, the energy of the protons equals their inlet energy E_{in} everywhere in the slab. The value of the momentum transfer cross section $\sigma_{tr}(E)$ depends on the material and on the energy of the proton. Since both are constant everywhere in the slab, the momentum transfer cross section is also constant everywhere in the slab: $\sigma_{tr}(E_{in})$. See table 6.3 for the values of the momentum transfer cross section in this test case.

Results

The results are plotted in figure 6.2 (right). From this figure, the error decreases with an increasing number of spatial cells with approximately 3^{rd} order. For high values of $\sigma_{tr}(E)$, we need a more dense structure to converge the solution compared to low values of $\sigma_{tr}(E)$. The discretization requirement depends on what size of effects it is desirable to capture in the calculation. If the energy of the proton is small, the remaining range of that

proton is small, but it will start to deviate from its direction of movement strongly in this remaining range. To capture this small-sized large-angular effect, a more dense spatial cell structure is necessary at the end of the range of the proton compared to the density of the structure to capture the small-angular effects at the beginning of the range. Therefore the spatial discretization in the medulloblastoma case in the following chapter is increased in the tumor, where the energy of the particles is low compared to in front of the tumor. In the remainder of this chapter all calculations are performed using 10000 spatial cells uniformly distributed over the spatial range, due to computation time considerations.

6.3 Energy Discretization

6.3.1 Test Case A

Computational Set-up

The discretization requirement of the energy variable E is determined by the most strict discretization requirement of test cases A and C. In test case A, the transport equation contains two independent variables: the spatial variable x and the energy variable E, and we ignore operators which depend on the angular variable μ. Therefore, it is sufficient to consider a single ordinate in the quadrature set: N = 1, $\mu_N = 1$ and $w_N = 4\pi$. In the spatial domain we use a fixed number of 10000. In the reference case we use 10000 energy groups. Just as in the previous section, we distinguish two types of boundary conditions: the mono-energetic boundary condition, and the energy plateau boundary condition. The plateau boundary condition can easily be set up using the multi-group method. The mono-energetic boundary condition, on the other hand, is not that easy to approximate using the multi-group method. In the next section, we present two energy group structures which can be used to approximate the mono-energetic boundary condition.

Computational Set-up of the Mono-Energetic Boundary Condition Problem

Since we are using a multi-group method, we can only approximate the mono-energetic boundary condition by introducing protons in energy group with a width ΔE_1. To investigate the optimal mono-energetic boundary condition approximation, we investigate two types of energy structures, (i) and (ii):
(i) we choose a very small value of ΔE_1 (the energy group in which the protons stream into the problem domain), after which the following energy groups are uniformly distributed over the remaining energy range. The energy group boundaries are determined according to the following three equations:

$$\Delta E_1 = 10^{-10} \tag{6.2}$$

$$E_{\frac{1}{2}} = E_{in} + \frac{1}{2}\Delta E_1 \tag{6.3}$$

$$\Delta E_{g\neq 1} = \frac{E_{\frac{3}{2}} - E_{NG+\frac{1}{2}}}{NG}. \tag{6.4}$$

The first, very small, energy group is placed symmetrically over the inlet energy E_{in}. Equation 6.4 distributes the remaining energy groups $g > 1$ uniformly over the remaining energy range. The disadvantage of this boundary condition is that the energy widths of the first and second energy groups are very different, which may cause inaccuracy in the solution.
(ii) we distribute all the energy groups uniformly over the problem domain. The energy

group boundaries in this case are determined according to the following three equations:

$$\Delta E_g = \frac{E_{\frac{1}{2}} - E_{NG+\frac{1}{2}}}{NG} \tag{6.5}$$

$$\varphi_{BC} = \frac{1}{w_N \Delta E_1}. \tag{6.6}$$

$$E_{in} = \mu_N \varphi_{BC} w_N \frac{1}{2} \left(E_{\frac{1}{2}}^2 - E_{\frac{3}{2}}^2 \right). \tag{6.7}$$

In equation 6.5 the energy boundaries are uniformly distributed over the energy range, equation 6.6 acquires that the number of particles streaming into the problem range is equal for every choice of ΔE_1 and thus for every choice of NG, and equation 6.7 acquires the energy E_{in} streaming into the problem domain is equal for every choice of NG. This last mentioned expression was obtained in the previous chapter, by evaluation of equation 5.9. The disadvantage of this boundary condition is that, although the number of particles and the average inlet energy of the particles streaming into the problem domain at the boundary is equal in every calculation, the boundary condition changes since ΔE_1 changes in every calculation. This is undesirable since we do not want the boundary condition to be dependent on the level of discretization we use, but only on the problem we are simulating.

Results of the Mono-Energetic Boundary Condition Problem

The results are plotted in figure D.4 (left) in the appendix of this thesis. From this figure, we see that the difference in the error is very small for the two different boundary conditions. So, it does not really matter which of the boundary conditions ((i) or (ii)) is used to approximate the mono-energetic boundary condition. However, (i) is gives slightly better results and is therefore adopted as mono-energetic boundary condition in the remainder of this thesis. From figure 6.4 (left), the error decreases with an increasing number of energy groups with an order of approximately 5.5. Note that this is 3.5 orders higher than the order in which the error decreases in the spatial domain, where a simple discretization scheme is used. In the low energy domain, we need a more dense energy structure to obtain an accurate solution. In every calculation 500 energy groups is sufficient to meet the error criterion, independent of E_{in}.

Results of the Plateau Boundary Condition Problem

The same analysis is applied on problems with the energy plateau boundary condition. In figure 6.4 (left) the results are shown with energy $E_{max} = 100$ MeV. The results of the $E_{max} = 150$ MeV and $E_{max} = 200$ MeV calculations can be found in appendix D of this thesis. We see that the number of cells we need to obtain a converged solution is about 5 - 10 times smaller (i.e. around 50 - 100) compared to the number of energy groups we need with the mono-energetic boundary condition. The reason for this is depicted in figure 6.3: the more singular the shape of the energy depending differential flux, the more energy groups are needed to accurately represent the shape of that flux. Since the shape of the energy depending differential flux in the mono-energetic boundary condition problem is much more singular compared to the energy depending flux of the energy plateau boundary condition problem, we can approximate the flux in the energy plateau boundary condition problem with less energy groups. Also, with an increasing width of the energy plateau boundary condition ΔE_p the shape of the smoothness of the energy depending differential flux increases and a decreasing number of energy groups are necessary here produce accurate results.

The error decreases approximately with an order of 5.5, which is equal to the order in which the error in the mono-energetic boundary condition problem decreases. Just as in the spatial discretization, we need a more dense group structure in the low energy domain to produce accurate results. The total number of groups sufficient to meet the

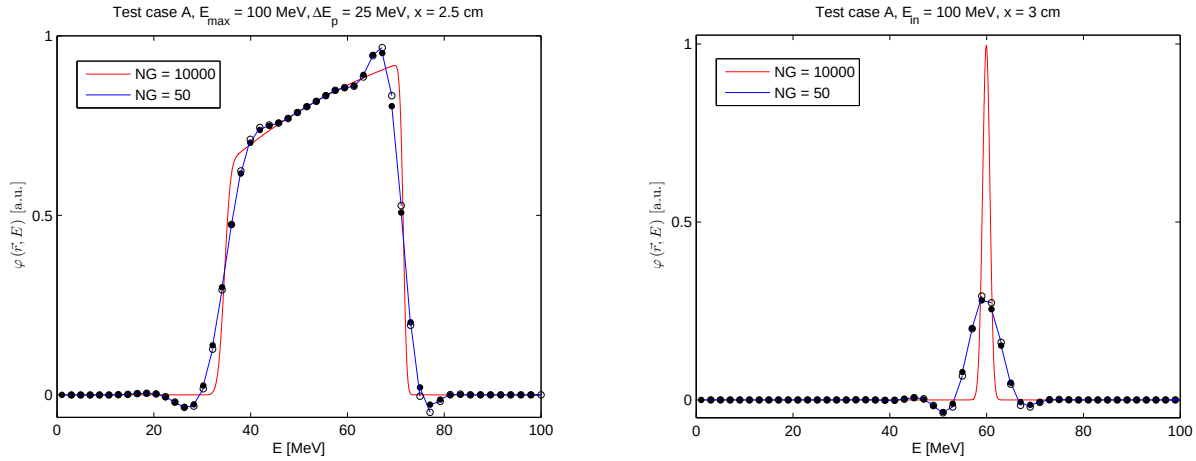

Figure 6.3: *Left: energy depending differential flux of an energy plateau boundary condition problem. Right: energy depending differential flux of a mono-energetic boundary condition problem. The 50 group energy structure is more suited to approximate the energy depending differential flux on the left compared to the right.*

error criterion is approximately 100 and 50 for $\Delta E_p = 25$ MeV and $\Delta E_p = 50$ MeV respectively, independent of E_{max}, see figures 6.4 (left) and D.2.

The influence of the slope of the plateau on the discretization requirement is tested. The results are shown in figure D.3 (left), in the appendix of this thesis. From this figure, the slope of the plateau does not influence the discretization requirement (significantly). Therefore, we assume that only the size of the energy plateau ΔE_p is on influence on the discretization requirement, not the shape of the plateau.

Investigation of the Optimal Energy Group Structure

In the previous sections, we have seen that we need a more dense energy group distribution in order to produce accurate results in the low energy range compared to the high energy range. This raises the suspicion that we could obtain an accurate solution more efficiently by applying a different energy group structure than the uniform distributed energy group structure. To investigate this, we introduce a method to distribute the energy groups which is similar to the distribution of ordinates in the quadrature set we introduced in section 4.1: we start with an energy group with a certain width, after which the following energy groups have widths which are a factor larger than the previous energy group: $\Delta E_g = f \cdot \Delta E_{g+1}$. In this section, we investigate the influence of f on the error in the solution.

From this investigation we found that in some cases we can obtain a more accurate solution with the same number of groups for certain values of f, but the gain is rather small. The result of a case in which we can obtain a very small decrease in error is shown in figure D.3 (right), in the appendix of this thesis. In most of the cases, however, in both the energy plateau and the mono-energetic boundary condition problems, we found that the best energy structure was the uniform distributed group structure. This is probably due to the range of the protons through the material after an error is created: if the error is created in the high energy range, the proton carries this error over a large range through the slab and has relative large effects on the solution. Errors created in the low energy range are carried over a short range through the slab, and therefore have a relative small effect on the solution. So, refining the group structure in the low energy range at the expense of the high energy range does not decrease the error in the solution (significantly). In all following calculations a uniform distributed energy groups structure is used.

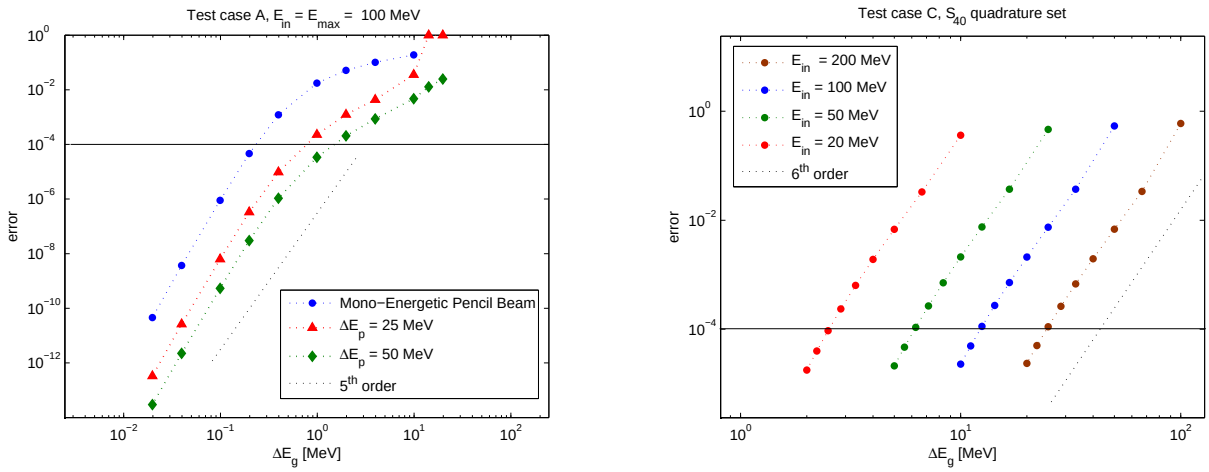

Figure 6.4: *Left: test case A, error versus energy width ΔE_g. Right: test case C, error versus energy width ΔE_g.*

6.3.2 Test Case C

Computational Set-up

In this thesis, the values of the momentum transport cross section $\sigma_{tr}(E)$ are evaluated at the center of the energy group ($\sigma_{tr,g} = \sigma_{tr}(E_g)$). In this section, this method of representing $\sigma_{tr}(E)$ is tested with the help of test case C. The transport equation in this test case contains the energy variable E and the angular variable μ. In the angular domain, we use an S_{40} quadrature set as defined in table 6.4, and in the reference solution, we use 1000 energy groups. Since there is no dependence on the spatial variable x in this transport equation, it is sufficient to consider only one spatial cell. Since the transport equation does not contain the streaming operator ($L_{str} = \mu\frac{\partial}{\partial x}$), we cannot impose a boundary condition as we did in the previous test cases. Therefore, in this test case the boundary condition is imposed on the continuous slowing down operator ($L_{CSD} = \frac{\partial S(E)}{\partial E}$) by fixing $\varphi(E_{\frac{1}{2}}) = \varphi_{BC}$.

Results

From figure 6.4 (right), we see that the error in the test case decreases 6^{th} order, with an increasing number of energy groups. An example of a 100 MeV calculation is plotted in figure D.4 (right) in the appendix of this thesis. The discretization requirement depends on what size of angular effects is desirable to capture in a simulation. We assume it is not useful to capture the angular deviation of protons with a range less than 0.3 cm, which corresponds to an energy of approximately 20 MeV (see figure D.5). To capture the angular effects of the protons with energies $E \geq 20$ MeV, the discretization requirement of the energy variable in this test case does not exceed the discretization requirement in test case A, independent of the type of boundary condition (plateau or mono-energetic). So, in conclusion, the method we have used here to represent $\sigma_{tr}(E)$ ($\sigma_{tr,g} = \sigma_{tr}(E_g)$), does not need to be improved.

6.4 Angular Discretization

6.4.1 Test Case B

Computational Set-up

The requirement for the angular discretization is investigated by means of test case B. The transport equation in this test case contains the angular variable μ and a spatial

Table 6.4: *The quadrature sets used in test case B and the approximate computation time to obtain a solution.* f *in* $w_n = f \cdot w_{n+1}$. $\mu_N = 0.999995$ *and* $w_N^a = 10^{-5}$.

Quadrature	f	CPU time [a.u.]
S_{10}	3.75	1
S_{20}	1.82	3
S_{40}	1.32	9
S_{80}	1.14	40
S_{150}	1.063	100
S_{250}	1.036	300
S_{400}	1.021	700
S_{500}	1.016	1300

variable x, and we ignore operator which depend on the energy variable E. Therefore, it is sufficient to consider a single energy group. In the reference case, we use an S_{500} quadrature set. In the spatial domain we use 10000 cells in every calculation. See table 6.4 for the quadratures sets used in this investigation. No operators which remove particles from the equation are included in the transport equation, and as a consequence, we have to impose a range over which we investigate the error (see section 6.2.2). See table 6.3 for the values of the momentum transfer cross section $\sigma_{tr}(E)$, and the ranges which are used in the calculations.

Results

Figure 6.5 (left), shows the angular depending differential flux at the end of the range in a calculation performed with a 100 MeV boundary condition. The result of a calculation with a 10 MeV boundary condition is shown in figure D.5 (left) in the appendix of this thesis. From these figures we see, that if a low order quadrature set is used, the flux is overestimated near $\mu = 1$. Further away from $\mu = 1$, the error in angular flux decreases strongly. Note that the computation time increases strongly with an increasing degree of quadrature, see table 6.4. This due to the increased number of equations in the set, and the increased number of iterations necessary to obtain the converged solution. In future work, much computation time can be gained if this iteration process is accelerated. For example, it can be investigated if a multi-grid method is suited to decrease computation time. In this multi-grid method, first a relatively low order quadrature is used to evaluate the angular flux. In this first solution, the flux is well approximated far from $\mu = 1$ and less near $\mu = 1$. The quadrature is then refined and interpolation is used for the flux values in the new ordinates. This fine quadrature is used to refine the angular flux away from $\mu = 1$ and improve the angular flux near $\mu = 1$.

From figure 6.5 (right), we see that the error decreases 4^{th} order. The error is in approximation independent of the inlet energy E_{in}. To obtain an error which meets the criterion we would need an S_{80} quadrature set. However, due to computation time considerations, we choose to use the S_{40} quadrature set in the benchmark calculations and to accept the error $\epsilon \approx 10^{-3}$ in the angular solution.

6.4.2 Test Case C

Test case C is not included in the investigation of the angular discretization requirement.

6.5 Conclusions

The error due to discretization is allowed to be $\epsilon \leq 10^{-4}$. To meet this criterion, a typical mono-energetic boundary condition problem needs 500 energy groups, 10000 spatial cells and an S_{80} quadrature set. The number of unknowns in such a calculation is: $2\times\text{NG}\times\text{NE}\times\text{N} = 2\times500\times10000\times80 = 8\cdot10^8$.

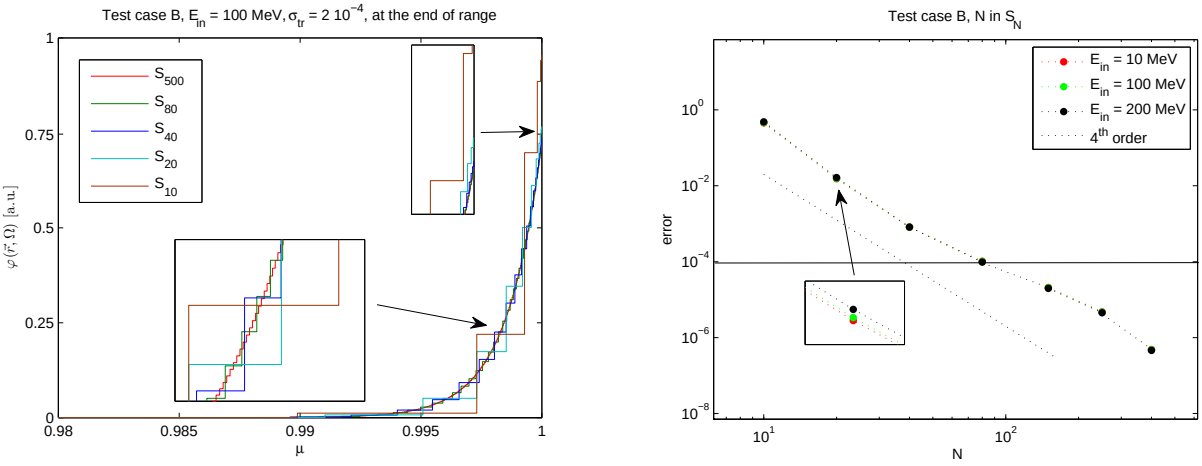

Figure 6.5: *Left: test case B, the angular depending differential flux at the end of the range, $E_{in} = 100$ MeV. Right: test case B, the error versus the number of ordinates N in the quadrature set.*

In a typical energy plateau boundary condition problem, the number of unknowns is, depending on the width of the plateau, approximately 2×NG×NE×N = 2×75×2500×80= $3{\cdot}10^7$. The total number of unknowns (and thereby also computation time) is approximately a factor of 25 smaller compared to the mono-energetic boundary condition problem (in a 3D calculation, this factor will even be orders larger). So concluding, due to computation time and storage space considerations, the S_N method is more suitable for solving energy plateau boundary condition problems compared to mono-energetic boundary condition problems.

Investigation showed that the optimal energy structure is the uniform energy structure in most cases. In some cases, solutions can be obtained more efficiently by applying a different structure, but the gain is not significant.

The number of cells necessary to produce accurate results decreases with an increasing size of the plateau. The slope of the plateau does not influence the discretization requirement.

The mono-energetic boundary condition is best approximated with a very small first energy group, for example, $\Delta E_{g=1} = 10^{-10}$ MeV. To approximate the pencil beam boundary condition, the directional cosine of this ordinate $\hat{\Omega}_N$ was chosen to be $\mu_N = 0.999995$. The error due to this pencil beam approximation is $\epsilon \approx 10^{-11}$, which is very small compared to the error which we allow due to discretization ($\epsilon \leq 10^{-4}$). So, this is a good approximation of the pencil beam direction.

The multi-group momentum transfer cross sections are evaluated as ($\sigma_{tr,g} = \sigma_{tr}(E_g)$), which does not need improving.

The number of iterations necessary to converge the continuous scatter operator increases strongly with an increasing size of the quadrature set. A lot of computation time can be gained by accelerating this iteration process.

The energy straggling operator can be ignored for the purpose of proton transport calculations in the energy range considered in proton therapy (see appendix C).

7. Results

7.1 Benchmark Cases

The results of the previous chapters are used in this chapter to set up two benchmark calculations. The results of these calculations are compared to the results of Monte Carlo calculations of the same problem. The Monte Carlo method is known to be very accurate, and therefore, these Monte Carlo calcualtions are assumed to be equally valuable as a benchmark as experimental results would have been. The results of these calculations are provided by Aleksandra Biegun [3], a post-doctoral researcher at the Technical University Delft.

7.1.1 Computational Set-up

Geometry and Material

The Monte Carlo calculations are of a mono-energetic pencil beam problem on a slab of PMMA. These calculation are performed in a 3D geometry. In this thesis, we only considered the 1D transport equation, and so, we are only able to perform calculations on 1D geometries. Still, we expect the solution of the Monte Carlo calculation to be comparable because of the nature of interaction of the protons with matter: they tend to go in a straight line through the material and they have small angle scatter interactions. These properties make the problem more depending on the x-coordinate, and less on the y and z coordinates. The 1D pencil beam problem can be visualized in 3D as the uniform irradiation of an infinite large slab, see figure 3.7 (left). On the right of this figure is the 3D pencil-beam problem visualized. In both cases, we expect the depth of the Bragg peak to be at the some depth in the slab. The dose profile from the Monte Carlo calculation is obtained by integrating the dose over the y and z coordinate. In this way, we have equal units of dose in both cases. We are not able to compare the angular solution; to be able to compare the angular solution of our method to the results of the Monte Carlo method, we need to perform calculations in a 3D geometry.

Boundary Condition

The benchmark cases are mono-energetic pencil beam boundary condition problems. From section 6.3.1, we have concluded that the best mono-energetic boundary condition approximation is boundary condition (i) from this section. Therefore, this boundary condition is used in these benchmark cases as well. The particles in the pencil beam stream into the problem domain perpendicular to the surface of the slab ($\mu = 1$). This is approximated by imposing a boundary condition on the first spatial element ($i = 1$), on discrete ordinate $\hat{\Omega}_N$, in the streaming operator ($L_{str} = \mu \frac{\partial}{\partial x}$).

Discretization

The level of discretization we use depends on the error which we allow in the calculation due to discretization. The error criterion in this thesis is semi-arbitrarily chosen, based on inspection of results of a 100 MeV mono-energetic pencil beam calculation from test case A of the previous section, see figure 7.1 (left). We decided that error in the NG = 500 calculation in this figure, is acceptable for the purposes of proton therapy. The difference in the peak position from the reference case is here $4.5 \cdot 10^{-3}$ cm, and the overshoot at

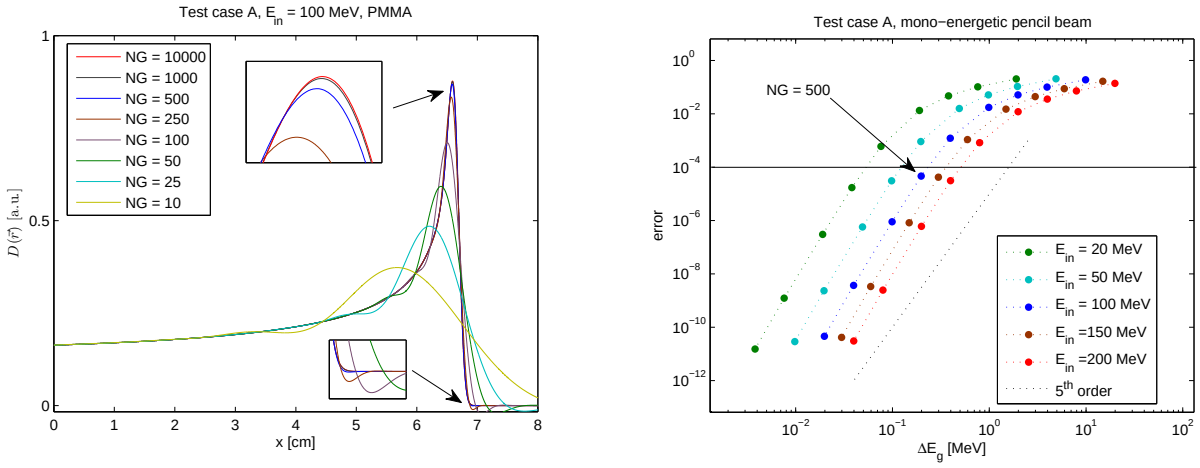

Figure 7.1: *Left: test case A (see table 6.1), dose profile of a mono-energetic pencil beam boundary condition problem. Right: the error we allow in the calculation is the error in the 500 energy group case which corresponds to* $\epsilon \leq 10^{-4}$.

Table 7.1: *Computational set-up of the benchmark cases.*

										fraction % by weight			
Material	E_{in} [MeV]	NG	N	NE	L	$S(E_{g\pm\frac{1}{2}})$	$\sigma_{tr}(E_g)$	$\sigma_{C,g}$	$\sigma_{C,g'\to g,l}$	H	C	O	ρ $[\frac{g}{cm^3}]$
PMMA	100,200	500	40	10000	10	Eq. 3.28	Eq. 3.19	SADCO	SADCO	0.08	0.6	0.32	1.18

the edge of the Bragg peak is acceptable. From figure 7.1 we see that this corresponds with $\epsilon \approx 10^{-4}$. So, discretization level in calculations performed in this thesis, is required to meet the error criterion $\epsilon \leq 10^{-4}$. In table 7.1, the settings are listed which we used to set up the benchmark cases. Note that the S_{40} quadrature set is used (see table 6.4), which does not meet this error criterion. Due to computation time considerations, the error $\epsilon \approx 10^{-3}$ is accepted in the angular domain. The energy straggling operator is not included in the calculations, due to its large influence on the computation time, and the small influence on the solution, see appendix C.

7.1.2 Results

In figure 7.2 (left), the dose deposition result of the 100 MeV benchmark calculation is presented. Here we see that the shape and the position of the peak are similar in both calculations. The S_N method does suffer from a small overshoot at the edge of the Bragg peak.

In figure 7.3 (left) we see the angular depending differential flux at various positions in the slab. The further the protons penetrate into the material, the further the protons deviate from their original path of direction. This deviation is the strongest in the last part of the protons range, as we can see from the difference in value of the angular depending differential flux between $x = 6$ and $x = 6.5$ cm. However, this part of the solution cannot be compared to the 3D Monte Carlo calculation.

In figure 7.2 (right), the dose deposition result of the 200 MeV benchmark calculations is presented. The profiles are similar in this case as well, although we do see two clear differences. The first is at the beginning of the dose profile. Here, the Monte Carlo simulation shows a smaller dose than our calculation with the S_N method. This difference in dose profile is probably the energy transferred to secondary particles which are not included in our calculations, like neutrons and photons. The energy which would have been carried and deposited over a relatively large range by to these particles, is assumed

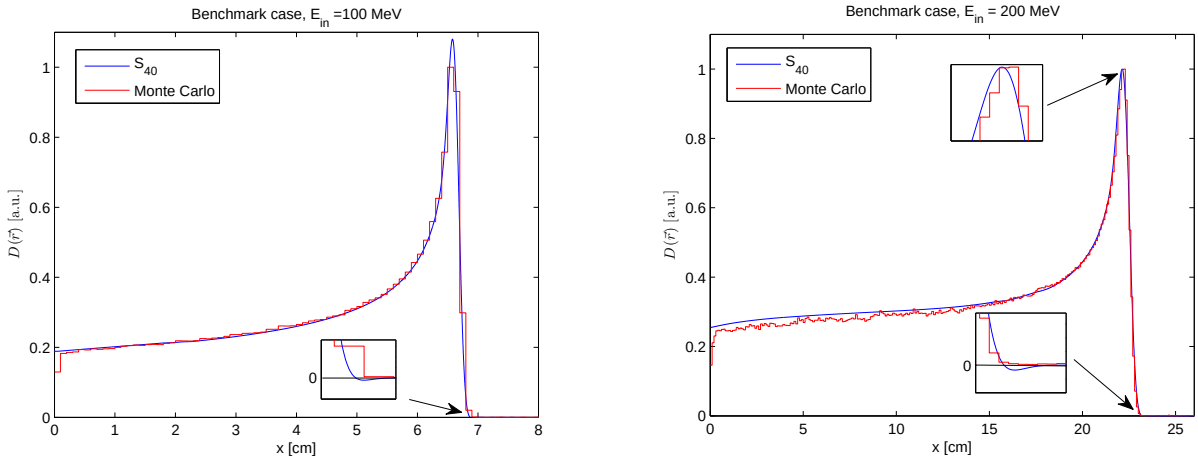

Figure 7.2: *Left: 100 MeV benchmark calculation, dose distribution. Right: 200 MeV benchmark calculation, dose distribution.*

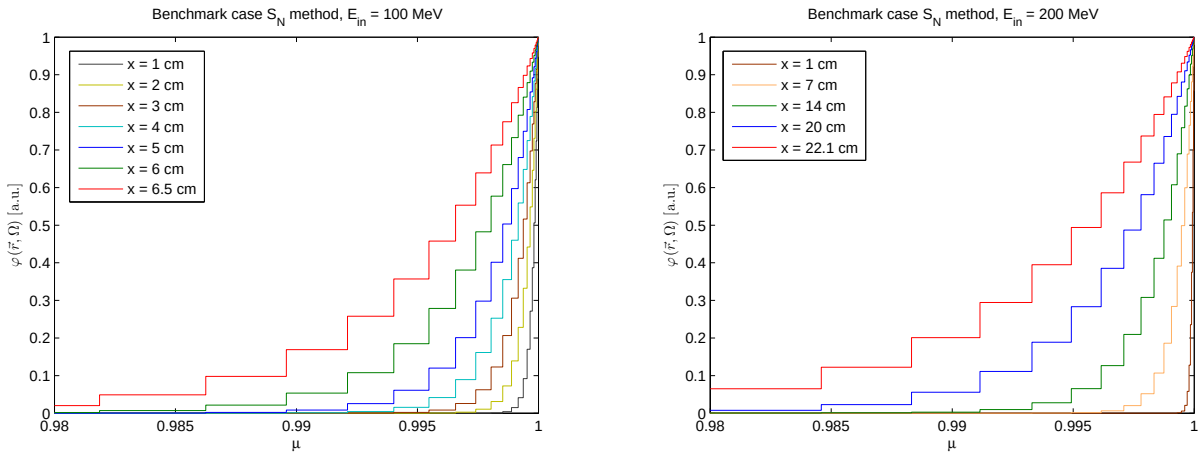

Figure 7.3: *Left: 100 MeV benchmark calculation, angular depending differential flux. Right: 200 MeV benchmark calculation, angular depending differential flux.*

to be deposited locally in our S_N calculations. This effect is large in the high energy range, compared to the low energy range. Therefore, this effect is large in the 200 MeV case compared to the 100 MeV case. The second lies in the position of the peaks. This small difference is probably the result of two things. The first is not including the shell corrections in our model for the stopping power. This effect corrects for the requirement that the velocity of the incident proton is much larger than the velocity of the target electron, slightly reducing the magnitude of the stopping power, resulting in a slightly larger range of the protons through the material. The second is the error criterion. This criterion is based on inspection of results of a 100 MeV mono-energetic boundary condition problem calculation. This error criterion may need to be more strict for a 200 MeV boundary condition problem. If under discretization is used, the position of the Bragg peak shifts to the left, see figure 7.1.

In figure 7.3 (right) the angular depending differential flux is shown for the 200 MeV S_N calculation. Just as in the previous benchmark case, this result cannot be to compared to the Monte Carlo calculation. We do see that the angular depending differential flux is more diffused to larger angles in the 200 MeV problem compared to the 100 MeV problem, as we would expect.

In both results, the S_N method suffers from overshoots end the end of the Bragg peak. This overshoot is seen in the energy depending differential flux as well. It is a consequence of the level of discretization we used. If a higher level of discretization would have been used, these overshoot disappear. However, computation time and storage space increases.

7.2 Medulloblastoma Case

As the final part of this thesis, we propose a treatment plan for the 4-year-old medulloblastoma patient in the scan of figure 7.4 (left), calculated with the S_N method. In the T1-weighted scan, the fatty tissue appears more bright on the picture, and we can clearly recognize the tumor in the brain. A critical area of the brain of the patient is lying directly behind the tumor. Irradiation of this tumor with conventional means, like photon or electron radiation, will lead to a significant dose in this critical area of the brain. This may result in long term side effects in the development of the patient, such as problems with speech, hearing or locomotion. Using proton therapy, we can achieve maximum dose in the tumor, while sparing this critical area.

7.2.1 Computational Set-up

Geometry and Materials

Figure 7.4 shows a T1-weighted MRI scan of the patient's head. From inspection of this figure, we estimated the width of the various tissues from the entry point in the head to reach the tumor. In our 1D calculation, we can not include information on the height and the width of the materials, only the depth. Such a 1D geometry can be visualized in 3D as the uniform irradiation of an infinite-sized slab. This slab then consist of several layers, representing the different tissues in the patient, see figure 7.4 (right). The tissues which are encountered by the proton are deducted from figure 7.4: skin, bone, brain, tumor, and behind the tumor lies a critical area of the brain, see table 7.2. The chemical composition and the density of these tissues is abstracted from the work of Woodard [46]. These physical properties are used in our models to evaluate the stopping powers and the momentum transfer coefficients, and used in the SADCO code to evaluate the multi-group catastrophic scatter constants.

Discretization

The discretization is such, that we meet the error criterion established in the previous section: $\epsilon \leq 10^{-4}$, with the exception of the angular quadrature set, where we accepted the error of $\epsilon \approx 10^{-3}$ due to computation time considerations, see table 7.2 for the settings.

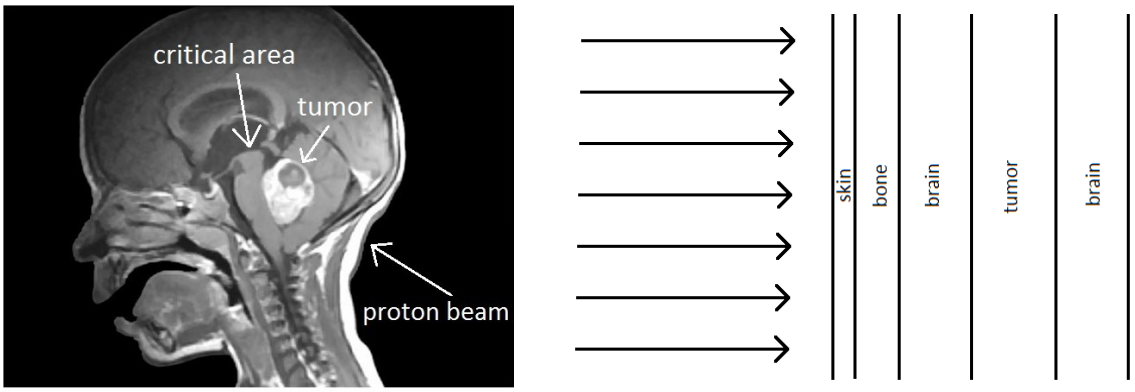

Figure 7.4: *Left: T1-weighted MRI scan, sagittal view of a medulloblastoma patient[34]. Right: the 1D geometry used in the treatment plan.*

Table 7.2: *Computational set-up of the medulloblastoma case with an S_{40} quadrature set (see table 6.4), with 100 energy groups, a P_{10} order Legendre expansion catastrophic differential scatter cross sections, and a plateau energy boundary condition $\Delta E_p = 30$ MeV, with energy depending differential flux as in figure 7.5. The multi-group stopping powers $S(E_{g\pm\frac{1}{2}})$ are evaluated with equation 3.28, the multi-group momentum transfer cross sections $\sigma_{tr,g} = \sigma_{tr}(E_g)$ are evaluated with equation 3.19, the multi-group catastrophic scatter cross sections $\sigma_{C,g}$ and $\sigma_{C,g'\to g,l}$ are evaluated with the SADCO code.*

			fraction % by weight[46]										
Body tissue	size [cm]	$\Delta x_i[cm]$	H	C	N	O	Na	P	S	Ca	Cl	K	$\rho\ [\frac{g}{cm^3}]$
Skin	0.2	10^{-2}	10	25	4.6	59.4	0.2	0.1	0.3	0	0.3	0.1	1.09
Bone	0.5	10^{-2}	3.4	11.5	4.2	43.5	0.1	0	0.3	22.5	0	0	1.85
Brain Gray	0.4	10^{-2}	10.7	9.5	1.8	76.7	0.2	0.3	0.2	0	0.3	0.3	1.04
Brain White	2.4	10^{-2}	0.6	19.4	2.5	66.1	0.2	0.3	0.2	0	0.3	0.3	1.04
Tumor	3.5	10^{-3}	0.6	19.4	2.5	66.1	0.2	0.3	0.2	0	0.3	0.3	1.2
Critical Area	2	10^{-2}	10.6	19.4	2.5	66.1	0.2	0.3	0.2	0	0.3	0.3	1.04

Just as in the benchmark cases, the energy straggling operator was not included in the calculations, since the effect of this operator on the solution is very small, see appendix C.

Boundary Condition

To approximate the pencil beam direction ($\mu = 1$) a boundary condition is imposed on the discrete ordinate $\hat{\Omega}_N$ in the streaming operator ($L_{str} = \mu\frac{\partial}{\partial x}$) in the first element on the left side of the slab ($i = 1$). The optimal energy depending differential flux of the boundary condition $\varphi_{BC}(E)$ is such that a maximum, nearly flat dose profile in the tumor is accomplished, while sparing the critical area. For this purpose, the optimal energy depending differential flux is investigated, using trial and error. The result is shown in figure 7.5. The width is $\Delta E_p = 30$ MeV, and $E_{max} = 103$ MeV.

7.2.2 Results

The dose deposition result of the medulloblastoma calculation is plotted in 7.5 (left). Near the entry point, the dose is relatively small compared to the dose in the tumor, although it is high compared to the entry dose of a single Bragg Peak. This can be explained by viewing the plateau boundary condition as a summation of a number of mono-energetic pencil beams. The Bragg peaks of these beams line up next to each other to obtain a flat dose profile in the tumor. Their entry doses, on the other hand, are added together, which result in a relatively high entry dose. The dose is maximum in the tumor, and hardly any dose is deposited in the critical area directly behind the tumor. Notice that the dose

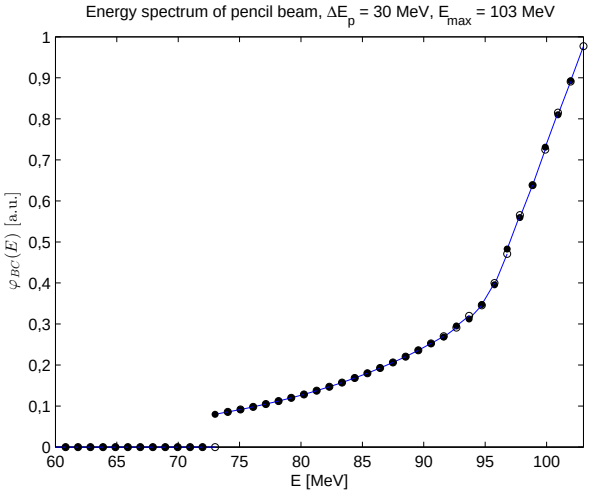

Figure 7.5: *The energy depending differential flux of the protons in the pencil beam at the boundary used in the medulloblastoma calculation.*

in the bone is smaller than the one in the surrounding tissue. This is due to the high number of the relatively heavy calcium atoms present in the scull; the amount of nucleons compared to the number of atomic electrons here, is relatively large due to the number of neutrons in the nucleus of a calcium atom, and as a consequence the deposited energy is distributed over a larger mass and so the dose is relatively low.

In this treatment plan, 62.3% of the energy is deposited in the tumor, 37.8% is deposited in front of the tumor, and only 0.7% of the dose is deposited in the critical area. If photon or electron radiation would have been used, the energy in front of the tumor and especially the energy in the critical area would be significantly higher. 96.5% of the deposited energy is transferred from the proton through inelastic Coulomb interactions with the atomic electrons. The remaining 3.5% is transferred through the catastrophic interactions of the incident protons with the atomic nuclei.

To reduce the entry dose, the tumor can be radiated from several angles. This causes the entry energy to be distributed over a larger part of the brain, locally reducing the dose in the brain. However, although the dose is lower, the total amount of normal tissue which is irradiated is larger, which may increase the chance on long term side effects instead of reducing it.

In figure 7.6 (right) the scalar flux is shown. At the beginning of the slab, the scalar flux decreases only due to absorption of protons in the catastrophic scatter process. After approximately $x = 4$ cm, the scalar flux decreases as a consequence of protons streaming out of the system through the final energy group boundary. After a little more than 7 cm, all of the protons have deposited their energy within the patient.

In figure 7.7 (left) the angular depending differential flux is plotted at several positions in the patient. The protons deviate from their original trajectory as they penetrate the patient. Due to this effect, some of the protons may pass the tumor on the side, thus contributing to the dose in normal tissue. This effects is not captured in a 1D calculation. However, since the protons tend to move in a straight line through the tissue, this effect is expected to be small. If the depth of the tumor increases, the protons can deviate further from their original trajectory, and as a consequence, the expected number of protons which miss the tumor by passing it on the side becomes larger. To capture these effects, 2D or 3D calculations are necessary.

In figure 7.7 (right) the energy depending differential flux of the protons is shown at several positions in the patient. Near the entry point, the protons have high energies. As the protons penetrate the tissue, energy is transferred to their surroundings, and the

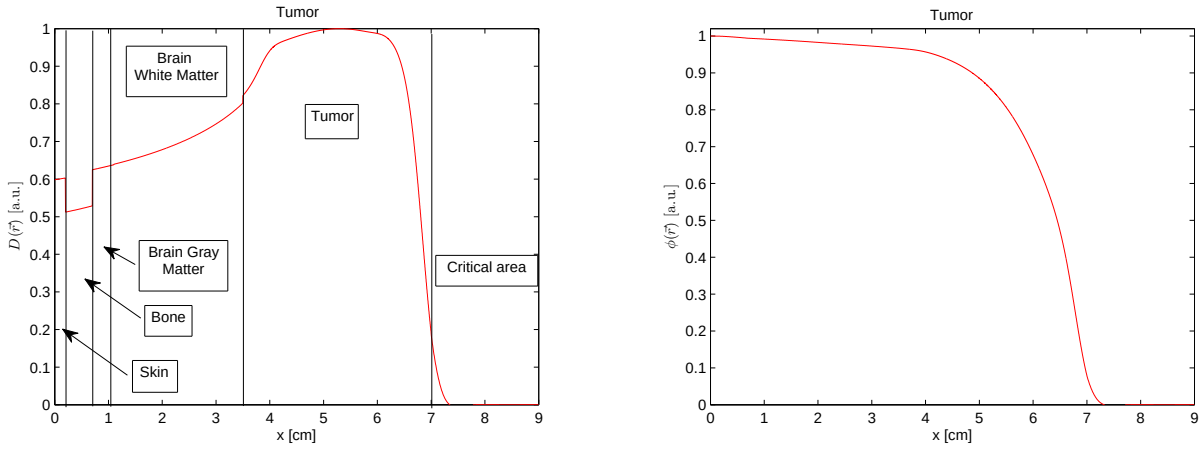

Figure 7.6: *Left: medulloblastoma case, dose distribution. Right: medulloblastoma case, scalar flux.*

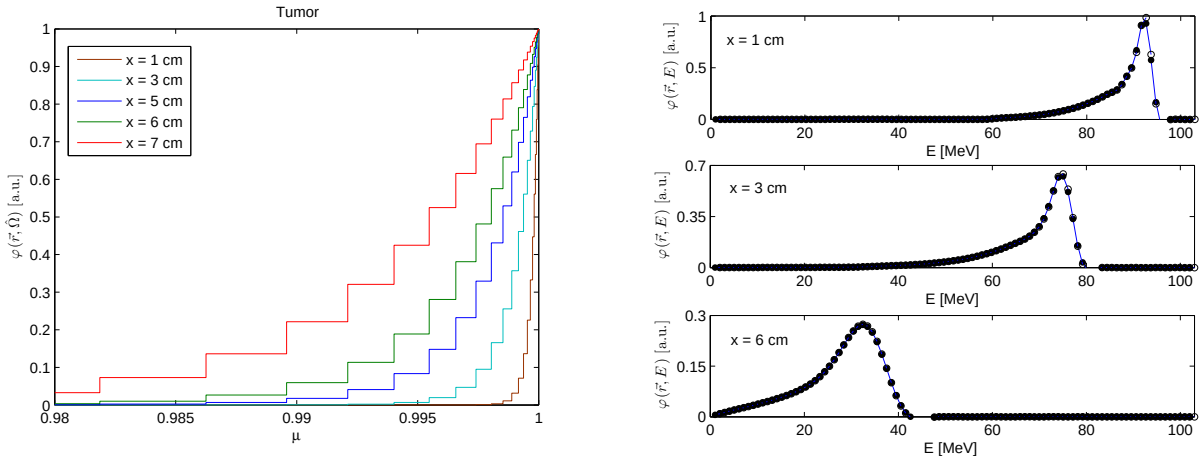

Figure 7.7: *Left: medulloblastoma case, angular depending differential flux at various positions in the patient. Right: medulloblastoma case, energy depending differential flux of the protons in bone (x = 1 cm), in the brain (x = 3 cm) and in the tumor (x = 6 cm).*

energy of the protons decrease. This is represented by the movement of the spectrum through the energy domain.

7.3 Conclusions

Results of the S_N method are compared to benchmark cases performed with the Monte Carlo code. Results are promising: the depth of the peak is very similar, and small difference in the profile between the result of the S_N method and the Monte Carlo calculations can be explained using secondary neutron dose, under discretization and shell corrections in the stopping power model. The profiles are expected to be exactly overlapping if these issues are further improved. However, the angular part of the solution is cannot be compared to benchmark cases using 1D calculations. In future work, 3D calculations should be performed in order to validate that the continuous scatter operator and the transport cross section are good representations of the angular deflection of the incident protons.

8. Discussion and Conclusions

The main goal of this thesis was to investigate the applicability of the S_N method to the use of proton therapy planning, and if it can replace and augment the Monte Carlo method. Therefore, the main question of this thesis was:

Is the S_N method accurate enough to replace the Monte Carlo method in proton therapy planning, and what underlying methods need to be improved to reach its potential computation speed?

For the purpose of answering this question, the models for describing charged particle transport and methods solving the transport equation were investigated on accuracy for proton transport calculations in the energy range considered in proton therapy. In this chapter we present and discuss the main results and conclusions of this investigation. In the following sections, we provide an answer to the main question of the thesis and give the general conclusion of this work. In the final section, we give recommendations for future work.

8.1 Models for Describing Protons Transport

The three main interaction processes in the energy range considered in proton therapy are: elastic Coulomb scatter interactions with the atomic nuclei, inelastic Coulomb scatter interactions with the atomic electrons, and catastrophic scatter interactions with the nucleus. These are the only three interaction processes needed to be modeled to accurately calculate the particle field in the problem domain in the energy range considered in proton therapy.

The Coulomb interactions are modeled by using the Rutherford model and the model of Bethe. These models are accurate down to 1 MeV in the energy range considered in proton therapy. This is an acceptable cutoff energy since the range of a 1 MeV proton through tissue is very short. Rutherford's model and the model of Bethe are used to evaluate the Fokker-Planck coefficients. Based on the comparison of the stopping power (one of the Fokker-Planck coefficients) with literature values it was concluded that our values were quite accurate, but the shell corrections need to be included in our models to highly accurate evaluate the stopping power in the energy range considered in proton therapy. The momentum transfer cross sections (one of the Fokker-Planck coefficients) was also validated using literature values and found accurate. However, 3D calculations are necessary to further validate these cross sections.

The catastrophic scatter interactions are modeled by using an extern code: the SADCO code. However, this code does not provide data in the complete energy range considered in proton therapy, and the accuracy is questionable in some parts of its outcome. In future work, an alternative code should be investigated, for example MCNPX, or it should be investigated if models are available to describe these scatter interactions.

The Fokker-Planck approximation was used to mathematically describe the small angular scatter interactions and the small energy transfers. The small energy transfers are accurately described by the continuous slowing down operator in the energy range considered in proton therapy; it is not necessary to include the energy straggling operator to

describe the process in this energy range. The small angular Coulomb scatter of the incident protons is described by the continuous scatter operator. This operator is validated in the energy range considered in proton therapy, for small angle scatter only. The large angle scatter needs to be described by the conventional Boltzmann scatter operator for an accurate and complete description of the problem. To further validate this operator for small angle Coulomb scatter, 3D calculation are necessary in future work.

8.2 Methods to Solve the Transport Equation

The linear Boltzmann-Fokker-Planck equation is the transport equation which is used to describe proton transport. In this thesis, the 1D form of this equation is transformed into a set of coupled equations using discretization methods. Subsequently, an iterative method is used to obtain the solution from this set of equations.

Several discretization methods exist for solving partial differential equations. In this thesis, the discretization methods used are the S_N method, the step scheme, and the linear discontinuous Galerkin method for the angular variable μ, the spatial variable x, and the energy variable E respectively. The S_N method and the step scheme are equivalent to each other, i.e. we would end up with the same set of equations if we had used the step scheme instead of the S_N method in the angular domain. Both these methods are relatively simple and suffer from large truncation errors: a relatively large number of discrete ordinates and spatial elements are necessary to produce accurate results. We expect these numbers to be smaller if a more advanced discretization scheme would have been used in these domains. This would decrease the number of cells necessary to produce accurate results, and thereby reduce storage space and computation time.

The energy domain is discretized using the linear discontinuous Galerkin method. This method is a more advanced method compared to the step scheme and the S_N method. It uses both features of the finite volume method and the finite element method: the energy groups are considered as a finite volume, the flux inside the groups is approximated with a finite set of basis functions. In this thesis, this flux is approximated to be linear within the groups. This linear dependency is expressed with a set of two basis functions which results in a coupled set of average and slope equations. It is possible to approximate the flux within an energy group using more basis functions. The number of equations and unknowns per energy group increases with the number of basis functions. However, we expect a fewer number of energy groups to be necessary to produce accurate results. Therefore, using more basis functions may reduce the number of equations and unknowns in the set and thereby reduce computation time. In future work, it should be investigated what the optimal number of basis function is in the discretization in the energy domain, spatial and angular domain in order produce accurate results as efficiently as possible.

The Gauss Seidel iterative method is used to solve the set of coupled equations. The average and slope equations are solved together, since they are strongly coupled, and are used as the basic building block in solving the set of equations. It is also possible to include more equations in the basic building block, for example, the average and slope equation of two neighbor spatial elements. Even though it will cost more computation time to solve this larger matrix system, the solution is expected to converge faster, and it may thus reduce the overall computation time in this case. In future work, it should be investigated what the optimal set of equations is in the basic building block for solving the system as efficiently as possible.

The convergence of the continuous scatter operator during the iterative process is slow; the angular depending differential flux moves, during the iterations, very slowly in the direction of the converged solution. On the other hand, if a low order quadrature set is used, the angular depending differential flux moves more quickly to the converged solution. Therefore, we expect that higher computation speed can be reached by using a multi-grid method. In this method, the order of the quadrature changes during the

iterations, using interpolation to estimate to angular depending differential flux of the higher order quadratures. In future work, it should be investigated what the optimal method is to accelerate this convergence process.

8.3 Main Question of the Thesis

The previously discussed investigations were undertaken to test the applicability of the S_N method to proton therapy planning, and to answer the main question of the thesis.

The results of the investigations were used to set up two benchmark calculations of a 100 MeV and a 200 MeV mono-energetic pencil beam boundary condition problems. The results of Monte Carlo calculations were used to benchmark our calculations with the S_N method. Monte Carlo is proven to be very accurate, and therefore we assume it to be a valuable benchmark.

The results were promising: in the 100 MeV benchmark case the Bragg peaks were at the same position and the dose profiles were almost exactly overlapping. In the 200 MeV benchmark case the Bragg peaks were almost at the same position; the small difference is expected to be due to the following: under discretization (the discretization criterion we used was based upon a 100 MeV case, the 200 MeV case may need a more strict criterion), or to the shell correction, which is not included in our model for the stopping power. The base of the profile is slightly different from the Monte Carlo calculation. This is expected to be due to the neglect of secondary neutrons: these secondary neutrons carry this energy over a large range. In the S_N calculation, they are assumed to deposit their energy locally. In conclusion, if these small shortcomings are overcome, the dose profiles are expected to be exactly overlapping. In other words, the S_N appears to be just as accurate as the Monte Carlo method. However, the angular solution cannot be benchmarked using 1D calculations. So, in order to answer this part of the question, 3D calculations have to be performed first.

Calculations performed in this thesis are not as efficient as the S_N can potentially be. At least three underlying methods need to be improved in order to reach the potential computation speed: the discretization method used in the spatial and angular domain, the structure of the discretization in the spatial and angular domain, and the iteration process to converge to continuous scatter operator.

A linear discontinuous finite element method can be used in the angular and spatial domain. This decreases the number of spatial cells and discrete ordinates to produce accurate results, decreasing the number of equations in the set and thereby reducing computation time.

Adaptive mesh refinement can be applied in the spatial and angular domain. This method automatically refines the discretization in the areas of interest. The result of this refinement procedure is an optimal discretization structure in the spatial and angular domain, reducing the number of equations in the set necessary to produce accurate results, and thereby reducing computation time.

In calculations performed in this thesis, a lot of iterations were necessary to converge the continuous scatter operator. This process can be accelerated, for example, by using a multi-grid method in the angular domain. In this method the level of discretization changes in-between the iterations, using interpolation between the finer and coarser grids. In this way fewer iterations are necessary to converge the continuous scatter operator, which results in reduced computation time.

The computation time of the S_N method with the above mentioned improvements included is expected to be small as compared to the computation time of the Monte Carlo method.

8.4 Conclusion

If the angular part of the solution of the S_N method is validated, the S_N method is just as accurate as the Monte Carlo method in proton therapy planning. With the necessary improvements, the S_N method is expected to be much faster as well. Furthermore, compared to the Monte Carlo method, the S_N method offers other advantages as well: it offers a dose profile in the entire region of simulation and it is suitable for perturbation techniques to capture the uncertainty of the chemical composition of the tissue and the movement of the patient. These properties make the S_N method superior to the Monte Carlo method, and therefore, the question if the Monte Carlo method should be replaced by the S_N method in proton therapy planning can be answered positively.

Including the improvements as described in the previous section, the uniform-intensity beam and pencil beam algorithms are still expected to be faster compared to the S_N method, especially in mono-energetic boundary condition problems. However, these methods use rough approximations and the uncertainty in the outcome is difficult to evaluate. Therefore, these methods can only be used in those situations were they are known to give accurate results, or as a first approximation, after which the S_N method needs to be used to validate the outcomes. In situations where the uniform-intensity beam and pencil beam algorithms are not certain to be accurate, the S_N method should be used.

8.5 Future Work

The S_N method, as described in this thesis, is not ready to be applied in clinics. In this section, we describe the improvements that need to be made in future work, in order to make the method ready to be implemented in clinics.

In order to reach the potential accuracy of the S_N method, the models which describe the stopping power and the catastrophic scatter interactions need to be improved. The shell correction needs to be included in the model for the stopping power, or, alternatively, tabulated stopping power data from literature may be used. For the catastrophic scatter interaction process a code or models should be included which are able to generate coupled differential catastrophic scatter cross sections in the energy range 1 - 200 MeV, for protons, neutrons, and photons. The catastrophic differential cross sections need to be accurately described by the Legendre expansion. Therefore, it should be investigated what number of Legendre polynomials is necessary to accurately describe these differential cross sections.

The equations in this thesis are to govern 1D geometries only. These equations need to be expanded to govern 3D geometries for the purpose of proton therapy planning. In a 3D geometry, the angular part of the solution can be benchmarked. The validity of the momentum transfer coefficient can be investigated with the help of these benchmark calculations.

Large angle elastic scatter can not be ignored in 3D geometries. The differential cross sections of the elastic Coulomb scatter with the atomic nuclei need to be decomposed in a singular and a smooth part, in order to describe this large angle scatter with the conventional Boltzmann scatter operator. Therefore, an optimal method for this decomposing needs to be investigated.

The next step is to increase the computation speed. For this purpose, the angular variable and the spatial variables can be discretized by using, for example, a linear discontinuous Galerkin method, the optimal discretization structure can be obtained by applying adaptive mesh refinement, and the convergence of the continuous scatter operator can be accelerated by using, for example, a multi-grid method. Furthermore, it should be investigated if applying even more advanced discretization methods can result in reduced computation time. In this thesis, we solved the average and slope equation together as the basic building block in the iterative method. In future work it should be investigated if including more equations in this basic building block, for example, the average and slope

equation of the neighbor spatial element, can result in reduced computation time.

At this stage, accurate calculations can be performed very efficiently. The next step is to include perturbation techniques, in order to capture the effects of uncertainty of the chemical composition of the tissue in the patient and the movement of the patient. Ideally, the code should be able to adapt the settings of the proton beam to the movements of the patient. To accomplish this, however, we need to be able to image the patient during treatment, like the MRI-accelerator[37] is able to do during electron therapy.

The accuracy of the S_N method is limited by the uncertainty of the chemical composition of the tissues in the patient. MRI and CT scans can be used to obtain this information. Ideally, these scans capture the exact chemical composition of the tissues, and this information is automatically communicated to the S_N code.

After performing these investigations and applying the possible improvements to the S_N method, we conclude that the S_N method is superior to the Monte Carlo method for the purpose of proton therapy planning and is ready to be implemented and used in the radiotherapy clinics.

Appendices

A. Rutherford Scatter

Here, we present a derivation of the relation between the scattering angle Θ and the impact parameter b.

In the center of mass frame, any two body problem is reduced to a one body problem. This greatly simplifies the analysis. We start with Newton's second law of motion in the cylindrical coordinate system:

$$F = m_0 \left(\ddot{r} - r\ddot{\theta} \right). \tag{A.1}$$

Here, F is the force acting on the incident proton, m_0 is the reduced mass of the proton, θ is the angle of position and r is the distance of the proton to the origin of the center of mass frame, see figure A.1. Conservation of angular momentum L requires that:

$$L = m_0 r^2 \dot{\theta} = m_0 v_0 b = \text{constant} \tag{A.2}$$

where b is the impact parameter and v_0 the initial velocity of the incident particle in the laboratory frame. Derivatives of r with respect to time can be rewritten as derivatives of u ($u \equiv \frac{1}{r}$) with respect to angle, using the conservation of angular momentum law:

$$\frac{du}{d\theta} = \frac{d}{dt}\left(\frac{1}{r}\right)\frac{dt}{d\theta} = -\frac{\dot{r}}{r^2\dot{\theta}} = -\frac{\dot{r}}{h} \tag{A.3}$$

$$\frac{d^2u}{d\theta^2} = -\frac{1}{h}\frac{d\dot{r}}{dt}\frac{dt}{d\theta} = -\frac{\ddot{r}}{h\dot{\theta}} = -\frac{\ddot{r}}{h^2u^2}. \tag{A.4}$$

The above can be combined to eliminate explicit time dependence. Physically, we are combining the principle of conservation of angular momentum and the Coulomb interaction between the particles in order to obtain the differential equation of the path of the incident particle:

$$F = m_0 \left(\ddot{r} - r\ddot{\theta} \right) = -m_0 \left(h^2u^2\frac{d^2u}{d\theta^2} + h^2u^3 \right) = -m_0h^2u^2 \left(\frac{d^2u}{d\theta^2} + u \right). \tag{A.5}$$

This equation is called the Binet equation.

The Coulomb force between two points of charge having Z_i and Z_t fundamental charge units for the incoming particle and the target particle respectively, can be written as:

$$F = \frac{1}{4\pi\epsilon_0}\frac{Z_tZ_ie^2}{r^2} \tag{A.6}$$

with ϵ_0 being the vacuum permittivity. This relationship can be plugged into the Binet equation to arrive at:

$$\frac{d^2u}{d\theta^2} + u = -\frac{Z_iZ_te^2}{4\pi\epsilon_0 m_0 v_0^2 b^2}. \tag{A.7}$$

The above differential equation describes the path of the incident proton. The general solution of the above equation;

$$u(v_0, \theta) = u_0 \cos\left(\theta - \theta_0\right) - \frac{Z_iZ_te^2}{4\pi\epsilon_0 m_0 v_0^2 b^2} \tag{A.8}$$

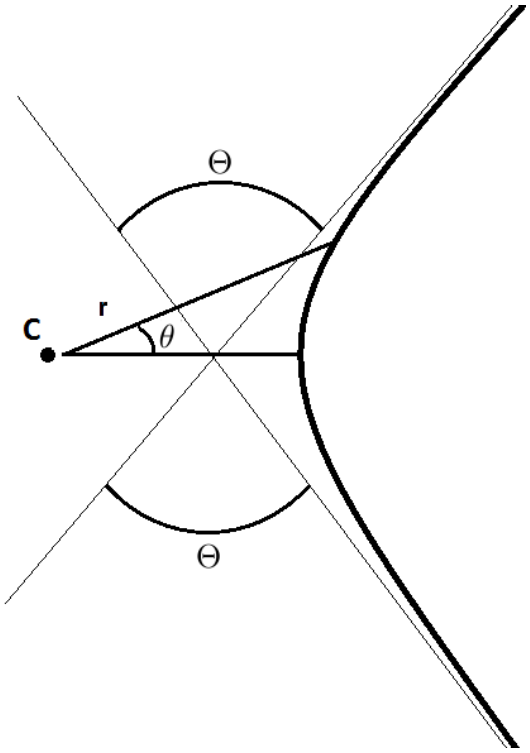

Figure A.1: *The hyperbolic path of the incident proton around the target nucleus. r is the distance between the proton and the nucleus, θ the angle between proton and nucleus, and Θ is the scattering angle.*

where u_0 and θ_0 are constants of integration. The smallest distance between the proton and its target is reached when $\theta = \theta_0$. Since this constant of integration only depends on the orientation of the reference frame, it is allowed to assume $\theta_0 = 0$, this is depicted in figure A.1. By rearranging equation (A.8), this solution for the orbit of the incident proton in the center of mass frame is recognized to be the hyperbolic orbit equation.

$$r = \frac{\frac{1}{\kappa}}{\frac{u_0}{\kappa}\cos(\theta) - 1} \tag{A.9}$$

with;

$$\kappa = \frac{Z_i Z_t e^2}{4\pi\epsilon_0 m_0 v_0^2 b^2}. \tag{A.10}$$

The general hyperbolic orbit equation in polar coordinates:

$$r = \frac{a(\epsilon^2 - 1)}{\epsilon\cos(\theta) - 1} \tag{A.11}$$

Here, ϵ is the eccentricity of the orbit, and a is the semi-major axis of the orbit. By comparing equations (A.9) and (A.11) we can derive the following equalities:

$$\frac{1}{\kappa} = a(\epsilon^2 - 1) \tag{A.12}$$

and

$$\epsilon = \frac{u_0}{\kappa}. \tag{A.13}$$

So, the incident proton makes a hyperbolic orbit around the target nucleus. Now, the next step is to determine the constants of integration u_0. To evaluate this integration constant we apply the principle of conservation of energy to this elastic collision. The kinetic energy of the incident particles must be equal to the electrostatic energy and the kinetic energy of the reduced mass in the center of mass frame. The kinetic energy of the incident particle at the moment of impact is,

$$v_1^2 = \left(\frac{dr}{dt}\right) + \left(r\frac{d\theta}{dt}\right) = \left[\left(\frac{dr}{d\theta}\right)^2 + r^2\right]\left(\frac{d\theta}{dt}\right)^2 \tag{A.14}$$

where v_1 is the velocity of the incident particle at the moment of impact in the center of mass frame. From equation A.8 we obtain (with $\theta_0 = 0$),

$$\frac{dr}{d\theta} = \frac{dr}{du}\frac{du}{d\theta} = \left(-\frac{1}{u^2}\right)(-u_0 \sin\theta) = u_0 r^2 \sin\theta. \tag{A.15}$$

From equation A.2 we have $\frac{d\theta}{dt} = \frac{h}{r^2}$. We use this together with the above to obtain,

$$v_1^2 = u_0^2 h^2 \sin^2\theta + \frac{h^2}{r^2}. \tag{A.16}$$

The sum of the kinetic energy after impact and the electrostatic energy must be equal to the initial kinetic energy of the incident particles,

$$\frac{1}{2}m_0 v_0^2 = \frac{1}{2}m_i v_1^2 \frac{m_i}{m_0} + \frac{Z_i Z_t e^2}{r}\frac{m_0}{m_i} \tag{A.17}$$

where the first term on the right hand side is the total kinetic energy after impact, see Evans[11] p. 833. Rewriting the above,

$$v_0^2\left(\frac{m_0}{m_i}\right)^2 = v_1^2 + \frac{2Z_t Z_i e^2}{r m_i}\left(\frac{m_0}{m_i}\right)^2 \tag{A.18}$$

and substituting v_1^2 from equation A.16 and $\frac{1}{r}$ from equation A.8, we arrive at:

$$\frac{u_0^2}{\kappa^2} = \frac{m^2}{\kappa m_0 b^2} + 1. \tag{A.19}$$

We could solve this equation for u_0, but instead we use this result directly to evaluate the eccentricity of the hyperbolic path of the incident proton from equation (A.13):

$$\epsilon = \sqrt{1 + \frac{m^2}{\kappa m_0^2 b^2}}. \tag{A.20}$$

According to this equation, the eccentricity is always larger than 1. Therefore, the path of the proton is always hyperbolic, and never elliptical. Now, let us take a closer look at the hyperbolic path of the proton. The direction of the incoming asymptote is determined by the boundary condition $r \to \infty$. If we rearrange the orbit equation of the incident proton and apply this boundary condition, we get:

$$\cos(\theta_\infty) = \frac{1}{\epsilon}. \tag{A.21}$$

From figure A.1, we can recognize a relation between the scattering angle Θ and θ_∞:

$$\Theta = \pi - 2\theta_\infty. \tag{A.22}$$

From equation A.21, we can relate this to the scattering angle Θ:

$$\sin\left(\frac{\Theta}{2}\right) = \frac{1}{\epsilon}. \tag{A.23}$$

Hence,

$$\cot^2\left(\frac{\Theta}{2}\right) = \epsilon^2 - 1. \tag{A.24}$$

Together with A.20 this will lead to the final result: the relation between the scattering angle Θ and the impact parameter b:

$$b = \cot\left(\frac{\Theta}{2}\right)\frac{Z_i Z_t e^2}{4\pi\epsilon_0 m_0 v_0^2}. \tag{A.25}$$

This result is the starting point for the derivation of the Rutherford scatter cross sections in chapter 2.

B. Derivation of Continuous Slowing Down and Energy Straggling Operators

In this section, we demonstrate how to derive the continuous slowing down and energy straggling operator from the Boltzmann scatter operator for the inelastic scatter operator of the incident protons with the atomic electrons:

$$L_{B,in}\varphi(E) = \int_0^\infty \sigma_{in}(E')\varphi(E')dQ - \sigma(E)_{in,s}\varphi(E) \tag{B.1}$$

were $E' = E + Q$. The first term on the right hand side represents all the protons that scatter from energy E' to energy E, the second term on the right hand side represent all the protons scattering away from energy E. Small energy transfers dominate the inelastic scatter process of the incident protons with the atomic electrons: the energy E' is close to the energy E. Therefore, we can approximate $\sigma_{in}(E')\varphi(E')$ with a finite Taylor series around E. Including up to second order terms in the approximation leads to:

$$\sigma_{in}(E')\varphi(E') \approx \sigma_{in}(E)\varphi(E) + \frac{\partial\sigma_{in}(E)\varphi(E)}{\partial E}(E' - E) + \frac{1}{2}\frac{\partial^2\sigma_{in}(E)\varphi(E)}{\partial E^2}(E' - E)^2. \tag{B.2}$$

This is implemented in the expression of the Boltzmann scatter operator:

$$\begin{aligned} &L_{B,in}\varphi(E) \approx \\ &\int_0^\infty \left(\sigma_{in}(E)\varphi(E) + \frac{\partial\sigma_{in}(E)\varphi(E)}{\partial E}(E' - E) + \frac{1}{2}\frac{\partial^2\sigma_{in}(E)\varphi(E)}{\partial E^2}(E' - E)^2 - \sigma_{in}(E)\varphi(E))\right) dQ \\ &= \frac{\partial S(E)\varphi(E)}{\partial E} + \frac{1}{2}\frac{\partial^2 T(E)\varphi(E)}{\partial E^2} \end{aligned} \tag{B.3}$$

with

$$S(E) = \int_0^\infty \sigma_{in}(Q)QdQ \tag{B.4}$$

$$T(E) = \int_0^\infty \sigma_{in}(Q)Q^2dQ. \tag{B.5}$$

$S(E)$ is the stopping power which expresses the rate of energy transfer to the atomic electron. $T(E)$ is the energy straggling coefficient which expresses the variance in this stochastic process.

C. Effect of Energy Straggling Operator on Solution of Transport Equation

The energy straggling operator describes the stochastic nature of the energy transfer process of the incident protons to the atomic electrons. This stochastic process is known to be an important process in modeling high energy protons in the energy range considered by NASA in shielding problems for objects in space[44]. In this section, we investigate the influence of the energy straggling operator on the solution of the linear Boltzmann equations for protons in the energy range considered in proton therapy.

The energy straggling operator acts as a diffusion operator of flux in the energy domain. This process in described by a second order derivative of the angular flux in the energy domain. As we have seen in chapter 4, discretization of this operator leads to an expression containting the flux value of both neighbor energy groups. Therefore, we have to iterate to obtain a solution. This iterative process is computation time demanding: in the case of the energy straggling operator, it increases computation time with an approximate factor of 8.

To investigate the effect of the energy straggling operator on the solution of the transport equation, we consider the following transport equation:

$$\mu\frac{\partial\varphi}{\partial x}+\sigma_{C,s}\varphi=\frac{\partial S\varphi}{\partial E}+\frac{\partial^2 T\varphi}{\partial E^2}. \tag{C.1}$$

This equation is discretized according to the requirements we found in chapter 5, and used to calculate the dose deposition distribution of several mono-energetic and plateau boundary condition problems. These same boundary condition problems are evaluated with the transport equation:

$$\mu\frac{\partial\varphi}{\partial x}+\sigma_{C,s}\varphi=\frac{\partial S\varphi}{\partial E} \tag{C.2}$$

which is the same equation as C.1, only without the energy straggling operator included. Now, the difference in the two solutions is evaluated in order to investigate the influence of the energy straggling operator on a solution of a typical proton therapy problem. This is done with the help of the error equation in test case A (table 6.1):

$$\epsilon=\frac{\int_0^\infty (D_{ref}-D)^2\,dx}{\int_0^\infty D_{ref}^2 dx} \tag{C.3}$$

where we take the solution of the transport equation C.1 as the reference solution. In this way we evaluate the error in a solution if we ignore the energy straggling operator.

In figure C.1 the energy spectrum is plotted of the two solutions at x = 2.5 cm in the slab of a $\Delta E_p = 25$ MeV, $E_{max} = 100$ MeV boundary condition problem. From this figure we already see by inspection that the difference between the solutions is small. Only at the positions in the energy spectrum were the gradients are high, the solution of equation C.1 shows a somewhat smoother energy spectrum. The errors evaluated with equation C.3 were $\epsilon \approx 10^{-5}$ for all problems, which is an order of magnitude smaller compared to the error in the solution which we allowed due to discretization.

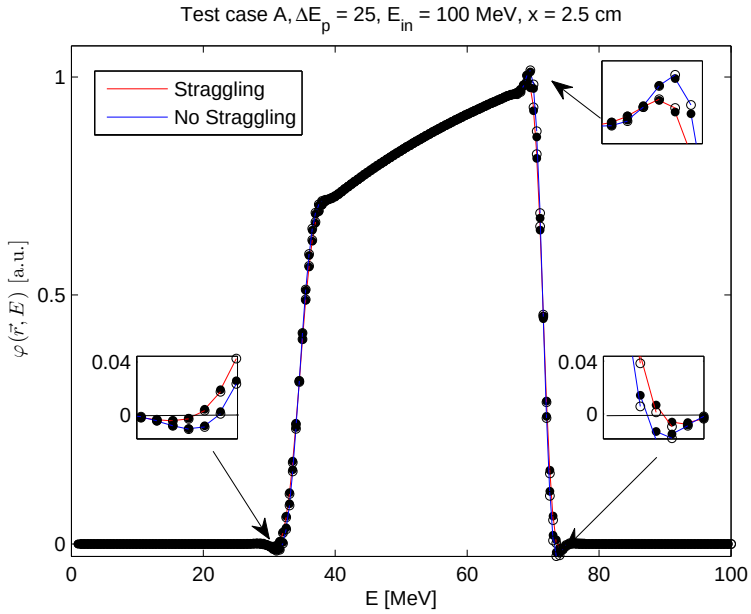

Figure C.1: *Test case A, energy spectrum of plateau boundary condition problem, with and without straggling operator.*

So, in conclusion, the energy straggling has only a minor effect on the solution, while it increases the computation time significantly. Therefore, the energy straggling operator can be ignored in the transport equation for proton transport calculations in the energy range considered in proton therapy planning.

D. Results Discretization Requirements

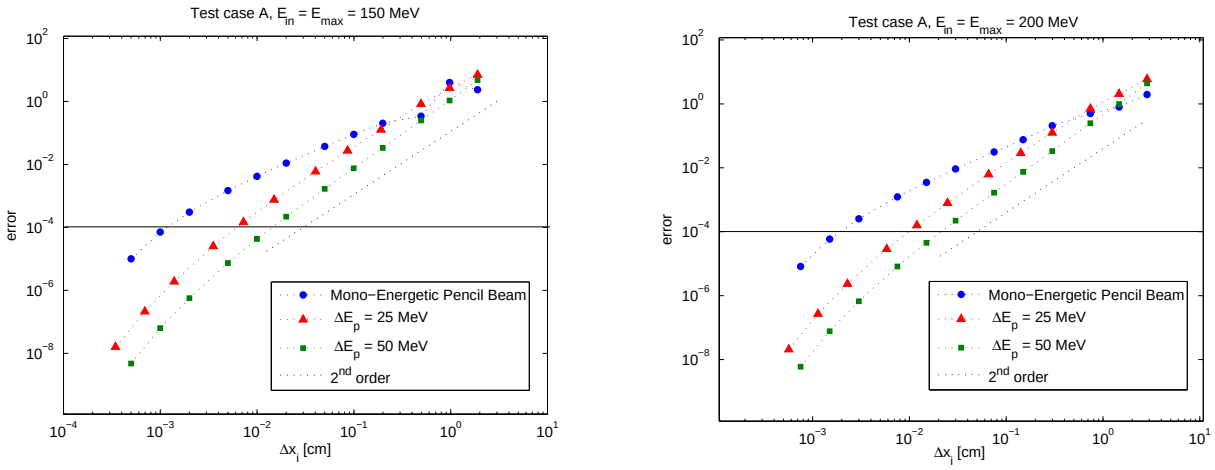

Figure D.1: *Left: test case A, error versus width of spatial cell Δx_i, $E_{in} = 150$ MeV. Right: test case A, error versus width of spatial cell Δx_i, $E_{in} = 200$ MeV.*

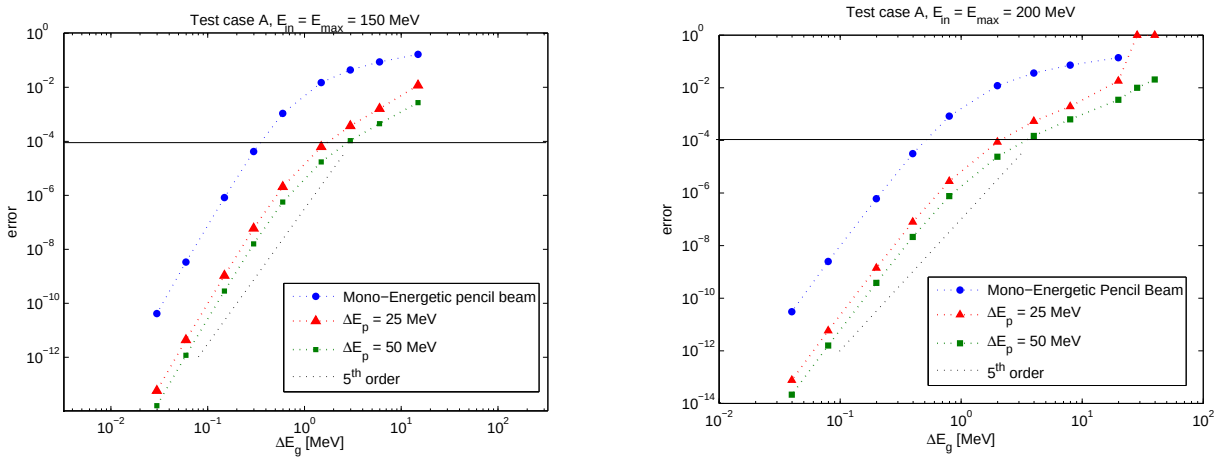

Figure D.2: *Left: test case A, error versus energy width ΔE_g, $E_{in} = 150$ MeV. Right: test case A, error versus energy group width ΔE_g, $E_{in} = 200$ MeV.*

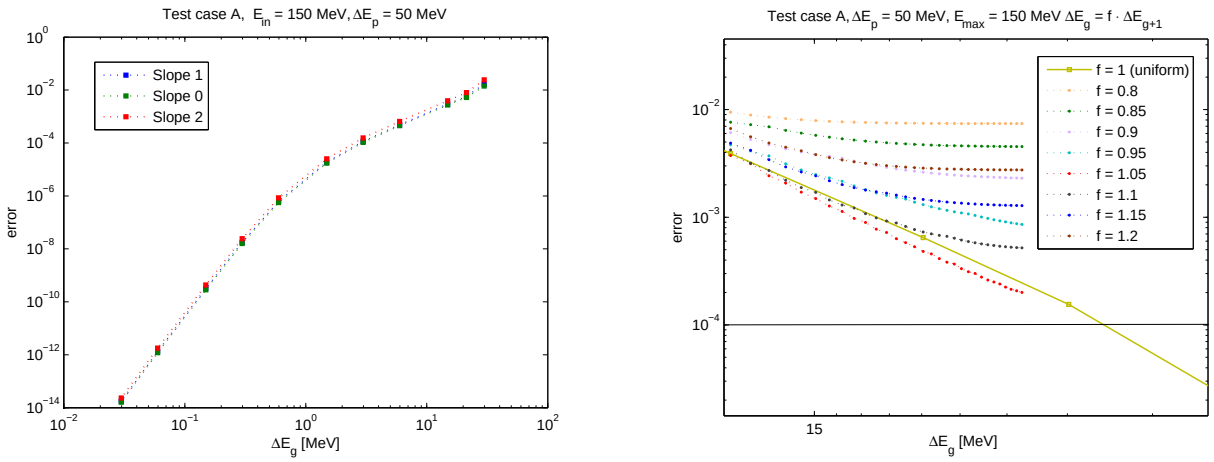

Figure D.3: *Left: test case A, error versus energy width ΔE_g. The slope of the plateau does not influence the discretization requirement. Right: test case A, error versus energy width ΔE_g. f in $\Delta E_g = f \cdot \Delta E_{g+1}$. The uniform energy structure is optimal in most problems. In this case, however, solution can be obtained more efficiently by applying a different energy structure than the uniform one, but the gain is not significant.*

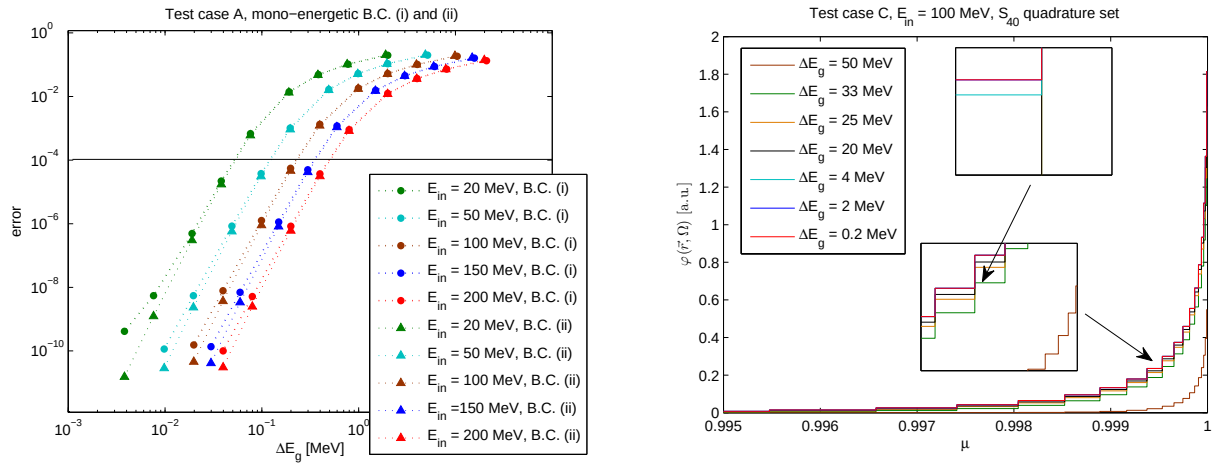

Figure D.4: *Left: test case A, error versus energy width ΔE_g. The error using boundary condition (i) and (ii) is similar, see section 6.3.1. Right: test case C, illustration of the error in the differential flux for several group widths ΔE_g, $E_{in} = 100$ MeV.*

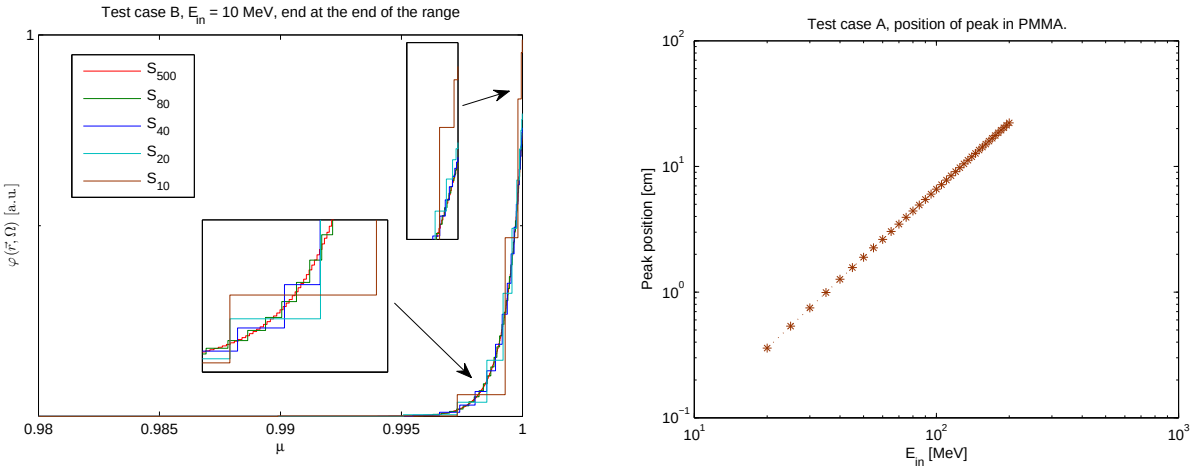

Figure D.5: *Left: test case B, differential flux at the end of the range, E_{in} = 10 MeV. The error in the low quadrature is large near $\mu = 1$ and decreases rapidly further away from $\mu = 1$. Right: test case A, Bragg peak position in PMMA. The position of the Bragg peak is used to impose a range in test case C over which the error in a calculation is evaluated.*

Bibliography

[1] R. Barett et al.
Templated for the Solution of Linear Systems: Building Blocks for Iterative Methods.
siam, 1994.

[2] M.J. Berger, D.S. Zucker, M.A. Zucker, and J. Chang.
Stopping-power and range tables for electrons, protons, and helium ions.
NIST Stand. Ref. Database, 2000.

[3] A. Biegun.
Post doctoral researcher.

[4] A.J.J. Bos, F.S. Draaisma, and W.J.C. Okx.
Inleiding tot Stralingshygiene.
Sdu Uitgevers, 2007.

[5] D.C. Cacuci.
Handbook of Nuclear Engineering.
Springer, 2010.

[6] Proton Therapy Center.
Principles of proton therapy.
`http://en.ptc.cz/proton-therapy/principles-of-proton-therapy`.

[7] W.H. St. Clair, J.A. Adams, M. Bues, B.C. Fullerton S. La Shell, H.M. Kooy, J.S. Loeffler, and N.J. Tarbell.
Advantage of protons compared to conventional x-ray or imrt in the treatment of a pediatric patient with medulloblastoma.
International Journal of Radiation Oncology Biology Physics, 58(3):727–734, 2004.

[8] T.F. DeLaney and H.M. Kooy.
Proton and Charged Particle Radiotherapy.
Wolters Kluwer, 2008.

[9] J.J. Duderstadt and L.J. Hamilton.
Nuclear Reaction Analysis.
Wiley, 1976.

[10] S.I. Alekhin et al.
Ihep preprint.
Protvino, pages 87 – 125, 1987.

[11] D. Evans.
The Atomic Nucleus.
Tata McGraw-Hill Publishing Company Ltd, 1955.

[12] J. Ferlay, H. . Shin, F. Bray, D. Forman, C. Mathers, and D. M. Parkin.
Estimates of worldwide burden of cancer in 2008: Globocan 2008.
International Journal of Cancer, 127(12):2893–2917, 2010.

[13] P. Fossati, U. Ricardi, and R. Orecchia.
Pediatric medulloblastoma: Toxicity of current treatment and potential role of protontherapy.
Cancer treatment reviews, 35(1):79–96, 2009.

[14] H. Goldstein.
Classical Mechanics.
Addison Wesley, 2002.

[15] D.V. Gorbatkov and V. P. Kryuchkov.
Sadco-2: a modular code system for generating coupled nuclear data libraries to provide high-energy particle transport calculation by multigroup methods.
Nuclear Instruments and Methods in Physics Research, 1995.

[16] S. Goudsmit and J.L. Saunderson.
Multiple scattering of electrons.
The American Physical Society, 1940.

[17] E.C. Halperin, C.A. Perez, and L.W. Brady.
Principles and practice of Radiation Oncology.
Wolter Kluwer, 2007.

[18] J.S. Hesthaven and T. Warburton.
Nodal Discontinuous Galerkin Methods.
Springer, 2000.

[19] ICRU.
report 49: Stopping power and ranges for protons and alpha particles, 2007.

[20] P. M. DeLuca Jr., A. Wambersie, and G. Whitmore.
Prescribing, recording, and reporting proton-beam therapy.
Journal of the ICRU, 7(2):1–210, 2007.

[21] N. Keen.
Ion cross section and monte carlo simulations using multigroup boltzmann fokker-planck transport.
Master's thesis, University of New Mexico, 1999.

[22] C. T. Kelsey.
Coupled multigroup proton/neutron cross section preparation using mcnpx and njoy for deterministic transport calculations.
Master's thesis, Texas A M University, 1992.

[23] E. Larsen and C. Brgers.
On the accuracy of the fokker-planck and fermi pencil beam equations for charged particle transport.
Nuclear Science and Engineering, 137:236, 2000.

[24] C.L. Leakeas and E.W. Larsen.
Generalized fokker-planck approximations of particle transport with highly forward-peaked scattering.
Nuclear Science and Engineering, 137(3):236–250, 2001.

[25] C.T. Lee, S.D. Bilton, R.M. Famiglietti, B.A. Riley, A. Mahajan, E.L. Chang, M.H. Maor, S.Y. Woo, J.D. Cox, and A.R. Smith.

Treatment planning with protons for pediatric retinoblastoma, medulloblastoma, and pelvic sarcoma: How do protons compare with other conformal techniques?
International Journal of Radiation Oncology Biology Physics, 63(2):362–372, 2005.

[26] W.P. Levin, H. Kooy, J.S. Loeffler, and T.F. DeLaney.
Proton beam therapy.
British journal of cancer, 93(8):849–854, 2005.

[27] P. Mayles, A. Nahum, and J.C. Rosenwald.
Handbook of Radiotherapy Physics.
Taylor and Francis, 2007.

[28] B.J. McParland.
Nuclear Medicine Radiation Dosimetry.
Springer Verlag, 2010.

[29] T.E. Merchant, C. Hua, H. Shukla, X. Ying, S. Nill, and U. Oelfke.
Proton versus photon radiotherapy for common pediatric brain tumors: Comparison of models of dose characteristics and their relationship to cognitive function.
Pediatric Blood and Cancer, 51(1):110–117, 2008.

[30] R. Miralbell, A. Lomax, L. Cella, and U. Schneider.
Potential reduction of the incidence of radiation-induced second cancers by using proton beams in the treatment of pediatric tumors.
International Journal of Radiation Oncology Biology Physics, 54(3):824–829, 2002.

[31] J.E. Morel, A.K. Prinja, J.M. McGhee, T.A. Wareing, and B.C. Franke.
A discretization scheme for the 3-d continuous-scattering operator.
Physics in Medicine and Biology, 54(3):731–743, 2009.

[32] D.B. Pelowitz.
MCNPX user's manual version 2.5.0.
Los Alamos National laboratory, 2005.

[33] J.C. Polf, S. Peterson, M. McCleskey, B.T. Roeder, A. spiridon, S. Beddar, and L. Trache.
Measurement and calculation of characteristic prompt gamma ray spectra emitted during proton irradiation.
Physics in Medicine and Biology, 54, 2009.

[34] W. R. Polkinghorn and N. J. Tarbell.
Medulloblastoma: Tumorigenesis, current clinical paradigm, and efforts to improve risk stratification.
Nature Clinical Practice Oncology, 4(5):295–304, 2007.

[35] ProCure.
Pediatric brain cancer: Proton therapy delivers less eadiation to healthy organ than x-rays, reducing the likelihood of side effect, 2012.
`http://www.procure.com/ProtonTherapy/TumorsTreated/PediatricCancer.aspx`.

[36] PTCOG.
Particle therapy facilities in operation, 2012.

[37] B. W. Raaymakers, J. J. W. Lagendijk, J. Overweg, J. G. M. Kok, A. J. E. Raaijmakers, E. M. Kerkhof, R. W. Van Der Put, I. Meijsing, S. P. M. Crijns, F. Benedosso, M. Van Vulpen, C. H. W. De Graaff, J. Allen, and K. J. Brown.

Integrating a 1.5 t mri scanner with a 6 mv accelerator: Proof of concept.
Physics in Medicine and Biology, 54(12):N229–N237, 2009.

[38] B. Rossi.
High-Energy Particles.
Prentice-Hall, 1952.

[39] W. Schlegel, T Bortfeld, and A.L. Grosu.
New Technologies in RadiationOncology.
Springer, 2006.

[40] P. H. Smith.
Analysis of moment-preserving methods for charged particle transport.
Master's thesis, University of New Mexico, 2007.

[41] J.E. Turner.
Atoms, Radiation, and Radiation Protection.
John Wiley and Sons, 1992.

[42] A. Wambersie, F. Richard, and N. Breteau.
Development of fast neutron therapy worldwide. radiobiological, clinical and technical aspects.
Acta Oncologica, 33(3):261–274, 1994.

[43] E.J. Williams.
Proceedings of the Royal Society.
Prentice-Hall, 1939.
[Chap. 18,Sec. 2; Chap. 21, Sec. 1; Chap. 22, Sec. 5].

[44] J.W. Wilson and T. Hsiang.
Range and energy starggling in ion beam transport.
NASA Technical Publication, 2000.

[45] R. Wilson.
Radiological use of fast protons.
Radiology, 47(5):487–491, 1946.

[46] H.Q. Woodward and D.R. White.
The composition of body tissues.
The British Journal of Radiology, 59:1209–1219, 1986.

[47] J.F. Ziegler.
The stopping of energetic light ions in elemental matter.
Journal Applied Physics, 85:12409–1272, 1999.

[48] A.L. Zietman.
The titanic and the iceberg: Prostate proton therapy and health care economics.
Journal of Clinical Oncology, 25(24):3565–3566, 2007.